공학박사학위논문

Cavitation Instability Mechanism and Thermal Effects in a Turbopump Inducer

터보펌프 인듀서에서의 캐비테이션 불안정성 메커니즘 및 열적 효과 연구

2018 년 2 월

서울대학교 대학원

기계항공공학부

김 준 호

Abstract

Cavitation Instability Mechanism and Thermal Effects in a Turbopump Inducer

Junho Kim

School of Mechanical and Aerospace Engineering

Seoul National University

An experimental investigation has been conducted on the cause and pulsation mechanism of rotating cavitation and thermal effects on the onset of rotating cavitation. To achieve the research objectives, the test facility has been designed and constructed in Seoul National University.

Based on the previous research, the author hypothesized that the incidence angle variation leads to the onset of rotating cavitation. To confirm the hypothesis, the incidence angle has been measured near the tip region of the leading edge with and without rotating cavitation through PIV (Particle Image Velocimetry) measurement

method. Under the rotating cavitation conditions, large and small tip leakage vortex cavitation regions are formed, respectively, and the cavitation region at each blade becomes uneven. The large tip leakage vortex cavitation reduces the following blade incidence angle to the negative value and suppresses the cavitation region. On the other hand, the small tip leakage vortex cavitation increases the following blade incidence angle to the positive value and promotes the cavitation region. Reduction of the incidence angle due to the cavitation region leads to the onset of rotating cavitation. Based on the suppression and promotion mechanism, cavitation region at each blade pulsates in sequence at the measured rotating cavitation frequency. The propagation of rotating cavitation has also been confirmed by high-speed camera visualization.

Through the time-resolved static pressure measured at the inlet of the turbopump inducer, the onset cavitation number of rotating cavitation has been determined for varying Reynolds number and non-dimensional thermal parameter values. Increasing non-dimensional thermal parameter suppresses rotating cavitation and causes a monotonic decrease in the rotating cavitation onset cavitation number. At low non-dimensional thermal parameter values (e.g., 0.0125), the onset cavitation number is independent of the Reynolds number. However, at higher values of the non-dimensional thermal parameter (e.g. higher than 0.0537), the onset cavitation number increases with increasing Reynolds number. Thus, the Reynolds number promotes rotating cavitation onset.

This study provides the first experimental results of the cause and mechanism of rotating cavitation. The first assessment of the individual effects of the non-dimensional thermal parameter and

Reynolds number is also presented.

Keyword: Turbopump Inducer, Cavitation Instability, Cavitation Performance, Thermal Effects, Rotating cavitation, Particle Image Velocimetry

Student Number: 2011-23329

Table of Contents

List of Figures

List of Tables

Nomenclature

A	area of an inducer inlet, m^2
c	tip clearance
C_{pl}	liquid heat capacity
C_p	pressure coefficient
C	characteristic length of an inducer
ϵ	resonance margin
E	modulus of elasticity
f	frequency, Hz
f_r	real frequency of instability, Hz
f_d	detected frequency, Hz
g	gravitational acceleration
G	velocity divergence
I	moment of inertia
l	shaft length
k	polytrophic constant
L	latent heat
n_{cell}	number of rotating cells

Nu_D	Nusselt number
p	pressure
p_{G0}	partial pressure of the non-condensable gas in the bubble
p_v	vapor pressure
$p_{v,B}$	vapor pressure in cavitation bubble
Δp_v	vapor pressure depression within the bubble
Pr	Prandtl number
r	inducer inlet radius
R	bubble radius
$\bar{R}$	non-dimensional bubble radius
$q_s^{'}$	heat transfer rate
Q	flow rate or 2nd invariant Q
S	Surface tension
t	time
Δt	Time interval between the two laser pulses
T	temperature
ΔT	depression of temperature within the bubble
u	uncertainty
U	tip rotational speed

x	distance along the streamline followed by the bubble
$\bar{x}$	non−dimensional distance
ρ_l	liquid density
ρ_v	vapor density
α_l	thermal diffusivity of liquid
γ	specific weight
σ	cavitation number, = $(p_1 - p_v)/\frac{1}{2}\rho r^2\omega^2$
σ_{eff}	effective cavitation number considering thermal effects
ϕ	flow coefficient, = $Q/Ar\omega$ or phase of the cross correlation
Σ	dimensional thermal parameter
Σ^*	non−dimensional thermal parameter
θ	angular distance, °
ψ	head coefficient, = $(p_2 - p_1)/\frac{1}{2}\rho r^2\omega^2$
$\Delta\psi$	unsteady pressure fluctuation coefficient (peak to peak)
ω	rotational speed, 1/s
ω_1	critical speed of the shaft
Ω	rotational frequency, Hz
∇	divergence

Subscripts

1	Inlet
2	outlet
d	design
B	bubble
l	liquid
p	particle
∞	reference liquid or bulk liquid

Chapter 1. Introduction

1.1. Study Background

1.1.1. Turbopump Inducer

To achieve high performance and reliable control of thrust, liquid propellants are mostly used to rocket engine system recently. Recently, the Republic of Korea is developing a liquid rocket by itself. For liquid rocket engines, turbopumps (Fig. 1.1) supply liquid oxidizer and fuel to the combustion chamber at high pressure. Turbopump is composed of an oxidizer pump, a propellant pump, and a turbine as shown in Fig. 1.2. To reduce the entire rocket engine weight, especially to minimize the weight of the oxidizer and fuel tank, liquid oxidizer and fuel need to stay at low pressure. Turbopumps rotate at high speeds to achieve high power densities. Such requirements lead to cavitation in turbopumps. Therefore, to inhibit cavitation in the impeller, an axial type inducer is installed upstream of a turbopump as shown in Fig. 1.2. The inducer is used to increase the pressure before the impeller. However, the inducer itself also can suffer from cavitation. The inducer has screw type blades with a long flow path for cavitation bubbles to be vanished while passing through the inducer. Thus, cavitation occurs frequently in the inducer. As cavitation in the inducer becomes severe, the pressure rise is degraded and hydraulic instabilities can occur.

Performance degradation and hydraulic instabilities caused by cavitation in the inducer are important issues for turbopump developers. However, complete understandings of cavitation in the inducer has not yet been achieved. In this study, the mechanism of cavitation instability and thermal effects on cavitation instability have been investigated experimentally.

1.1.2. Fundamentals of Cavitation

Cavitation is the one of the vaporization process. Contrary to boiling, the phase change in case of cavitation occurs due to a pressure drop at a given temperature (Fig. 1.3). To quantify the degree of the cavitation occurrence, cavitation number, σ, is generally employed. It is defined as the pressure difference between reference liquid pressure, p_∞, and the liquid's vapor pressure, p_v, corresponding to its temperature, non-dimensionalized by the dynamic pressure as shown in Eq. (1).

$$\sigma = \frac{p_\infty - p_v}{\frac{1}{2}\rho_l U^2} \tag{1.1}$$

It represents a margin before flow begins to cavitate. Thus, a decreases in cavitation number eventually results in cavitation.

Cavitation is initiated from microscopic nuclei or micro bubble in the flow. These nuclei grow through the low pressure region and become a cavitation bubble. Cavitation bubbles grow and collapse over time. The history of cavitation bubble could be predicted by Rayleigh-Plesset equation [2] in Eq. (2), which describes the bubble dynamics.

$$R\frac{d^2R}{dt^2}+\frac{3}{2}\left(\frac{dR}{dt}\right)^2=\frac{p_v(T_\infty)-p_\infty}{\rho_L}+\frac{p_v(T_B)-p_v(T_\infty)}{\rho_L}-\frac{4\mu_l}{\rho_l}\frac{dR}{dt}+\frac{2S}{\rho_l R}+\frac{p_{G0}}{\rho_l}\left(\frac{T_B}{T_\infty}\right)\left(\frac{R_0}{R}\right)^{3k} \quad (1.2)$$

This equation determines the temporal evolution of the cavitation bubble radius, R, under given pressure field, p_∞(t). For the simplicity, several assumptions were made: 1) spherical bubble; 2) incompressible liquid; 3) homogeneous contents of bubbles; 4) The derivation of the Rayleigh–Plesset equation is well described in textbooks of cavitation [[3],[4]].

The left hand side of the equation represents the expected output of the time evolution of the bubble radius. On the right hand side of the equation, the first term is pressure driving term determined by the conditions far from the bubble, the second term represents thermal effects, the third term represents the viscous effect, the fourth term is the surface tension effect, and last term shows the non–condensable gas effects in the bulk liquid. From the Rayleigh–Plesset equation, the growth and collapse of cavitation bubble can be simply understood.

Cavitation is easily observed in hydrofoil, nozzle, and many turbomachinery which operate in liquids. There are several types of cavitation. The characteristics of each type of cavitation are different and these cavitation occur simultaneously, thus it is difficult to investigate cavitation.

1.1.3. Types of Cavitation

There are several types of cavitation according to the environmental condition.

Travelling bubble cavitation is isolated bubbles foaming mainly due to the nuclei or microbubbles in the free stream (Fig.1.4 (a)). Thus, it strongly depends on the water quality. The bubbles are collapsed when they enters the sufficiently high pressure region. Traveling cavitation appears on the low pressure region on turbomachinery blades operating in liquid such as the outlet of Francis turbines or the inlet of centrifugal pumps.

Attached cavitation or sheet cavitation occurs most commonly in the low pressure region of blades or hydrofoils as shown in Fig. 1.4 (b). Attached cavitation is the main source of unsteadiness in the rear part of the cavity. Partial cavitation is one of the attached cavitation, which usually develops in regions of separated flow (e.g. venture nozzles or suction side of hydrofoils). At the closure region of the attached cavitation, the liquid flow re-attaches to the wall and splits into two parts: one is re-entrant jet which penetrates the attached cavitation and the other is the main outer flow which reattaches to the wall. Re-entrant jet leads to the detachment of the attached cavitation when the jet encounters the cavity interface, and the detached cavitation becomes the unstable cloud cavitation. This phenomenon has periodicity.

In hydrofoils, as cavitation number decreases further, partial cavitation becomes super-cavitation (Fig. 1.4 (c)) which closes downstream of the trailing edge, not on the foil. In practice, to reduce the drag in liquid, super-cavitation conditions are deliberately created in such as torpedoes.

Vortex cavitation is observed in 3D hydrofoil or turbulent wakes in the bluff body as shown in Fig. 1.4 (d). In propellers or pumps,

tip vortex cores are low pressure region, thus, the vortex cavitation occurs. Also, the pressure difference between the suction and pressure side leads to the leakage flow through the tip. The shear region of the leakage flow forming the tip leakage vortex cavitation which often is observed in axial type pump like an inducer. In the inducer, backflow vortex structure between the swirling backflow and the main flow is found even in the design flow coefficient. The backflow vortex region is low pressure region, thus the cavitation occurs following the vortex core called backflow vortex cavitation.

1.1.4. Cavitation in Turbomachinery

In practical turbomachinery, various types of cavitation, which are described above, occur simultaneously and affect each other. For turbopump inducers, tip leakage vortex cavitation, attached cavitation, and backflow vortex cavitation occur simultaneoulsy as shown in Fig. 1.5 (a) [6]. Tip vortex cavitation, travelling bubble cavitation, and various types of attached cavitation are frequently observed in ship propellers (Fig. 1.5 (b) [7]. In hydraulic turbines, attached cavitation also occurs due to the low pressure region of the turbine exit and induces structural damage such as cavitation erosion [8]. Furthermore, in an axial type pump, the interaction between the sheet cavitation on the suction side of the blade and the tip vortex cavitation generates the perpendicular cavitating vortices [9], [10]. The occurrence of cavitation induces harmful effects such as hydraulic performance degradation, vibration, and structural damage causing erosion as shown. Thus, turbomachinery designers try to minimize cavitation effects or at least needs to consider the cavitation occurrence when they design

turbomachinery in cavitating conditions.

1.1.5. Cavitation in Turbopump Inducers

Figure 1.6 represents the schematic of general types of cavitation occurring at the inducer– backflow vortex cavitation and tip leakage vortex cavitation (re–drawn from [11]). Backflow vortex cavitation is formed by a vortex between the main flow and the backflow. Tip leakage vortex cavitation is due to tip leakage vortex from the pressure side to the suction side. As cavitation number decreases, tip leakage vortex cavitation region becomes larger. These two types of cavitation occurs simultaneously, thus, it is difficult to extinguish each cavitation effects.

Under cavitating condition, cavitation performance, which shows the head coefficient variation according to the cavitation number, is applied to represent the performance of inducers or impellers. Figure 1.7 shows the typical cavitation performance of the inducer. Even though the cavitation decreases to the certain cavitation number called a critical cavitation number (σ_{crit}) the head coefficient remains constant. When the cavitation number becomes lower than the critical cavitation number, the head coefficient begins to decrease. The critical cavitation number (defined to be the cavitation number at which the head coefficient value decreases to 97 % of the nominal value) is used to signify the head coefficient degradation. Further diminution in cavitation number leads to major degradation in the head coefficient. To quantify the major degradation, the breakdown cavitation number (σ_b) (defined to be the cavitation number at which 25 % head coefficient drop occurs)

is usually applied.

1.1.6. Cavitation Instability

Inducer cavitation can also cause hydraulic instabilities, which are called cavitation instability. Cavitation instabilities can be broadly categorized into rotating cavitation, asymmetric attached cavitation, and cavitation surge. Rotating cavitation and asymmetric attached cavitation are rotational cavitation instabilities which are local instabilities. Cavitation surge is an axial instability which oscillates overall system. Cavitation instabilities are usually identified from power spectrum density from the unsteady pressure as shown in Fig. 1.8 [12]. Cavitation instabilities have detrimental effects on turbopump inducer system reliability causing flow rate or pressure oscillations, shaft vibration, and structural damage.

Rotational cavitation instabilities

When **rotating cavitation** occurs, cavitation region at each blade becomes uneven forming 2 large cavitation region and 1 small cavitation region. Cavitation regions at each blade oscillates in order at 0.1−0.2 Ω speed, thus the uneven cavitation region seems to propagate at super−synchronous (1.1−1.2 Ω) speed in the same direction of inducer as shown in Fig. 1.9 (a). It seems like the rotating stall in compressors, but the propagation speed and the mechanism are totally different. Rotating stall occurs where the positive slope of head−flow rate curve, on the other hand, rotating

cavitation occurs in the negative slope, even at the design flow coefficient. Rotating cavitation is observed in severe cavitating conditions. Therefore, it is difficult to understand the mechanism through the analytical or numerical method like rotating stall [13].

Asymmetric attached cavitation also forms uneven cavitation like rotating cavitation, but cavitation regions at each blade does not oscillate. Thus, in asymmetric attached cavitation, the each cavitation region rotates at the same speed as the inducer (Fig. 1.9 (b)). As the uneven cavitation region attached to the blade, asymmetric attached cavitation can be simulated with steady condition [14].

For an even number blade inducer, another rotating instability, alternate blade cavitation, may occur. Alternate blade forms symmetric cavitation region attached to inducer blade (for 4 blade number inducer case– 2 large cavitation region and 2 small cavitation region as shown in Fig. 1.9 (c)), thus the frequency is twice of the inducer rotational frequency. Rotating instabilities can cause blade flutter excitation or fraction due to resonance.

Cavitation surge

For cavitation surge, cavitation region at each blade periodically oscillate with the same phase (Fig. 1.9 (d)). It leads to axial oscillation and fluctuation of flow rate. The oscillation frequency is in the low frequency range 0.1–0.2 Ω. Cavitation surge usually occurs at lower cavitation number than other types of cavitation instabilities. Cavitation surge is also different phenomenon from surge in compressor. It also occurs in the negative slope of head–flow rate curve and does not have the same surge cycle as shown in

compressor surge [15]. Cavitation surge causes severe degradation of the head coefficient, stronger vibration than rotational instabilities and is suspected to be the one of the cause of POGO instability in rocket engines.

Other types of cavitation instabilities

Recently, Fujii et al. [16] and Tsujimoto et al. [17] found new types of cavitation instabilities such as higher order rotating cavitation and higher order cavitation surge. These instabilities have similar characteristics with the conventional rotating cavitation and cavitation surge, but they occur at higher frequencies than the conventional cavitation instabilities. Due to their higher frequencies, they may cause resonance of the inducer blades. Semenov et al. [18] conducted a study on the rotating choke occurred in a low flow rate, which was a recent problem in Japan's rocket. Watanabe et al. [19] investigated the chocked surge by chocking in the 3-blade and 4-blade inducer. Choked surge also occurs in the very low flow rate.

1.2. Literature Review

1.2.1. Previous Research: Rotating Cavitation

As described above, there are several types of cavitation instability. Rotating cavitation occurs at relatively higher cavitation number, thus, it has been encountered frequently in the development process of high performance turbopumps such as

Space Shuttle Main Engine [20], European Ariane 5 engine [21], LE-7 engine [22]. More seriously, rotating cavitation induces the vibration, blade fracture and even entire rocket failure, as reported in Japan H-2 failure [23]. For these reasons, numerous studies have been conducted to investigate rotating cavitation characteristics, occurrence ranges, mechanism, and suppression method for decades through experimental, analytical, and numerical methods.

Experimental approach

Kamijo et al. [24] experimentally examined rotating cavitation with unsteady pressure transducers and cavitation visualization. Tsujimoto et al. [25] identified detailed characteristics of cavitation instabilities, including the propagation speed, cell number, and dependency on the rotational speed and piping system. The suppression of performance degradation and cavitation instabilities is important issue for turbopump developers.

To suppress the cavitation instability, simple modifications of the inducer casing have been proposed. Kamijo et al. [22] and Hashimoto et al. [26] succeeded in the suppression of rotating cavitation through the inducer upstream casing modification. Also, axial grooves and circumferential grooves on the inducer casing suppressed the onset of rotating cavitation [[27]-[29]]. The backflow vortex cavitation is also suppressed when the casing modification method is adapted. As backflow vortex cavitation is changed, the incidence angle at the inducer is also varied. Thus, these studies gave the clue that the incidence angle plays important role in rotating cavitation. Lettieri et al. [30] tried to explain the

mechanism of rotating cavitation with visualization. They reported that the rotating cavitation onset is governed by the interaction of the blade cavitation with the leading edge of the adjacent blade. But, they did not fully explain how the interaction change the flow field of the adjacent blade.

Analytical approach

Analytical studies have been performed to investigate cavitation instabilities. Tsujimoto et al. [31] developed an analytical model for prediction of rotating cavitation using the actuator disk method. They proposed the criterion for the occurrence of rotating cavitation. The mass flow gain factor and cavitation compliance play a major role in the occurrence of rotating cavitation. Tsujimoto et al. [32] also proposed the unified model for four flow instabilities of turbomachinery– surge, rotating stall, cavitation surge, and rotating cavitation. This model did not reflect all characteristics of flow instabilities, but tried to explain the onset condition and frequency using the simplest model. However, these models developed in 2–D cascade and did not consider the cavitation characteristics sufficiently.

Watanabe et al. [33] and Horiguchi et al. [34] also developed an analytical model to predict the criterion for rotating cavitation and alternate blade cavitation using singularity and closed cavity model. Cavitation region and blade are considered as sink and vortex term respectively. They also proposed that the cavitation instability occurs when the cavitation length is 65 % of the blade pitch length and validated with the experimental results. However,

other experimental results [6] showed different results with which the criterion does not agree. In addition, their model is also 2-D cascade and they assumed that the cavitation region is attached cavitation, thus, it is difficult to apply in 3-D real inducer with tip leakage vortex cavitation case.

Numerical approach

Numerical analysis to understand cavitation instabilities has been conducted. Iga et al. [[35]-[37]] simulated cavitation instabilities in 2-D cascade. They treated the gas-liquid two-phase medium inside the cavitation as a locally homogeneous pseudo-single-phase medium. The results was validated with the pressure distribution of cascade hydrofoils. The propagation speed mechanism of rotating instability was proposed based on the natural characteristics of the break-off frequency of sheet cavitation. However, in real inducer, tip leakage vortex cavitation, which is different from the sheet cavitation, plays an important role in rotating cavitation. Also, the authors assumed that the weak rotating stall exists even though the slope of head-flow rate curve is negative (i.e. stable condition), which was required to match the estimated frequency of rotating cavitation with experiments. 2-D cascade model does not simulate tip leakage vortex cavitation, thus, Iga et al.'s model did not simulate real inducer cavitation instabilities.

3-D CFD simulation of rotating cavitation has been conducted from many research groups. Kimura et al. [38] explained that the rotating cavitation is related to the tip leakage vortex through

experiments and the non-cavitating 3-D simulation. They found that the flow coefficient where rotating cavitation occurs corresponds to the flow coefficient at which tip vortex cavitation interacts with the next blade. Hosangadi et al. [39] performed numerical simulation for 4-blade SSME low pressure fuel pump inducer. They found that the interaction of the cavitation region with neighboring blade leads to rotating cavitation. Kang et al. [40] simulated cavitation instabilities and explained the propagation mechanism of rotating cavitation. When cavitation region increases, the incidence angle of next blade is decreased and the cavitation region of the next blade also is also decreased. Therefore, the propagation of rotating cavitation is forward to the inducer rotation. Tani et al. [41] also performed 3-D CFD under rotating cavitation with the different flow rate. They calculated the incidence angle variation according to the inducer rotation, and found out that the incidence angle changes near the leading edge of the blade under rotating cavitation due to the cavitation collapse. They explained that the rotating cavitation does not occur in low flow coefficient. For the low flow coefficient, the relative incidence angle change is small, thus rotating cavitation did not occur.

Until now, numerical simulation for rotating cavitation has been performed by unsteady Reynolds Averaged Navier Stokes (RANS). However, simulations with RANS cannot predict the backflow vortex cavitation and tip leakage vortex cavitation accurately. Thus, the rotating cavitation results from the CFD needs experimental validations.

1.2.2. Previous Research: Thermal Effects

Thermal effects on cavitation

Cavitation is sensitive to liquid temperature. When a cavitation bubble is growing inside a liquid, the latent heat of vaporization can only be supplied by the liquid surrounding the cavitation bubble. As cavitation bubble grows, the local temperature of the cavitation bubble decreases as the temperature of surrounding liquid is decreased as represented in Fig. 1.10. Thus, the corresponding vapor pressure of the cavitation bubble is decreased as well. This phenomenon is referred to as the "thermal effects". The cavitation bubble growth is determined by an effective cavitation number defined as a pressure difference between the bulk liquid pressure and the vapor pressure of the cavitation bubble.

$$\sigma_{eff} = \frac{p_\infty - p_{v,B}}{\frac{1}{2}\rho_l U^2} = \sigma + \frac{\Delta p_v}{\frac{1}{2}\rho_l U^2} \tag{1.3}$$

Thus, the effective cavitation number is larger than the nominal cavitation number because it considers the vapor pressure depression due to thermal effects. Therefore, the cavitation bubble is more suppressed when thermal effects exist. The thermal effect is significant in a hot water or cryogenic fluids such as a liquid oxygen or nitrogen where the flow properties are sensitive to temperature variations. On the other hand, thermal effects are usually neglected in a cold water where the influence of the temperature variation on the flow properties is small.

Thermal Effects with Temperature Variation

Previous researches related to thermal effects on cavitating inducer have been investigated at different temperature liquid. Ruggeri and Moore [42] measured cavitation performance for pumps and inducers in liquid hydrogen. The critical cavitation number decreased with increasing liquid temperature or decreasing rotational speed. Kikuta et al. [43] found that the critical cavitation number and cavitation region length were decreased as the liquid nitrogen temperature was increased.

Franc et al. [[6], [44]] observed the variations in cavitation region length at the inducer leading edge and the onset of cavitation instabilities with changes in the liquid (refrigerant R-114) temperature and rotational speed. As R-114 temperature increased, the leading edge cavitation region was shortened and rotating cavitation occurred at lower cavitation numbers. In R-114 (in which the thermal effect existed), the cavitation region was lengthened as the rotational speed increased, but the cavitation region length was insensitive to the rotational speed in cold water (in which the thermal effect was negligible).

Yoshida et al. [[45], [46]] investigated cavitation instabilities at different liquid nitrogen temperatures. They found the followings. First, rotating cavitation occurred at the same length of tip vortex leakage cavitation region regardless of temperature. Second, the onset cavitation numbers of rotating cavitation and asymmetric attached cavitation were decreased as the temperature of liquid nitrogen increased. Finally shaft vibration and rotating cavitation amplitudes were reduced at high liquid temperatures.

The thermal effects on cavitating inducer in water have also been investigated. Cervone et al. [47] conducted experiments on the influence of water temperature on cavitation instabilities in a 3-

bladed inducer. They found that 1) the intensity of cavitation surge was weaker at higher temperatures (343 K) than at lower temperatures (297 K); and 2) increasing temperature did not change either frequency or type of cavitation instabilities. Torre et al. [48] found that the critical cavitation number was higher when the water temperature is lower. On the other hand, the breakdown cavitation number was not affected by the increasing water temperature. They also found that the onset of asymmetric attached cavitation corresponded to the critical cavitation number. However, they did not show a clear relationship between the critical cavitation number and water temperatures, and how temperature change affects rotating cavitation.

Tokumasu et al. [49] performed a numerical simulation of a 2-D hydrofoil and found that the size of cavitation was smaller and temperature drop was smaller at a higher temperature liquid oxygen. Hosangadi et al. [50] numerically simulated cavitating hydrofoil in liquid hydrogen and liquid nitrogen. The amount of temperature drop was similar at different temperatures, and temperature drop increased as freestream velocity increased. Hosandadi et al. [51] also performed numerical simulations using their CFD code for liquid hydrogen and water in cavitating inducer. They found that the temperature drop in hydrogen fluid was on the about 0.5 K to 1.0 K for reference temperature of 20.55 K. Gonclaves et al [52] performed a numerical simulation of inducer cavitation in liquid hydrogen at different temperatures. They found that cooling effect due to cavitation was lower than heating effect due to viscosity.

Thermal Effects with Non-dimensional Thermal Parameter

Alternatively, to quantify such thermal effects, several parameters have been suggested. Stepanoff [53] used the B-factor, or the ratio of the vapor volume to the liquid volume in the vaporization process, to represent the temperature effects of liquids and adjust the difference in cavitation performance between water and other liquids. Brennen [11] suggested a dimensional thermal parameter, Σ ($m/s^{3/2}$), from the Rayleigh-Plesset equation (Eq. 1.2). The depression of temperature (ΔT) within the bubble due to the latent heat is expressed as below using conduction of heat flux.

$$\Delta T \cong \frac{\dot{R}\sqrt{t}}{\sqrt{\alpha_l}} \frac{\rho_v L}{\rho_l c_{pl}} \tag{1.4}$$

The vapor pressure depression due to the latent heat is also expressed as below from Clausius-Clapeyron relation.

$$\Delta p_v = \frac{L\rho_v}{T} \Delta T \cong \dot{R}\sqrt{t} \frac{(\rho_v L)^2}{\sqrt{\alpha_l}\rho_l c_{pl} T} \tag{1.5}$$

From thermal effects term in the Rayleigh-Plesset equation, Σ is derived as shown below. Σ represents the amount of vapor pressure depression due to the thermal effect in a fluid (Eq. 1.2).

$$\frac{p_v(T_B) - p_v(T_\infty)}{\rho_L} = \dot{R}\sqrt{t}\Sigma \tag{1.6}$$

$$\Sigma = \frac{(\rho_v L)^2}{\rho_l^2 C_{pl} T_\infty \sqrt{\alpha_l}} \tag{1.7}$$

Subsequently, for cavitation in fluid machines, Franc et al. [54] derived a non-dimensional thermal parameter, Σ^* (Eq. 1.9), by

nondimensionalizing the Rayleigh–Plesset equation (Eq. 1.2). For simplicity, they assumed inviscid flow and neglected the surface tension.

$$\bar{R}\frac{d^2\bar{R}}{d\bar{x}^2}+\frac{3}{2}\left(\frac{d\bar{R}}{d\bar{x}}\right)^2+\Sigma^*\sqrt{\bar{x}}\frac{d\bar{R}}{d\bar{x}}=-\frac{Cp+\sigma}{2} \tag{1.8}$$

$$\Sigma^*=\Sigma\sqrt{C/U^3} \tag{1.9}$$

In Eq. 1.8, the bubble radius (R) and the distance (x) have been non–dimensionalized by the characteristic length C. Cp is the pressure coefficient, and σ is the cavitation number. In addition to the fluid properties of Σ, Σ^* incorporates the characteristic length (C) and reference velocity (U) of the pump representing the amount of the thermal effect on cavitation in fluid machines. In Eq. (1), as the temperature of the working fluid increases, the vapor density increases faster than the increase in the temperature. Thus, Σ is increased. According to Eq. 1.7 and 1.9, Σ^* is increased as the liquid temperature increases or the reference velocity decreases. In actual rocket engines using liquid oxygen, Σ^* ranges from 1.5 to 30 depending on the size and rotational speed of the inducer.

Cooper [55] developed an analytical model for temperature effects on inducer cavitation performance using the B–factor. Watanabe et al. [[56], [57]] developed an analytical model to simulate temperature effects using singularity analysis to investigate the cavitation in an inducer cascade. They suggested the non–dimensional thermal parameter, Σ^*, in a different way. They found that 1) as Σ^* increases, the onset cavitation number of cavitation instabilities moved toward lower cavitation number; 2) temperature effects were more significant at higher temperatures,

and temperature effects became larger as the cavitation bubble becomes longer due to the need of larger latent heat. Kikuta et al. [58] investigated the rotational speed effects using Σ^* in liquid nitrogen. The cavitation region length and critical cavitation number both decreased as Σ^* increased.

Hot water can be used as a surrogate test fluid for cryogenic oxidizer or propellant when it satisfies the similarity requirement in terms of the non-dimensional thermal parameter. Ehrlich and Murdock [59] derived their DB parameter, which is a reciprocal of Σ^*, and they matched their DB value in water with that of liquid oxygen. In water, they found that decreasing DB completely suppressed rotating cavitation. They tried to match DB with different temperature and rotational speeds. But their results showed that the cavitation performance is different even though DB values are same at different temperature and rotational speed. It gave the clue that the non-dimensional thermal parameter is not the only parameter to satisfy the similarity in terms of thermal effects.

1.3. Research Objectives

Despite of such efforts listed above, the cause and mechanism of rotating cavitation is still unclear. Especially, experimental approaches to understand rotating cavitation mechanism such as flow field measurement under rotating cavitation has not been performed. Thus, only numerical approaches has been performed until now. However, CFD simulation still cannot predict cavitation phenomenon exactly in 3-D rotating inducer. Therefore, the rotating cavitation results from the CFD simulations need experimental validations. The first objective of this study is to investigate the cause and mechanism of rotating cavitation through experimental method.

Previous researchers investigated the thermal effect on cavitating inducers by varying either the liquid temperature or rotational speed, but they did not consider viscous effects. When either the liquid temperature or rotational speed is changed, not only Σ^* but also the Reynolds number is simultaneously changed. Yet, the individual effects of Σ^* and Reynolds number on the cavitation instability onset have not been examined. Therefore, the second research objective of this study is to evaluate and understand the individual effects of Σ^* and Reynolds number on the onset of rotating cavitation.

Following hypotheses are formulated based on the literature review and going to be confirmed through experimental methods. First, incidence angle change due to the tip leakage vortex cavitation induces rotating cavitation. This hypothesis is based on

the CFD simulation results from Kang et al. [40] and Tani et al. [41]. Incidence angle measurement near the leading edge of the inducer tip is performed. Second, Σ^* and Reynolds number play an important role on rotating cavitation onset. From the Rayleigh–Plesset equation, non–dimensional parameters which affect cavitating inducer are derived. Σ^* effect at constant Reynolds number and Reynolds number effect at constant Σ^* on rotating cavitation onset are examined separately.

1.4. Scope and Organization

The scope of this study is limited to the experiments. While the flow field, unsteady pressure, visualization of cavitating inducer have been measured, numerical simulation for rotating cavitation and thermal effects was not done.

To achieve the research objectives, axial velocity and tangential velocity are required at the same time. Thus, PIV (Particle Image Velocimetry) measurement method has been adapted to measure 2-D velocity near the tip region.

Also, to investigate non-dimensional parameter effects on rotating cavitation, experiments have been conducted on a combination of various combination of temperature and rotational speed conditions.

In addition, the inlet flow distortion effects using S-shaped inlet also have been measured and shown in Appendix.

This dissertation is organized in five chapters. The chapters are individually described below.

Chapter 1 introduces fundamentals of cavitation, turbopump inducer, and types of cavitation instability occurring in cavitating inducer. Previous works on rotating cavitation and thermal effects are reviewed and research objectives of this study are presented.

Chapter 2 describes the design process of the test facility constructed in Seoul National University including detailed design of each components, rotordynamic analysis and selection of instrumentations. Inducer performances under cavitating and non-

cavitation conditions are determined. Visualization of inducer cavitation phenomenon is presented. Cavitation instabilities occurring at the test inducer is also identified.

Chapter 3 presents the experimental results from PIV measurement to understand rotating cavitation. Flow fields under the rotating cavitation condition are presented. The cause and pulsation mechanism of rotating cavitation are discussed using experimental data.

In Chapter 4, the effects of two non-dimensional parameters on rotating cavitation are presented. Based on the experimental results under various conditions of water temperature and rotational speed, thermal effects on rotating cavitation onset are evaluated.

Chapter 5 summarizes the results and new conclusions of this study. Recommended future works are also presented.

Figure 1.1 75 ton turbopump developed by Korea Aerospace Research Institute.

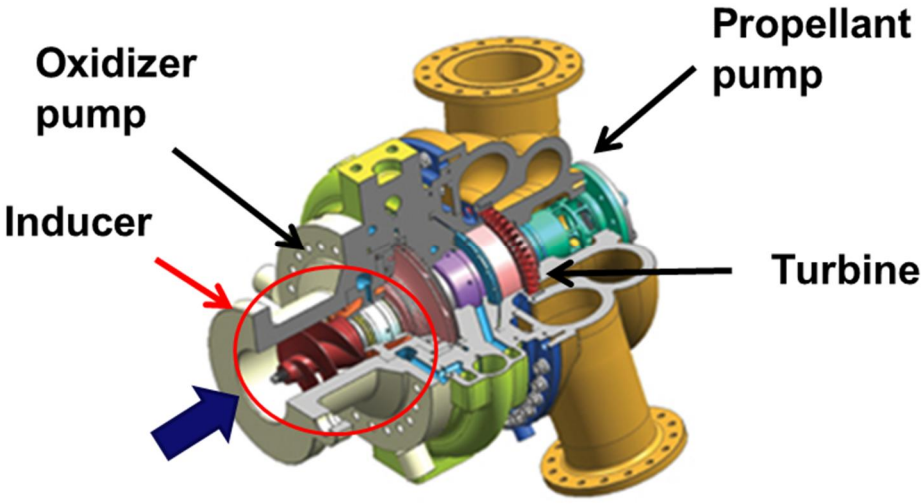

Figure 1.2 Schematic of turbopump [1].

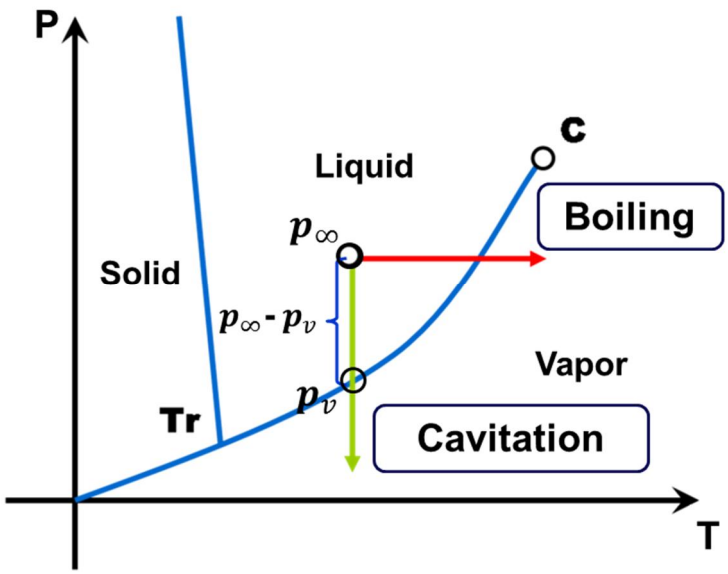

Figure 1.3 Pressure−Temperature phase diagram.

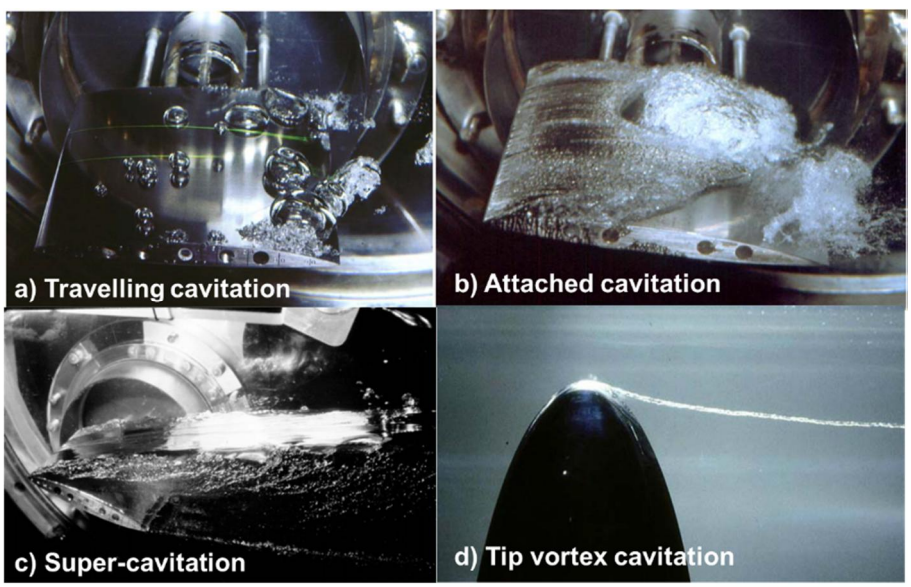

Figure 1.4 Types of Cavitation [5]: a) Travelling vortex cavitation, b) Attached cavitation and unsteady sheet cavitation, c) Super−cavitation, and d) Tip vortex cavitation.

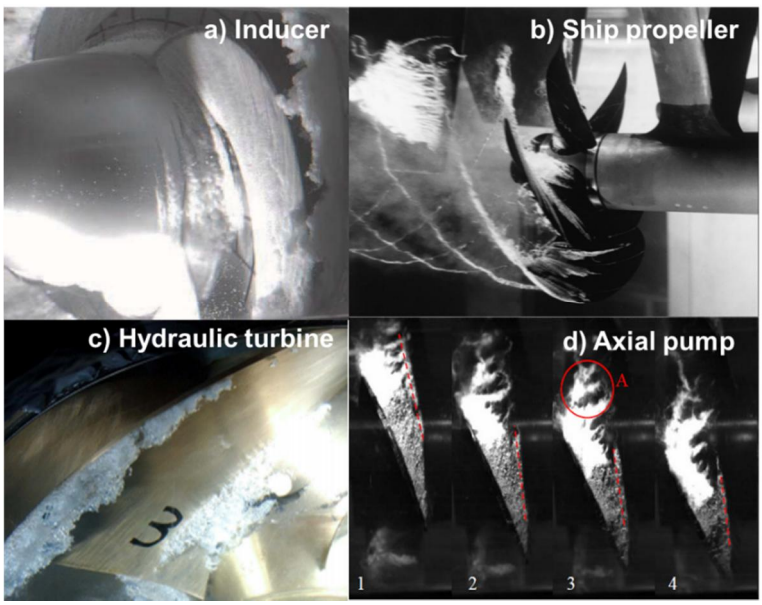

Figure 1.5 Cavitation in various turbomachinery: a) inducer cavitation [6], b) ship propeller cavitation [7], c) hydraulic turbine cavitation [8], and d) centrifugal pump impeller and erosion due to cavitation [9].

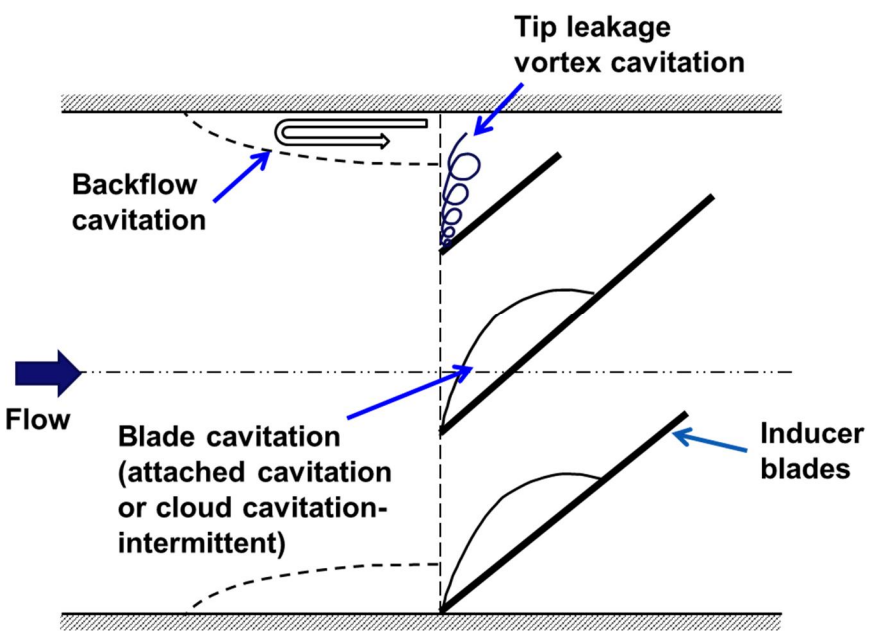

Figure 1.6 Inducer cavitation phenomenon (re-drawn from [11]).

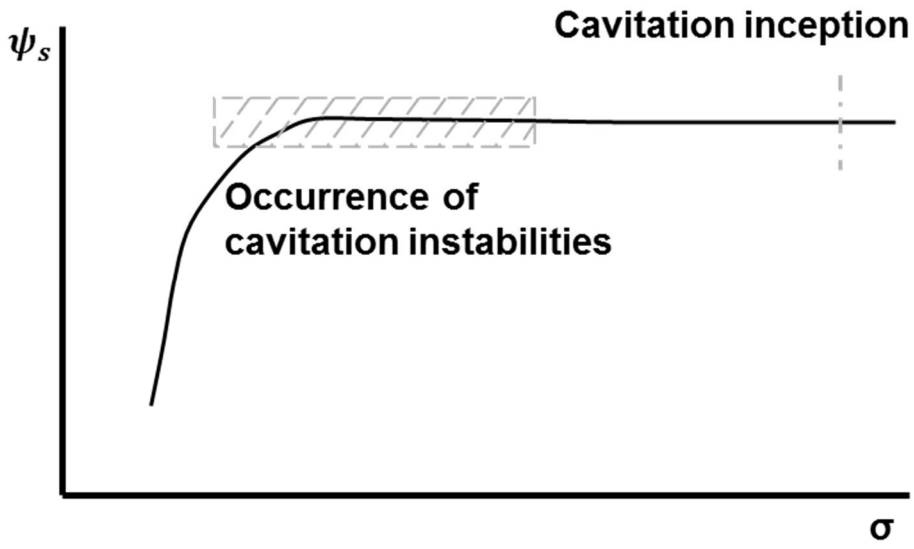

Figure 1.7 Cavitation performance.

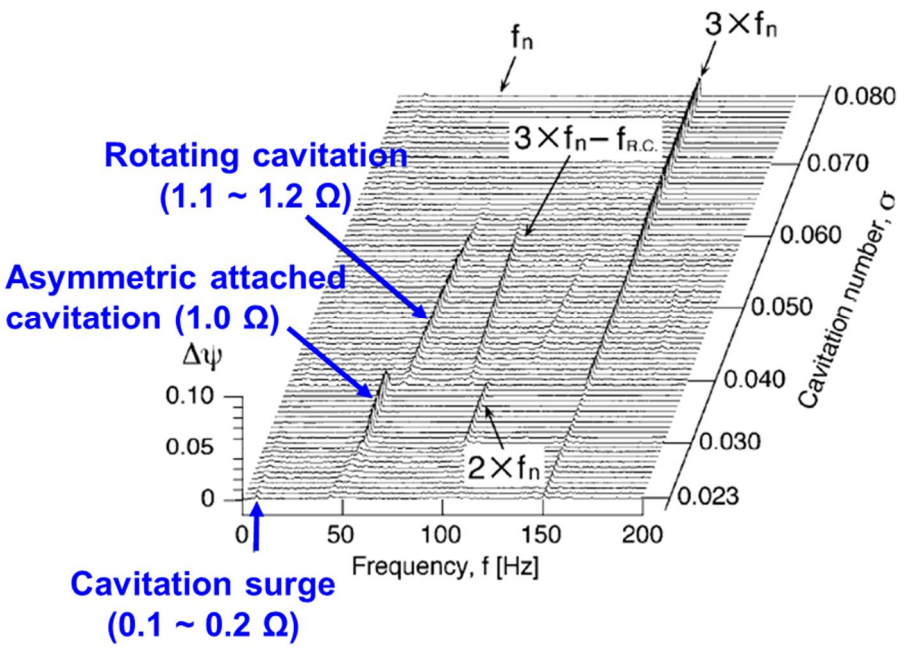

Figure 1.8 Detection of cavitation instabilities– Power spectrum density of inducer inlet pressure fluctuations [12].

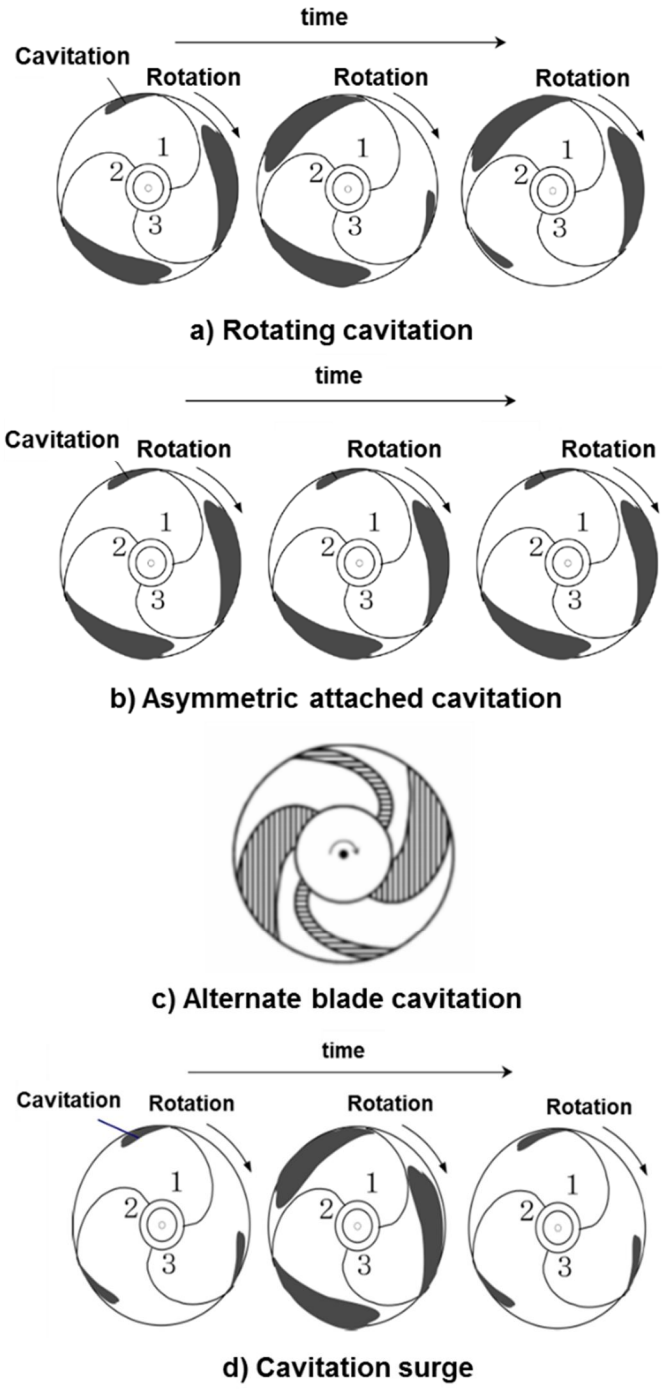

Figure 1.9 Types of cavitation instabilities; (a) rotating cavitation, (b) asymmetric attached cavitation, (c) alternate blade cavitation, and (d) cavitation surge.

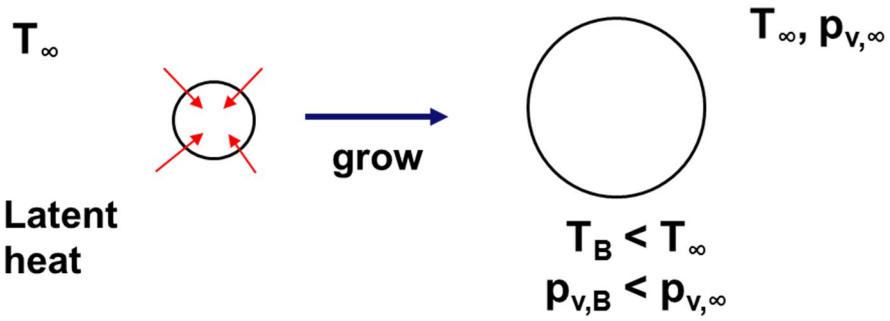

Figure. 1.10 Thermal effects on cavitation bubble growth.

Chapter 2. Experimental Apparatus

2.1. Design of the Test Facility

2.1.1. Design Procedure

The turbopump inducer water test facility at Seoul National University has been designed and built to measure cavitating and non-cavitating inducer/pump performance and unsteady phenomenon over a wide range of operating conditions. Figure 2.1 shows the design procedure of the test facility. Firstly, non-dimensional parameters needed for measurement and design are selected and calculated. The range of non-dimensional parameters has been determined based on constraints and design values. Thus, the operating ranges of the test facility have been determined. With reference to the existing experimental apparatus, the components of the test facility have been selected considering the purpose of the experiments.

The purpose of the test facility is 1) to measure the performance under cavitating and non-cavitating condition; 2) to measure the instability induced by cavitation; 3) to visualize the cavitating inducer; 4) to employ the laser measurement method; 4) to measure the thermal effects on cavitation performance and cavitation instability; and 5) to install the S-shaped inlet to measure inlet distortion effects on cavitation performance and cavitation instability. Thus, the test facility needs to have ability to

sustain cavitating and high temperature condition and change in pressure, temperature, and rotational speed. It also needs to have transparent test section for visualization. S-shaped inlets also needs to install (the inlet distortion effects will be shown in Appendix F).

For the detailed component design, the specifications of the components that satisfy the calculated operating ranges have been selected. Detailed rotating part design including a shaft, a seal, and bearings has been validated through rotordynamic analysis. For instrumentation design, types of sensors need to measure for obtaining non-dimensional parameters have been selected. For the operating ranges, specifications of the sensors can be determined. Based on the uncertainty analysis and cost, instrumentation has been determined.

The author have established the design of a test facility and test plans based on test facilities which were published in various research institutes such as Aerospace Corporation [60], Pisa University [[61], [62]], Osaka University [[18], [25]], Japan Aerospace Exploration Agency (JAXA) [63], California Institute of Technology (Caltech) [64], and Korea Aerospace Research Institute (KARI) [65]. The test facilities from other institutes are summarized in Table 2.1 and the pictures are shown in Appendix A. The strengths and weaknesses of each test facility have been analyzed considering the purpose of the experiments, and the test facility in SNU was constructed based on the analysis.

2.1.2. Non-dimensional Parameters for Design the Test Facility and Operating Ranges

Followings are the non-dimensional parameters to consider in the design process; Cavitation number (σ), flow coefficient (ϕ), head coefficient (ψ), non-dimensional thermal parameter (Σ^*), Reynolds number (Re), Mach number (Ma). Definitions of each non-dimensional parameter are as follows.

$$\sigma = \frac{P_{inlet} - P_v}{\frac{1}{2}\rho_l (r_1\ \omega)^2} \tag{2.1}$$

$$\phi = \frac{Q}{A r_1 \omega} \tag{2.2}$$

$$\psi = \frac{P_2^T - P_1^T}{\frac{1}{2}\rho_l (r_1 \omega)^2} \tag{2.3}$$

$$\Sigma^* = \frac{1}{R\omega^{3/2}} \frac{(\rho_v\ L)^2}{\rho_l^2 \sqrt{\alpha_l} c_{p,l} T_\infty} \tag{2.4}$$

$$Re = \frac{2\rho_l r_1^2 \omega}{\mu} \tag{2.5}$$

$$Ma = \frac{r_1 \omega}{c} \tag{2.6}$$

Cavitation number which usually quantifies the degree of the cavitation occurrence represents a margin before flow begins to cavitate. Flow coefficient is the ratio of the flow rate to rotational speed, head coefficient represents the amount of pressure rise in the inducer. Non-dimensional thermal parameter represents the amount of thermal effects, which is proportional to the amount of the vapor pressure depression (Δp_v). Reynolds number and Mach number represent the viscosity effect and compressibility, respectively. Conventionally, cavitation number, head coefficient,

and flow coefficient are used to establish dynamic similarity of experiments between a real engine and a water test facility. For thermodynamic similarity, non-dimensional thermal parameter needs to be considered.

The test inducer as shown in Fig. 2.2 has been designed and provided by Korea Aerospace Research Institute (KARI) [65]. The 3-bladed inducer has a high solidity and moderate blade tip angle at the inlet. The design flow coefficient is 0.096. Its specifications are summarized in Table. 2.2.

There is a variation in cavitation number due to the pressure difference above and below the pipe, because the test facility is horizontal, Figure 2.3 shows the cavitation number gradient magnitude according to the mean inlet cavitation number. As rotational speed increases, the difference of the cavitation number is decreased. For σ = 0.06, the difference at above the 5,000 rpm is lower than 5 %. Thus, inducer rotational speed needs to be higher than 5,000 rpm.

The critical speed (Eq. 2.7) [66] needs to be considered. From Eq. 2.7, E is modulus of elasticity, I is moment of inertia, γ is specific weight, g is gravitational constant, and l is shaft length.

$$\omega_1 = \left(\frac{\pi}{l}\right)^2 \sqrt{\frac{gEI}{A\gamma}} \tag{2.7}$$

The calculated critical speed is 10,600 rpm. Considering the safety factor and the cavitation number difference, 5,000 rpm was determined as the target rotational speed.

Reynolds number and Mach number also needs to be considered. There is Reynolds number effects on the efficiency ratio of the

inducer [67]. When Reynolds number is larger than 10^6, hydraulic efficiency and shaft efficiency ratio are constant at 1 as shown in Fig. 2.5. At the target rotational speed, 5,000 rpm, Reynolds number is 2.58×10^6, thus, the Reynolds number effects is negligible. Also, Mach number is 0.01, thus, the flow is considered to be incompressible and neglected compressible effects. Non-dimensional parameters at the design rotational speed are summarized in Table. 2.3.

The operating range requirements for flow coefficient and cavitation number is ϕ/ϕ_d = 0.8~1.1 and 0.03 ~ 0.5 respectively based on the typical operating ranges of turbopumps. The non-dimensional thermal parameter is a key consideration of the test facility operating temperature range. For the real liquid rocket engine conditions (liquid oxygen, 87K and 20,000 rpm), Σ^* is 1.81. To satisfy the thermodynamic similarity, Σ^* for the test case needs to be similar to the real engine value. Figure 2.4 represents the Σ^* values according to the water temperature. For 5,000 rpm and 83 ° C, Σ^* is 1.80 which can simulate cryogenic conditions. Thus, the test facility should be designed to endure the temperature up to 83 ° C.

2.1.3. Rotating Part Design

Figure 2.6 presents the detailed schematic of rotating parts. Rotating parts are composed of the test inducer, shaft, and motor. The initial shaft design was based on the test facility of KARI. The bearing and seals are selected and rotordynamic analysis performed to validate the safety of the shaft design.

Bearings are selected to endure the axial and radial force during

the experiments. Based on the force balance, the rated load and rating fatigue life have been calculated. Types of front and back side bearings are angular contact bearing and deep groove bearing. The selected bearings can be used semi-permanently by increasing the margin of the life time. Mechanical seal is applied to block the leakage from the collector to the bearings.

Figure 2.7 shows the schematic of the shaft. The length and diameter of the shaft is determined by considering the critical speed as shown in Eq. 2.7. A simple rotordynamic analysis has been performed using the ANSYS program. The process of rotordynamic analysis is shown in Fig. 2.8. A simplified geometry which treats the inducer as big disk is used and the mesh is created at the geometry. For the boundary condition, fix surface is given at both ends. The rotational speed and boundary conditions are given. Stiffness and damping values based on the bearing characteristics are also given to simulate bearing conditions. The material is stainless steel.

Modal analysis for the loading conditions has been performed. Figure 2.9 shows the modal analysis results. The first mode occurs at 170.74 Hz (10,244 rpm) which is similar to calculation by the critical speed (Eq. 2.1). The second and third modes are 1,237.9 Hz (74,274 rpm) and 1,392.5 Hz (83,550 rpm) respectively. The system is thought to be safe if the resonance margin rate, $\epsilon = \frac{|rotational\ speed - natural\ frequency|}{rotational\ speed}$, is above 0.5. At 5,000 rpm ϵ is 0.92, which indicates a safe design. The maximum safe rotational speed is 6,700 rpm (ϵ = 0.5). Stress and deformation analysis also have been conducted as shown in Fig. 2.10 and 2.11. From the stress analysis at 5,000 rpm condition, the stress and deformation of the shaft are also calculated. The maximum stress of the shaft is 3.32

MPa which is much lower than shaft yield stress (736 MPa). The maximum deformation of the shaft is 4.4×10^{-3} mm, which is much smaller than the casing tip clearance. The rotordynamic analysis results are summarized in Table 2.4. The safety of the test facility is verified through rotordynamic analysis.

2.2. Components of the Test Facility

Figure 2.12 shows a schematic of the turbopump inducer water test facility at Seoul National University. The closed loop test facility includes a water tank, test section, rotating part, flow straightener, control valve, and booster pump. Rotating part includes the inducer, shaft, collector, and motor.

2.2.1. Flow Loop Component Design

A water tank capacity is not required to be large because an inducer water test does not require high power. Thus, the water tank has a 0.9 m^3 capacity. A vacuum pump and compressed air supply pipe are connected to the water tank to control pressure. To adjust the water temperature, a 20-kW electrical heater has been employed in the water tank. The inlet of the water tank is curved to swirl incoming flow as shown in Fig. 2.12, thereby eliminating bubbles in the water. To give a variety of inlet curvature shapes (changes in radius of curvature), three exits have been installed at the water tank. Straight duct and 1.0 D and 1.5 D radius of curvature duct can be installed in order to distort incoming flow for

inlet distortion experiments (Appendix F). A honeycomb and a screen have been installed at each outlet to flow make uniform.

The filtered water from the tank is circulated in the direction shown in Fig. 2.6. The length of the straight section from the water tank to the test section is 35 pipe diameters to eliminate the effect of pulsation from the water tank. An electrical automatic flow control valve have been installed downstream of the inducer for accurate and convenient flow control. To inhibit the occurrence of cavitation at the valve, a globe valve which deters cavitation at the valve have been selected. Downstream of the collector, Straightener also have been located 10 pipe diameters upstream of the flow meter for accurate flow rate measurement. Farther downstream, the booster pump is installed to maintain a constant flow rate under cavitating conditions. From the simultaneous operation of booster pump and control valve, it is able to maintain constant flow coefficient at every measurement points, thus, the flow coefficient effect can be negligible during the experiments. Elastic couplings have been installed at the exit of the water tank and collector for alignment and vibration control.

The flow passing the inducer goes to the collector through the diffuser. The diffuser principle is identical to a centrifugal pump diffuser, so the diffuser has been designed with the same design process as the centrifugal pump [[68], [69]].

$$r_{diffuser} = (1.55 + \varphi) r_2 \tag{2.8}$$

$$CP_i = cos^2\alpha_2 \left(1 - \frac{1}{AR^2}\right) + sin^2\alpha_2 \left(1 - \frac{1}{RR^2}\right) \tag{2.9}$$

Following these equations and reference, diffuser inlet radius,

exit radius, and the ratio of the width of inlet and outlet have been designed. The design of the collector has been followed the CFD analysis performed by Kang et al. [70]. The non-uniformity based on the impeller exit pressure is 0.03 % when the collector cross-section is 0.3 m X 0.3 m. Thus, the author have adapted this to design of the collector and the final collector design is shown in Fig. 2.6.

2.2.2. Test Section

The configurations of casings with and without the inducer upstream enlargement ramp used in this study are shown in Fig. 2.13 and 2.14. The casing with the enlargement ramp is applied to investigate thermal effects which will be discussed in Chapter 3. The casing without the enlargement step is used in Particle Image Velocimetry (PIV) measurement which will be discussed in Chapter 4. The ramp is usually applied to suppress the cavitation instabilities. The geometry of the ramp is obtained from KARI. R_1 is the casing inlet radius upstream of the step, r_2 is the casing inlet radius at the inducer tip leading edge and r_3 is the casing inlet radius downstream of the inducer. γ is the slope angle of the casing from R_1 to R_2. The slope starts from 4.6 mm upstream from the inducer tip leading edge. Both casings has the same tip clearance, thus the effects of tip clearance are negligible. The detailed geometry information is summarized in Table 2.5.

2.3. Instrumentation

2.3.1. Uncertainty Analysis

To obtain performance of the inducer under cavitating and non-cavitation condition, cavitation number, head coefficient, and flow coefficient should be measured. To identify cavitation instability, unsteady pressure measurement is also required. Required non-dimensional parameters and variables, device to measure the variables, and locations are summarized in Table 2.6. To obtain flow coefficient, flow rate and rotational speed are required. For cavitation number, inlet pressure, rotational speed, and water temperature need to be measured. For head coefficient, inlet and outlet pressure, rotational speed, and water temperature are needed. To measure the non-dimensional thermal parameter, water temperature and rotational speed are required. To get the inlet and outlet pressure, pressure transducers are installed upstream and downstream of the inducer. Flow rate is measured through the electric-magnetic type flow meter. Bulk flow temperature is obtained at the water tank. An encoder is used to measure rotational speed.

Measurement accuracy and uncertainty influence the capacity of the test facility and the reliability of the results. To balance the cost with accuracy, an uncertainty analysis for non-dimensional parameters is required before selecting instrumentations. The uncertainty analysis indicates the accuracy of the total instrumentation system. Normalized uncertainties for cavitation number, head coefficient, non-dimensional thermal parameter, and flow coefficient are given by:

$$\frac{u_\phi}{\phi} = \left[(\frac{u_Q}{Q})^2 + \left(\frac{u_\omega}{\omega}\right)^2 \right]^{0.5} \quad (2.10)$$

$$\frac{u_\sigma}{\sigma} = \left[(\frac{u_{P_{inlet}}}{P_{inlet}-P_v})^2 + \left(\frac{u_{P_v}}{P_{inlet}-P_v}\right)^2 + \left(\frac{u_\rho}{\rho}\right)^2 + \left(\frac{-2u_\omega}{\omega}\right)^2 \right]^{0.5} \quad (2.11)$$

$$\frac{u_\psi}{\psi} = \left[(\frac{u_{P_2}}{P_2})^2 + (\frac{-u_{P_1}}{P_1})^2 + (\frac{u_{V_2}}{V_2})^2 + (\frac{-u_{V_1}}{V_1})^2 + \left(\frac{-2u_\omega}{\omega}\right)^2 + \left(\frac{u_\rho}{\rho}\right)^2 \right]^{0.5} \quad (2.12)$$

$$\frac{u_{\Sigma^*}}{\Sigma^*} = \left[\begin{array}{c} \left(\frac{3u_\omega}{2\omega}\right)^2 + \left(\frac{2u_{\rho_l}}{\rho_l}\right)^2 + \left(\frac{u_{c_{pl}}}{c_{pl}}\right)^2 + \left(\frac{u_T}{T}\right)^2 + \left(\frac{u_\alpha}{2\alpha}\right)^2 + \\ \left(\frac{-2u_{\rho_g}}{\rho_g}\right)^2 + \left(\frac{-2u_{h_{fg}}}{h_{fg}}\right)^2 \end{array} \right]^{0.5} \quad (2.13)$$

Figure 2.15 presents the uncertainty of non-dimensional parameters according to key parameter accuracy. Pressure sensor accuracy strongly influences the cavitation number and head coefficient uncertainties. The flow coefficient are sensitive to accuracy of the flow meter. For the non-dimensional thermal parameter, variables are dependent on water temperature except rotational speed. But, the uncertainty of the non-dimensional thermal parameter is insensitive to the inlet temperature. Based on the uncertainty analysis results, accuracy of pressure sensor and the flow meter should be prioritized, with less emphasis on accurate temperature measurement. The measurement range has also been considered before the selection of instrumentation.

2.3.2. Specifications and Location of Measurement Instrumentation

The SNU test facility has been equipped with appropriate

instrumentation to accurately measure and control the important parameters described above. The test section schematic is shown in Fig. 2.13 and 2.14. Eight and four static pressure transducers (Druck, PMP 5073) with an accuracy of 0.04 % full scale (200 kPa (P_1) and 400kPa (P_2)) have been installed at x/D = −1.0 (P_1) and x/D = 0.75 D (P_2) from the inducer tip leading edge to measure the inducer static head coefficient and cavitation number. Eight unsteady pressure transducers (Kulite, HEL−375−100A) with an accuracy of 0.1 % of the full scale value (350 kPa) and 400 kHz frequency response have been installed at x/D = −0.25 and 45° intervals in the circumferential direction to identify cavitation instabilities. During the experiments, unsteady pressure signal acquisition rate is 50 kHz and it has been received during 1 second for each measurement point. An electro−magnetic flow meter (Foxboro, IMT 25) is used to measure flow rate non−intrusively with 0.25 % accuracy and 0~20 L/s measurement range. An encoder (Baumer, HOG 9) is installed at the motor shaft to measure rotational speed and give a synchronized signal, which send a signal with 1024 pulse/rev. Torque−meter (MEAS, UTM−300) has been installed between the shaft and the motor to measure the torque and rotational speed. Bulk water temperature has been measured in the water tank with an accuracy of ±0.1 K. In order to consider the safety, an accelerometer (PCB 352C34) has been installed on the bearing housing to measure the vibration of the test facility during the experiment. The detailed specifications of measurement devices are described in Table. 2.7.

Inducer cavitation phenomenon is difficult to observe by CFD. Thus, the visualization of the inducer cavitation is important to understand the phenomenon. A transparent test section was made

of fabricated acryl to obtain visualization data of the inducer cavitation. For visualization of the inducer cavitation, a high speed camera (Photron, FASTCAM Mini UX 100) has been used. Figure 2.16 shows the high speed camera and the light set-up for the visualization. Inducer cavitation pictures have been acquired at a speed of 5,000 fps (6° per picture) and 1,280 x 1,000 pixels.

2.3.3. Specifications of Data Acquisition System

The data Acquisition (DAQ) system is another important component affecting accuracy. Considerations for DAQ system are resolution and channels. The resolution of the DAQ system should be better than the sensor accuracy to read the sensor signal accurately. The number of channels should be sufficient to connect all the sensors.

AD boards from National Instrument with 16 bit and sampling rate of 350 kS/s are used to obtain static pressure transducer signals (NI 9205) and flow rate signals (NI 9203). Unsteady pressure signals are amplified by amplifier from TEAC and acquired by an oscilloscope (Yokogawa, DL 750) with 12 bit. Non-dimensional parameters are monitored and measured in real time with LabView software. The detailed specifications of data acquisition system are described in Table. 2.8.

2.3.4. Measured Uncertainty

Uncertainty of measured non-dimensional parameters has been acquired based on general uncertainty analysis method [71]. For a

Gaussian distribution with mean μ and standard deviation σ,

$$\text{Prob}\ (\ X_i - 1.96\,\sigma\ \leq\ \mu\ \leq\ X_i + 1.96\,\sigma\ ) = 0.95 \qquad (2.14)$$

For a single data (X_i), μ is within $\pm$ 1.96 σ with 95% confidence interval.

For the mean $\bar{X}$ of a sample population of size N is itself normally distributed with standard deviation $\sigma/\sqrt{N}$,

$$\text{Prob}\ (\bar{X} - 1.96\frac{\sigma}{\sqrt{N}}\ \leq\ \mu\ \leq\ \bar{X} + 1.96\frac{\sigma}{\sqrt{N}}) = 0.95 \qquad (2.15)$$

For the sample mean $\bar{X}$ computed from N readings, μ is within $\pm$ 1.96 $\sigma/\sqrt{N}$ with 95% confidence interval.

When sample standard deviation S_x is used instead of standard deviation σ, because we do not know σ, we use S_x as an estimate of σ.

$$\text{Prob}\ (-t\ \leq\ \frac{X-\mu}{S_X}\ \leq\ t) = 0.95 \qquad (2.16)$$

The variable $(X-\mu)/Sx$ follows t distribution with N−1 degrees of freedom. Thus, the values of t are functions of the size N of the sample population. Therefore,

$$\text{Prob}\ (\ X_i - P_x\ \leq\ \mu\ \leq\ X_i + P_x\ ) = 0.95\ (\ P_x = tS_x) \qquad (2.17)$$

When the inducer rotates at 5,000 rpm, 61 data of inlet pressure, outlet pressure and flow rate have been acquired. The uncertainty of each parameter with 95 % confidence interval is as follows − $\pm$ 0.00398 in ψ; $\pm$ 0.000422 in ϕ; and $\pm$ 0.000759 in σ.

2.4. Particle Image Velocimetry (PIV) Equipment

2.4.1. Component of PIV Set-up

PIV measurement system is composed of light source, image recorder (camera), light sheet optics, and synchronizer as shown in Fig. 2.16 and Fig. 2.17. The detailed specifications and pictures of PIV measurement system components are summarized in Table. 2.9 and Appendix E, respectively.

Light source

In this study, the double-cavity Q-switched Nd:YAG Laser (New Wave Solo) has been used in PIV measurement. The schematic of double-cavity Nd:YAG laser is shown in Fig. 2.18. The laser generated the cavity is originally 1064 nm. After the light passes the harmonic generator and harmonic separator, it transforms into green, visible light (532nm). Using the Q-switch time sequence, the delay between two laser pulses can be easily controlled. Nd:YAG lasers are classified as Class 4 radiation hazards, thus, the user needs to consider the safety. The diameter of the laser is 4 mm.

Image recorder

CCD camera (PCO Sensicam) with 1376x1040 pixels (pixel size: 6.45 μm x 6.45 μm) has been used as an image recorder. Images are transferred via the PCI-board (PCO, Model 525KP, PCI Local Bus compatible) to the computer. 'Cam Ware' software has been used to setup and record the images. In double frame mode, the maximum repetition rate is 10 Hz and the rate can be controlled from the synchronizer signal. The exposure times of the first and second frame are 54 μs and 1,000 μs, respectively. The minimum time interval between the first frame and second frame (dead time) is 0.5 μs. Focal length and f-number of the camera lens (Nikon) used in this study are 45 mm and 4, respectively.

Light sheet optics

The laser sheet optics are composed of cylindrical lens mirror with a Nd:YAG laser coating. Using the original optics, the laser sheet thickness is about 4 mm. To make narrow laser sheet, a slot has been installed before the laser sheet enters the inducer acryl casing.

Synchronizer

A synchronizer (Quantum composers 9518+ pulse generator) with 8 independent signal output channels has been used to give time sequence signal. Resolution and accuracy are 1 ns and 1 ns + .0001 delay. It can be triggered by external signal. A TTL output signal is generated on each output channel configured as follows.

A: CCD camera signal

B: Flash lamp (laser 1)

C: Q-switch (laser 1)

D: Flash lamp (laser 2)

E: Q-switch (laser 2)

The time sequence have been configured as shown in Fig. 2.19. The 'Q-switch 1 out' signal and 'Q-switch 2 out' signal must be located during the first the first and second camera exposure time, respectively. The time interval (Δt) is determined by the difference between the 'Q-switch 1' signal and 'Q-switch 2' signal. Power of two laser pulses is also determined by the difference between 'lamp trigger' signal and 'Q-switch' signal. Usually, the first picture is brighter than the second picture because the second exposure time of the camera is always longer than the first exposure time.

Particle seed

In PIV measurement technique, velocity of the flow is determined based on the illuminated seeds. If the particle size is small, the image density is low. Contrary, if the particle size is large, it cannot follows the flow. Therefore, it is important to select the appropriate particle seeds for PIV measurement.

In the present study, silver coated hollow glass spheres with 10 μm diameter and 1.1 g/cm^3 density have been selected as particle seeds. Characteristics of various particle seeds which are able to use in liquid are summarized in Table 2.8. Silver coated hollow glass spheres is relatively close to being neutrally buoyant, bright

and relatively inexpensive.

For particle seed dynamics, Stokes number (Stk) is considered. Stokes number is the ratio of the characteristic time of the particle to the characteristic time of the flow. For Stk < 0.1, particles are considered to follow flow streamlines with less than 1% of tracing error. In this study, Stokes number is 0.003 with 10 μm diameter of silver coated hollow glass spheres.

$$\mathrm{Stk} = \frac{\tau_p V_l}{d_c} \tag{3.2}$$

where, τ_p = particle time constant

V_l = liquid velocity

d_c = fluid flow characteristic length

$$\tau_p = \frac{(\rho_l - \rho_p) d_p^2}{18 \rho_l \nu_l} \tag{3.3}$$

where, ρ_l= liquid density

ρ_p = particle density

d_p = particle diameter

ν_l = liquid dynamic viscosity

Inducer casing

For PIV measurement, casing without the upstream enlargement ramp (Fig. 2.14) has been used to avoid the refraction problem which might be occurred in the stepped casing. The casing is made of transparent acryl with 21 mm thickness.

Calibration target

Calibration should be preceded for PIV measurement. Thus, a calibration target picture is required when the test facility is filled with water. PIV measurement is performed in water, thus, it is required to take the calibration target picture when it is placed inside the water. Also, calibration target should be placed where the laser sheet passes. When the calibration target is placed in the acryl casing, it must not scratch the casing. Calibration target has been designed and located to satisfy such requirements as shown in Fig. 2.20. L-shaped calibration target (34.76 mm (height) × 80 mm (length)) is placed on another L-shaped base. It can be moved in the axial direction, so when the calibration target is attached to the inducer casing at 0.95 radius of the inducer. And the axial position can be changed by the position of the calibration target. 2 mm grid is engraved on the calibration plate to give the calibration picture. The precision measurement for the length between grids has been performed. Calibration plated placed inside the acryl casing with water is shown in Fig. 2.21.

There might be a distortion due to the cylinder shaped casing. Thus, pixels at each grid need to be calculated whether the distortion exists or not. The measured pixel at each grid is 43 pixel ± 1 pixel. Therefore, the distortion is disregarded.

Tilted laser

At first, laser sheet is shot in a vertical direction. Figure 2.22 shows the raw image of PIV measurement for the vertical laser sheet. The lower part of the cavitation region (red circle area) is

dark because cavitation region blocks the laser sheet, and particles are rarely observed. Even though the cross-correlation of interrogation area has a peak in the dark region, the dark region needs to be minimized. Therefore, the laser sheet is tilted with about 40° . To give tilted laser, the structure of the laser sheet optics support is re-designed as shown in Fig. 2.23.

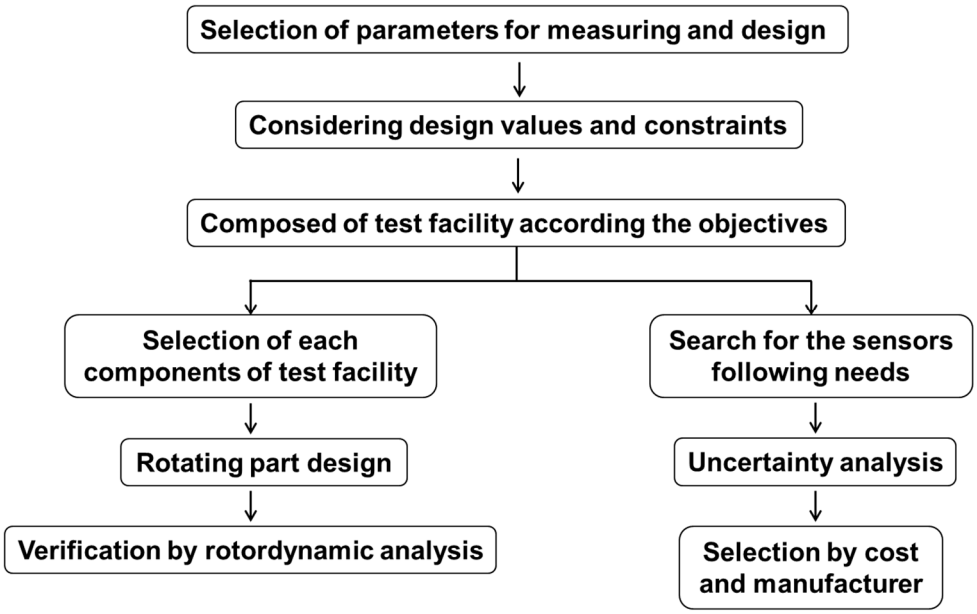

Figure 2.1 Design procedure of the test facility.

Figure 2.2 Test inducer.

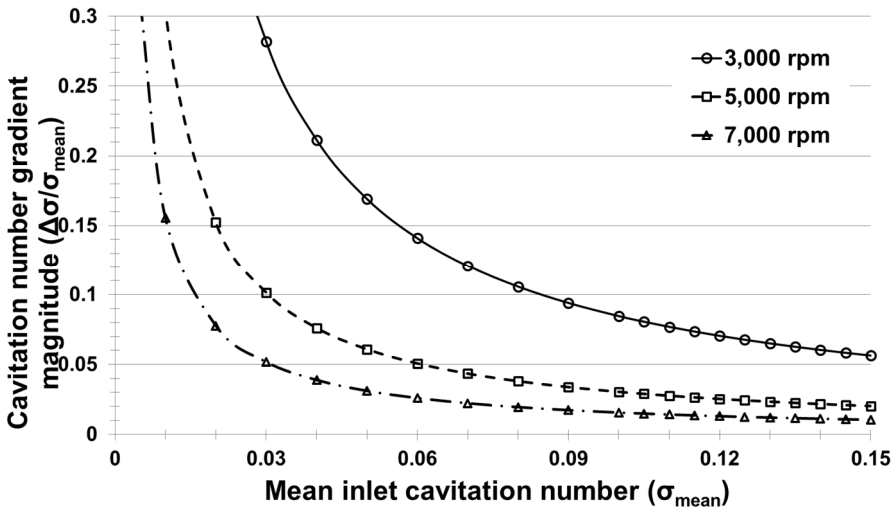

Figure 2.3 Cavitation number difference between top and bottom of the pipe versus the mean inlet cavitation number.

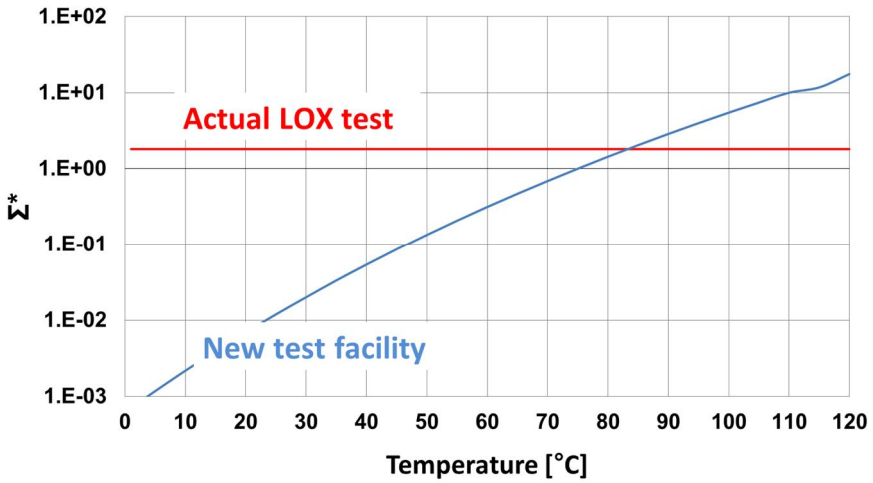

Figure 2.4 Non-dimensional thermal parameter for the new test facility and actual liquid rocket engine with liquid oxygen.

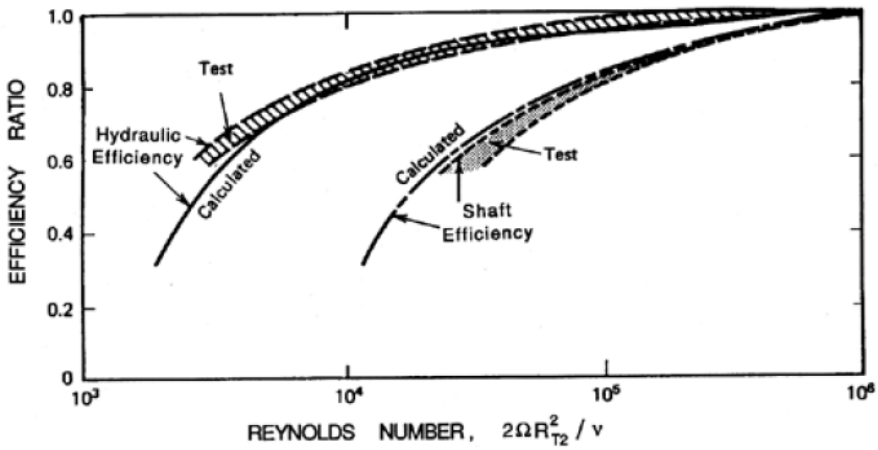

Figure 2.5 The dependence of hydraulic efficiency and shaft efficiency on Reynolds number [67].

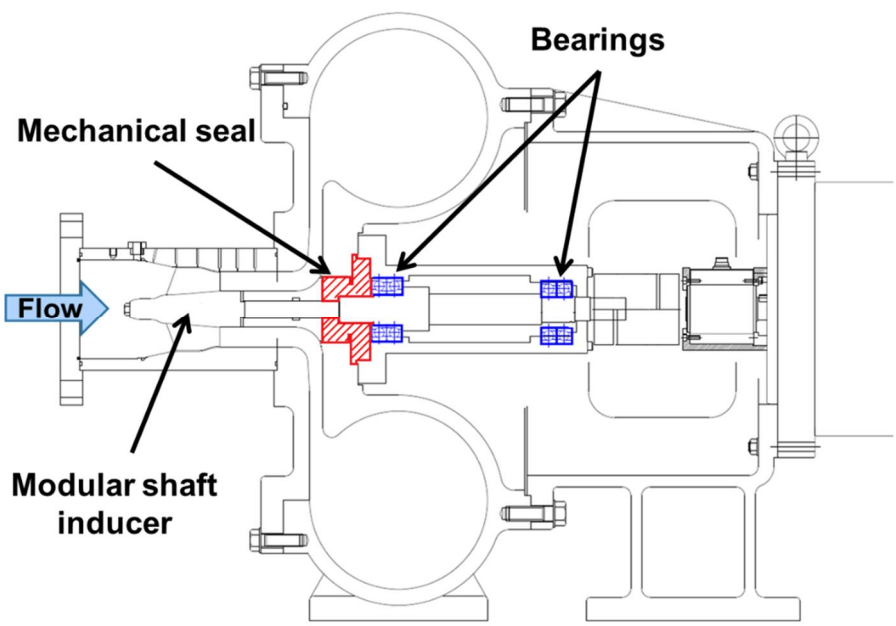

Figure 2.6 Detailed schematic of rotating parts.

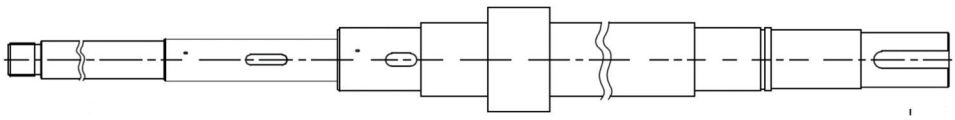

Figure 2.7 Schematic of the shaft.

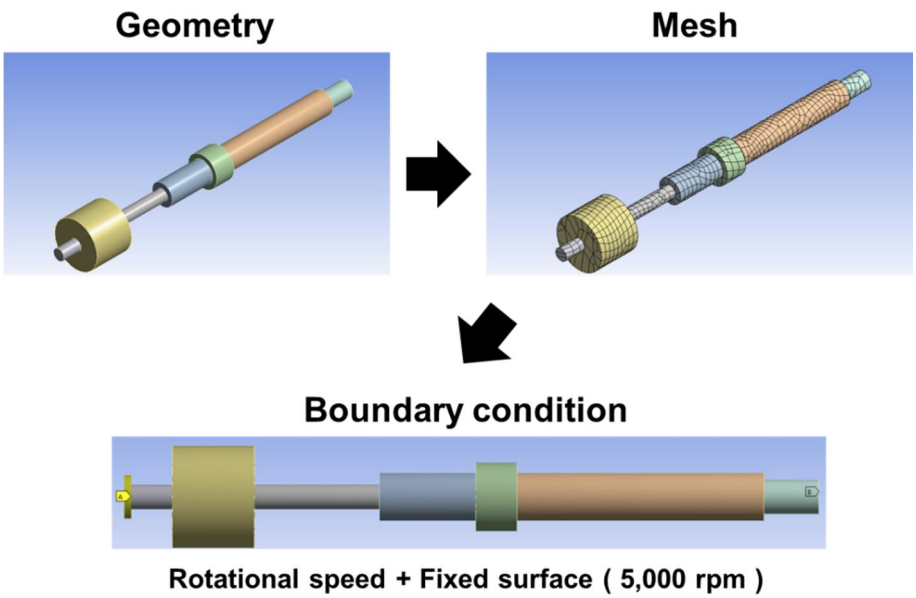

Figure 2.8 Process of rotordynamic analysis.

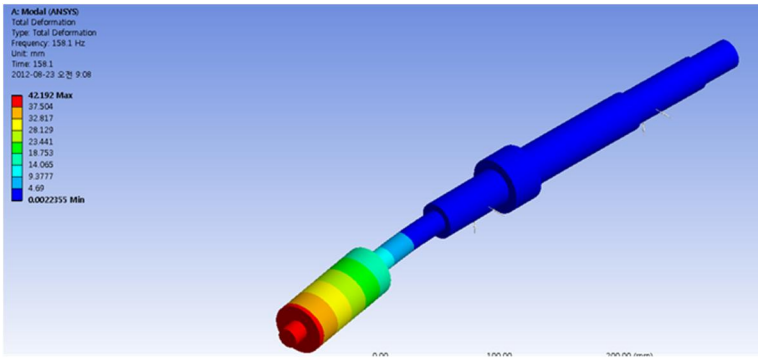

a) Mode 1: 170.74 Hz

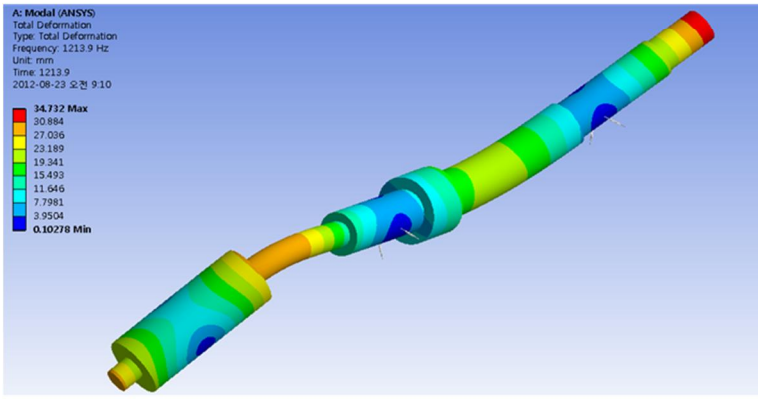

b) Mode 2: 1,237.9 Hz

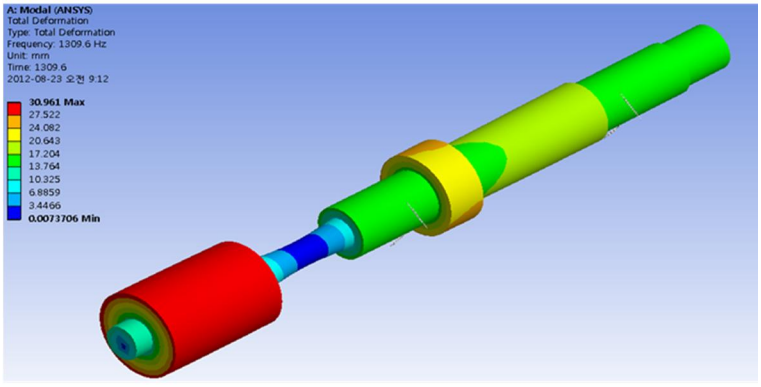

c) Mode 3: 1,392.5 Hz

Figure 2.9 Mode analysis results (1st mode: 170.74 Hz, 2nd mode: 1,237.9 Hz, 3rd mode: 1,392.5 Hz).

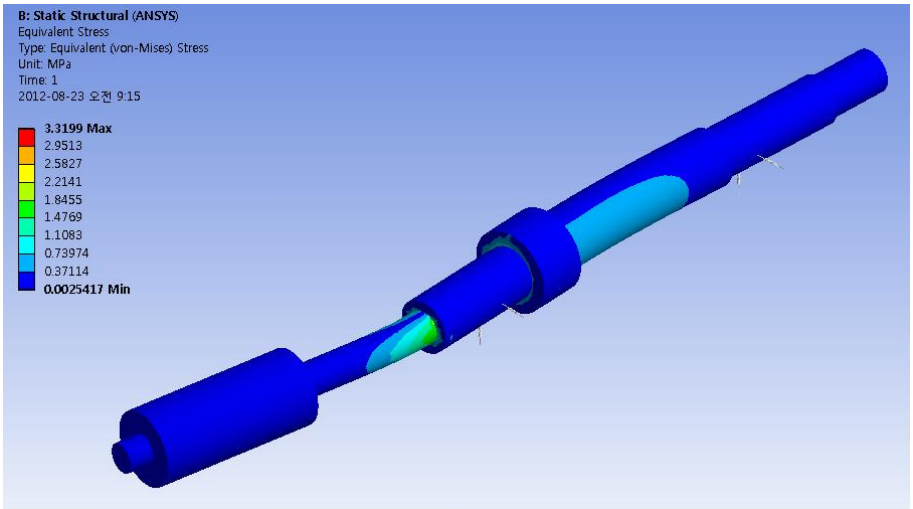

Figure 2.10 Stress analysis results (material: steel).

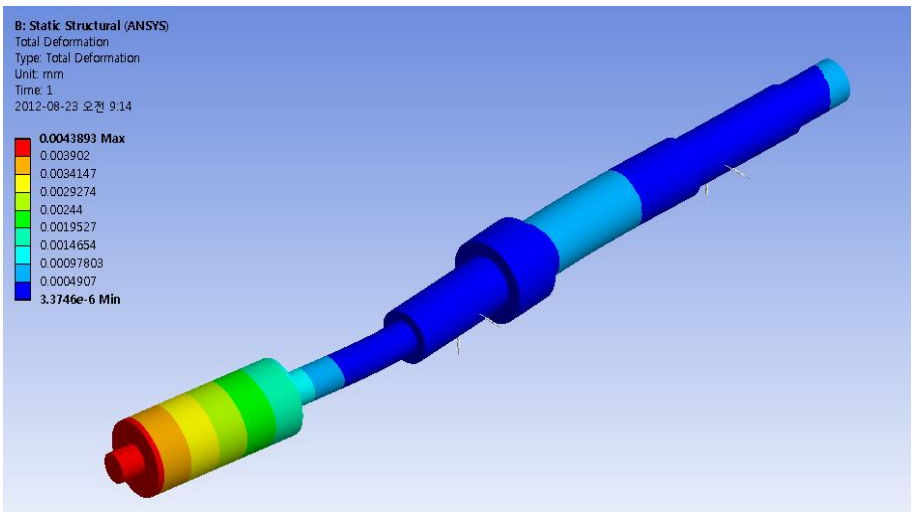

Figure 2.11 Shaft deformation analysis results (5,000 rpm).

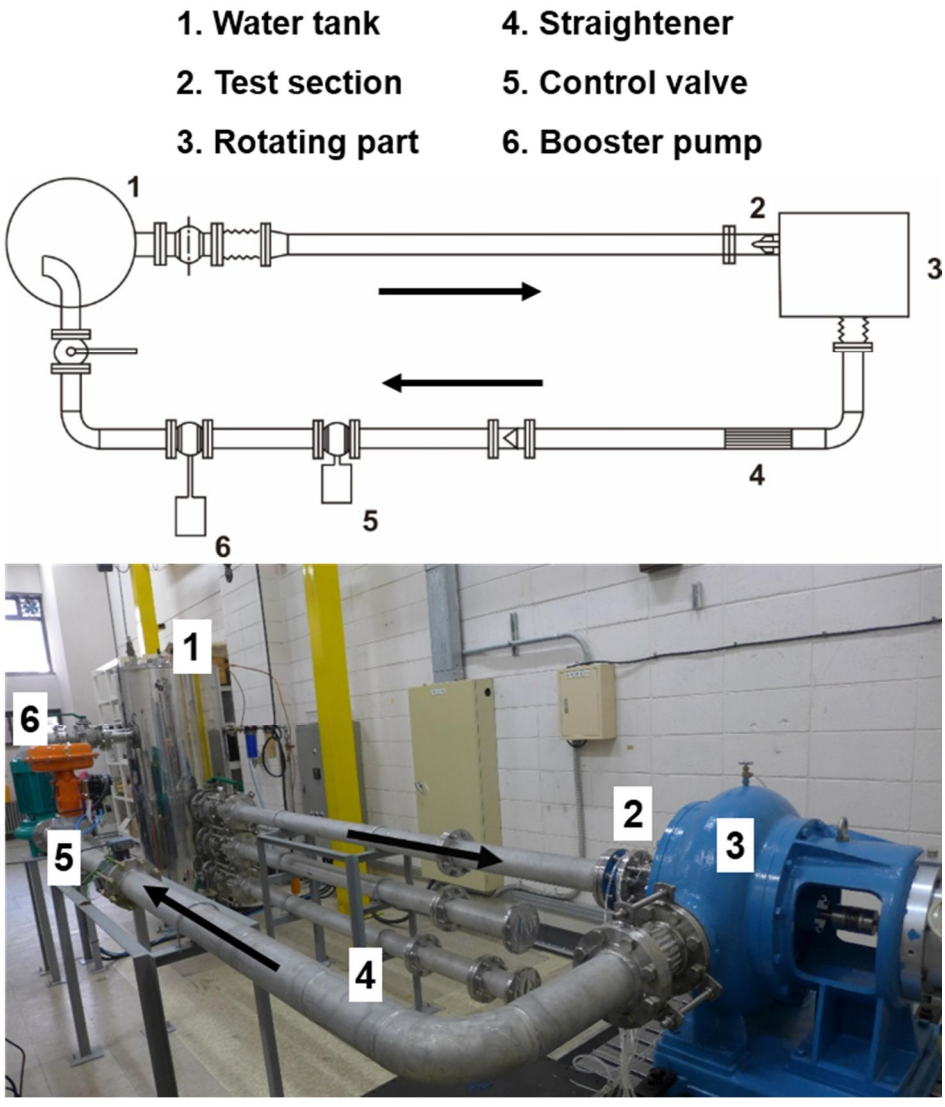

Figure 2.12 SNU turbopump inducer experimental facility.

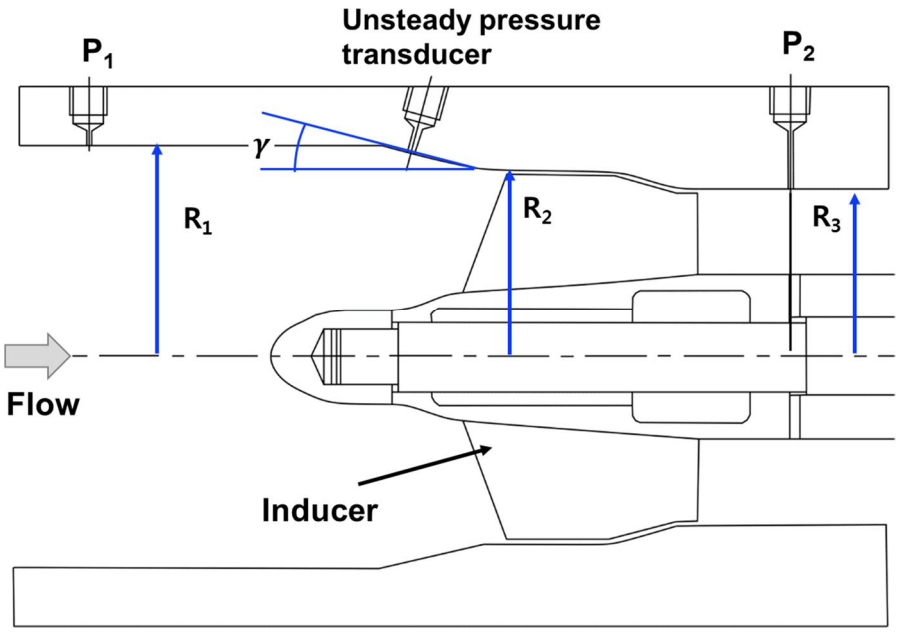

Figure 2.13 Schematic of the test inducer and the test section with the upstream enlargement step.

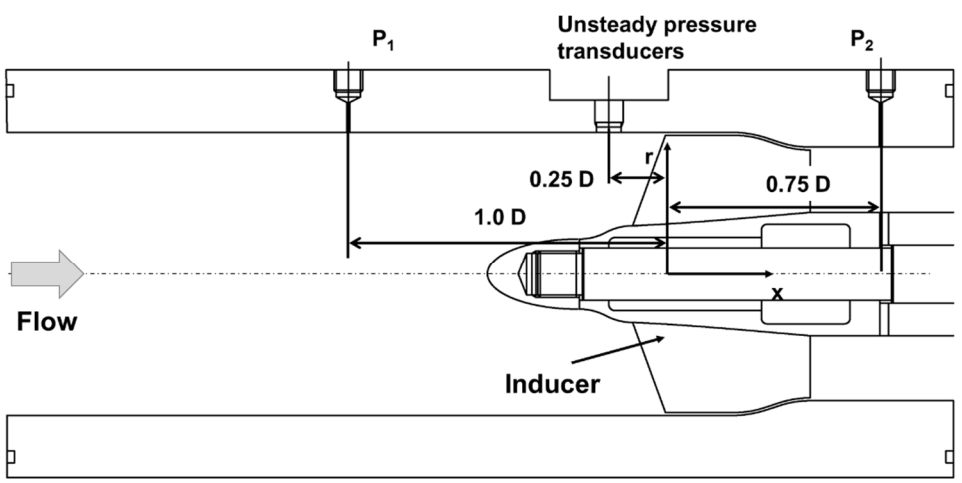

Figure 2.14 Schematic of the casing without the step.

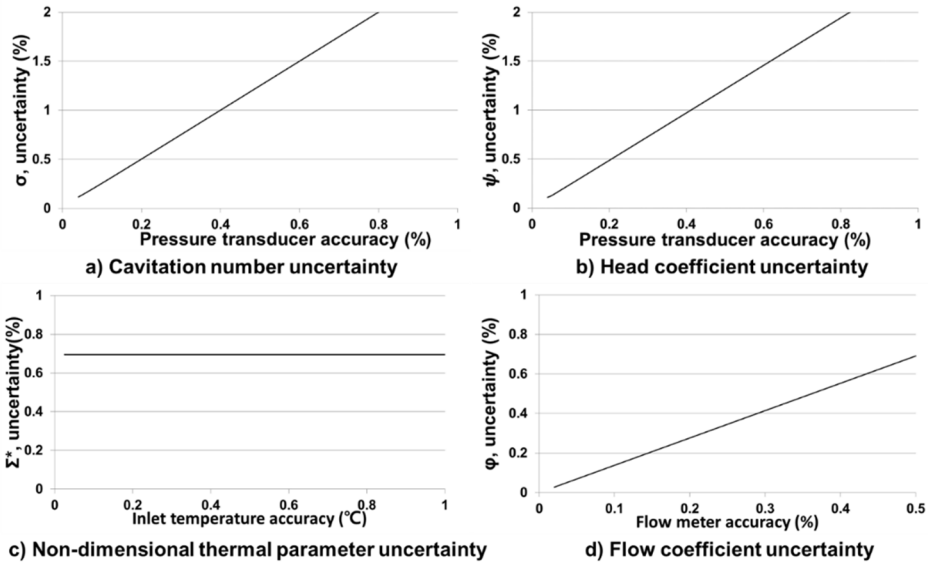

Figure. 2.15 Uncertainty analysis for non-dimensional parameters: a) cavitation number, b) head coefficient, c) non-dimensional thermal parameter, and d) flow coefficient.

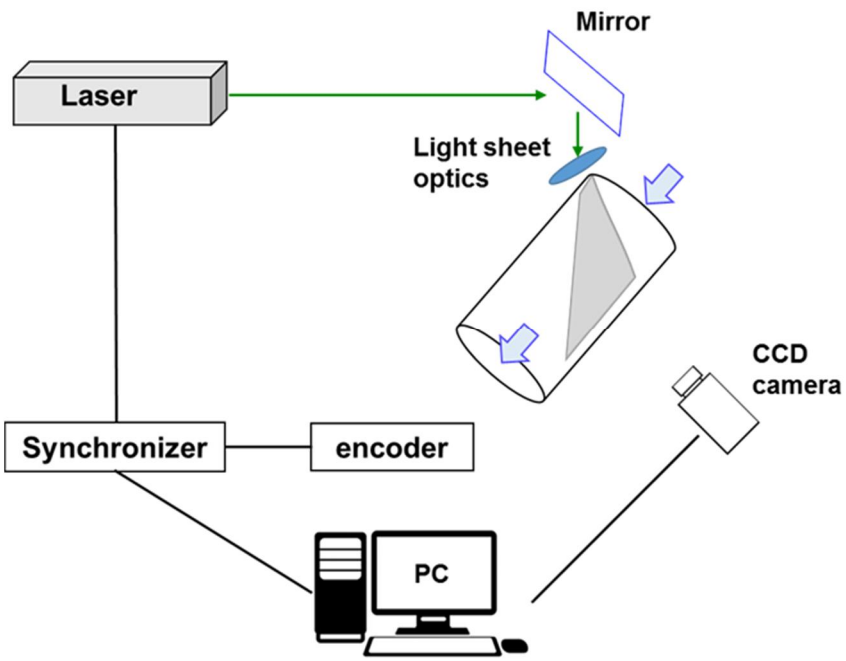

Figure 2.16 Schematic of PIV measurement system.

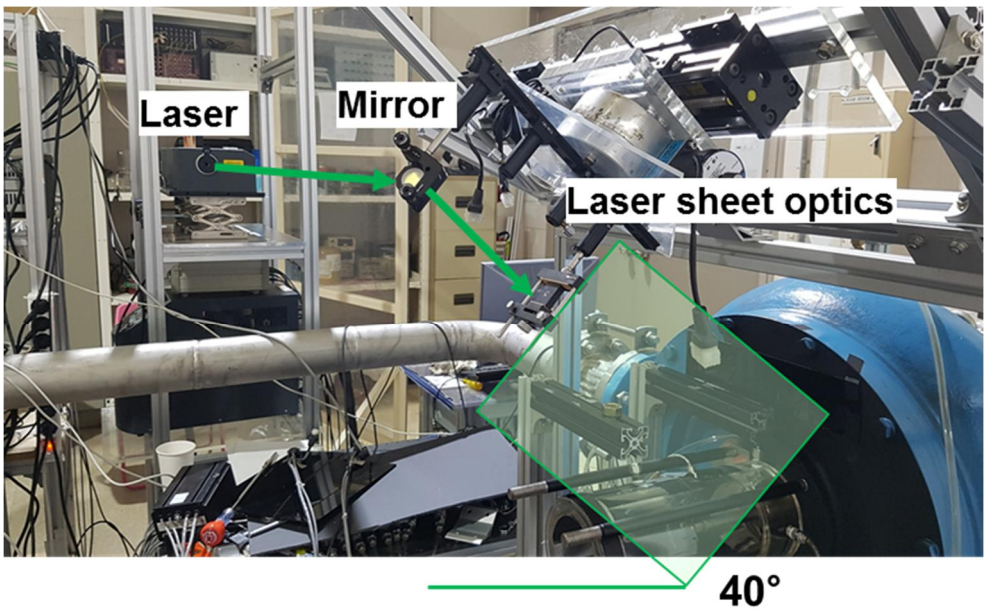

Figure 2.17 Picture of PIV measurement system.

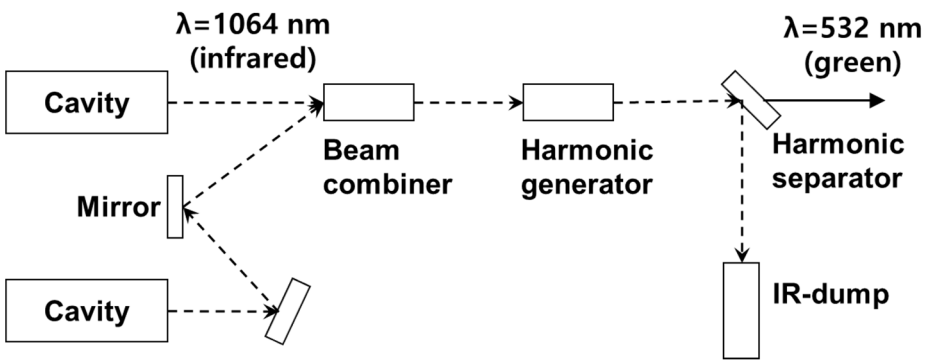

Figure 2.18 Schematic of the double-cavity PIV laser principle.

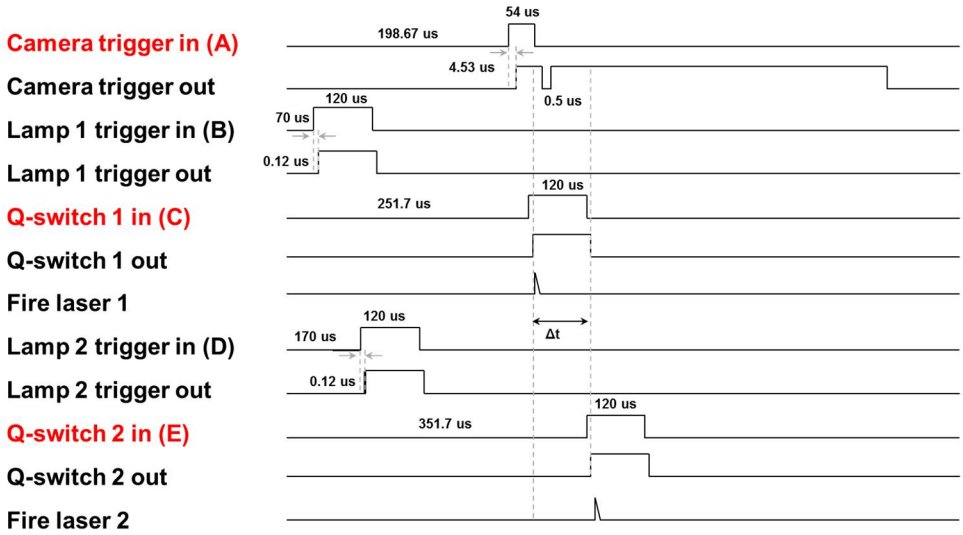

Figure 2.19 Time sequence for PIV measurement.

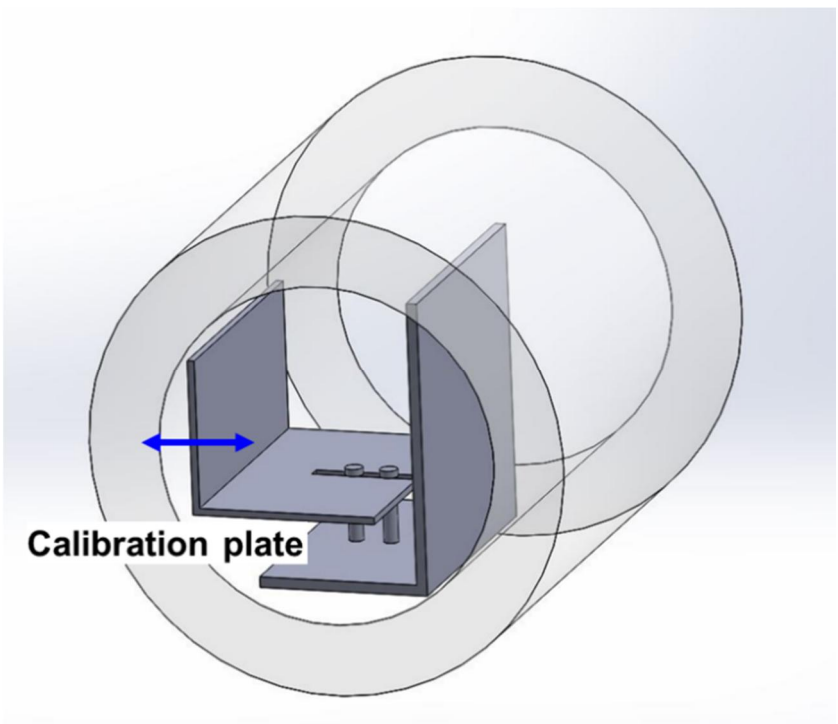

Figure 2.20 Calibration Target.

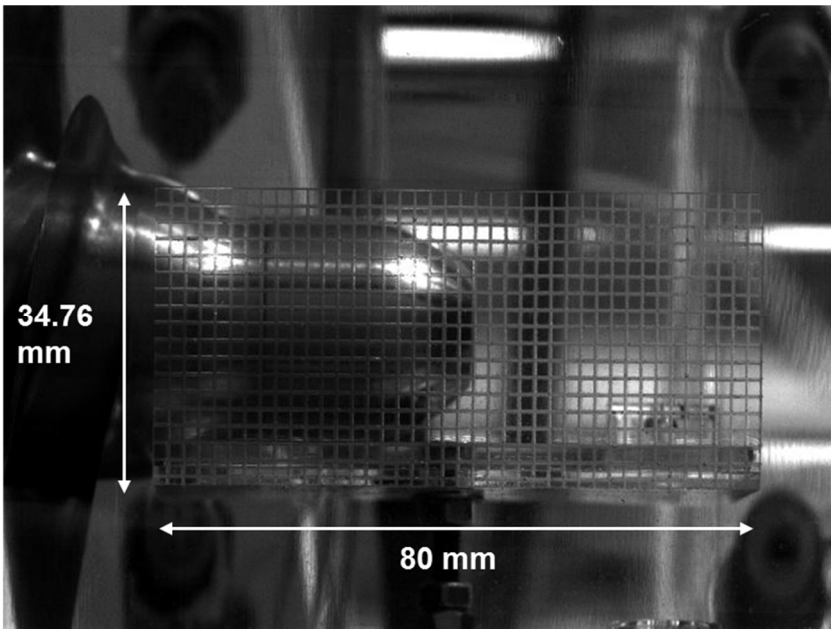

Figure 2.21 Picture of calibration plate without laser sheet.

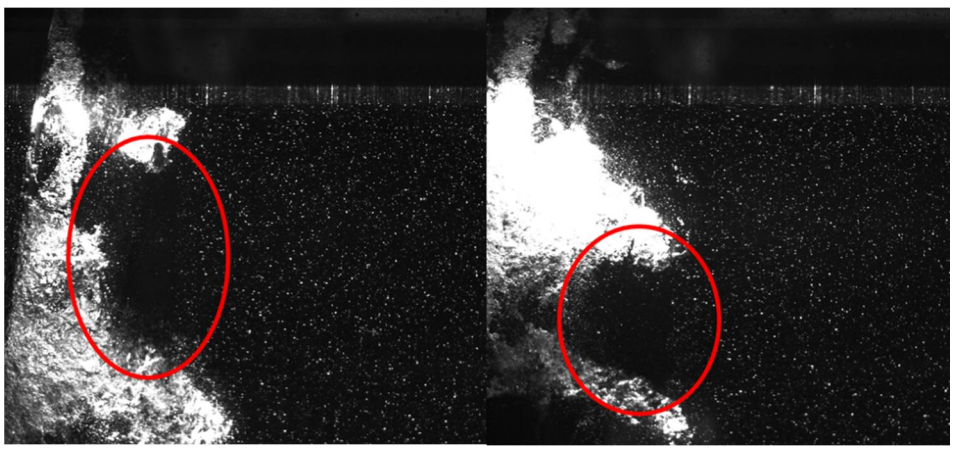

Figure 2.22 PIV image for the vertical direction laser sheet (red circle indicates the dark region due to the cavitation region blockage).

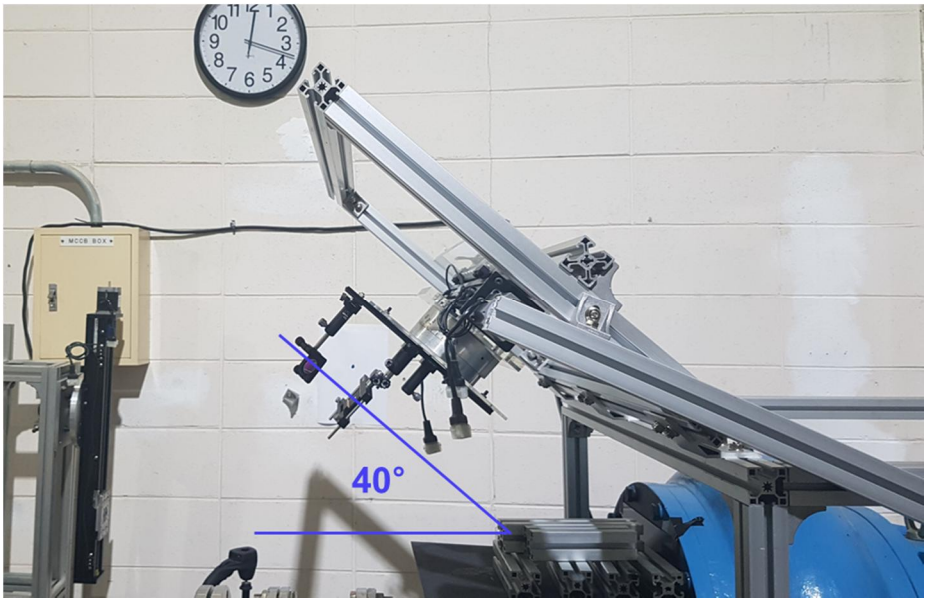

Figure 2.23 The tilted laser sheet setting.

Table 2.1 Comparison of test facilities.

Affiliation	Specification	Objectives	Main components
KARI	37 kW 6,000 rpm	Performance, instability	– Water tank – Settling chamber – Booster pump
Pisa Univ.	30 kW 4,000 rpm	Performance, instability, rotordynamics	– Water tank (airbag system) – Settling chamber – Silent throttle valve – Dynamometer
Aerospace Corp.	7.5 kW 5,000 rpm	Performance, instability, various inducer	– Vertical type – Water tank (heater) – Settling chamber – He sparging system
Osaka Univ.	30 kW 3,000 rpm	Performance, instability	– Water tank – Settling chamber – Magnetic vibrator
Caltech	15.6 kW 3,000 rpm	Instability, rotordynamics	– Water tank (heater, airbag system) – Settling chamber – Silent throttle valve – Siren valve

Table 2.2 Characteristics of the test inducer.

Parameters		Value
Diameter (r)		47 mm
Design flow coefficient (ϕ_d)		0.096
Blade number		3
Solidity at tip		2.7
Blade tip angle	Inlet (β_{1t})	9.6 deg
	Outlet (β_{2t})	15.0 deg
Non-dimensional tip clearance (c/D)		0.0106
Angle variation on line normal to hub		$\tan(\beta) = (r_t/r)\tan(\beta_t)$

Table 2.3 Design values of non-dimensional parameters.

Non-dimensional parameters	ϕ	ψ	Re	Ma
Design value	0.096	0.22	2.58×10^6	0.01

Table 2.4 Results from rotordynamic analysis.

Parameters	Value
1st mode	170.74 Hz
2nd mode	1,237.9 Hz
3rd mode	1,392.5 Hz
Maximum deformation at 5,000 rpm	3.32 MPa
Maximum stress at 5,000 rpm	4.4×10^{-3} mm

Table 2.5 Parameters of casing with step and without step.

	Casing w/ step	Casing w/o step
R_1 [mm]	54.15	48
R_2 [mm]	48	48
R_3 [mm]	43	43
γ [°]	12.3	0

Table 2.6 Measurement variables and devices.

Non-dimensional parameters	Measuring variables	Device	Location
$\phi = \frac{Q}{Ar\omega}$	Flow rate	Flow meter	Discharge line
	Rotational speed	Encoder	Motor shaft
$\sigma = \frac{P_{inlet} - P_v}{\frac{1}{2}\rho(r_1\omega)^2}$	Inlet pressure	Pressure sensor	Inlet of the inducer
	Rotational speed	Encoder	Motor-shaft
	Temperature	Thermometer	Water tank
$\psi = \frac{P_2 - P_1}{\rho(r_2\omega)^2}$	Inlet & outlet pressure	Pressure sensor	Inlet & outlet of the inducer
	Rotational speed	Encoder	Motor-shaft
	Temperature	Thermometer	Water tank
$\Sigma^* = \frac{1}{R\omega^{3/2}} \frac{(\rho_v L)^2}{\rho_l^2 \sqrt{\alpha_l} c_{p,l} T_\infty}$	Temperature	Flow meter	Water tank
	Rotational speed	Pressure sensor	Motor-shaft

Table 2.7 Specifications of measurement devices.

Device	Company	Quantity	Specifications
Flow meter	Foxboro	1	Model: IMT 25 Type: Electro-magnetic Accuracy: 0.25% Range: 0 ~ 20 L/s
Static pressure transducer	Druck	Inlet: 8 Outlet: 4	Model: PMP 5073 Accuracy : 0.04% Range - 0 ~ 2 bar (inlet) - 0 ~ 4 bar (outlet)
Torque-meter	MEAS	1	Model: UTM-300 Accuracy: 0.03% Range : 0 ~ 30 Nm, 10,000 rpm
Encoder	Baumer	1	Model: HOG 9 1024 pulse/rev Range: 0 ~ 10,000 rpm
Temperature		1	Accuracy: 0.1℃
Unsteady pressure transducer	Kulite	8	Model: HEL-375-100A Accuracy : 0.1% Range : 0~3.5 bar
Accelerometer	PCB	2	Model: 352C34 Resolution : 0.00015 g Measurement range : ±50g Frequency range : 0.5 to 9 kHz
High speed camera	Photron	1	Model: FASTCAM Mini UX 100 Max. frame rate: 200,000 fps 1,280 x 1000 pixels at 5,000 fps

Table 2.8 Specifications of data acquisition system.

Device	Company	Quantity	Usage
Oscilloscope	Yokogawa	1	Model: DL 750 Unsteady signal acquisition Resolution: 12 bit Sampling rate: 200 S/s ~ 10 MS/s Channel: 8
Amplifier	TEAC	8	Power supply to the unsteady pressure transducer and amplify the unsteady signal
NI cDAQ-9172	National Instrument	1	Chassis of NI 9205 and 9203
NI 9205	National Instrument	1	±10V signal acquisition Resolution: 16 bit Sampling rate: 350 kS/s Channel: 16
NI 9203	National Instrument	1	20 mA signal acquisition Resolution: 16 bit Sampling rate: 200 kS/s Channel: 8

Table 2.9 Specification of PIV measurement system.

Laser	Maker	New Wave Solo
	Type	ND;Yag−532 nm
	Power	120 mJ
	Diameter	4 mm
Camera	Type	PCO Sensicam, 12 bit
	Resolution	1376 x 1040 pixels
	Pixel size	6.45 μm x 6.45 μm
	Repetition rate	10 Hz
Synchronizer	Type	Quantum Composers 9518+
	Output channel	8
	Resolution	1 ns
	Accuracy	1 ns + .0001 delay
	Max. frequency	5 MHz
Seed	Type	Silver coated hollow glass spheres
	Diameter	10 μm
	Stokes number	0.003 (tracing error is less than 1 %)

Chapter 3. Test Inducer Characteristics and Rotating Cavitation Mechanism

3.1. Performance of the Test Inducer

3.1.1. Non-cavitating Suction Performance

Non-cavitating suction performance has been measured at 298 K as shown in Figure 3.1. The inducer characteristic has a negative slope for flow coefficient values above 0.0456. For flow coefficient values below 0.0456, the inducer characteristic has a zero or positive slope. At the design flow rate (ϕ_d=0.096), the measured head coefficient is 0.22, equivalent to the design value. Three repeatability tests have been performed. The head coefficient is repeatable to within 0.75 % at the design flow coefficient. At the design point, the Reynolds number is 2.58 X 10^6 based on the tip radius, rotational velocity, and fluid viscosity.

3.1.2. Cavitation Performance

Figure 3.2 shows the cavitation performance at 298 K and the design flow coefficient. Cavitation performance is the head coefficient variation according to the cavitation number, which usually is used in cavitating condition fluid-machinery. For cavitation number from 0.3 to 0.072, head coefficient remains

constant at 0.22. For cavitation number lower than 0.072, the head coefficient is decreased. Thus the critical cavitation number for this case is 0.072. Repeatability has been confirmed by 3 separate experiments showing similar values and trends.

For each measurement point, the flow coefficient has been always fixed at the specified flow coefficient. Air content in the test water has not been controlled. According to Brennen [11], cavitation inception is dependent on the air content, however, once it has initiated, the cavitation performance is independent of the air content. Thus, the air content in the test water does not significantly influence the results in the draft. Before the measurement, water has existed at low pressure for 10-15 minutes to eliminate the dissolved air.

3.1.3. Visualization of Cavitating Inducer

Figure 3.3 is the visualization of the cavitating inducer taken at the test facility using the high-speed camera. At the blade, tip leakage vortex is attached to the tip of the inducer. Backflow cavitation which propagates from the inducer to the upstream is also occurred.

Figure 3.4 shows the variation in inducer cavitation phenomenon with changes in cavitation number at the design flow rate. As cavitation number decreases, tip leakage vortex cavitation at each inducer blade and backflow vortex cavitation become larger. For cavitation number below 0.072, which is the critical cavitation number (σ_{crit}), backflow cavitation is rapidly suppressed and tip leakage vortex cavitation becomes uneven forming seemingly 2 large cavitation region and 1 small cavitation region. As cavitation

further decreases, below the critical cavitation number, backflow vortex is suppressed abruptly because the amount of pressure rise by the inducer is reduced. As cavitation number further decreases, the backflow cavitation is more suppressed, and the tip leakage vortex cavitation grows larger and blocks the flow path causing a drastic head coefficient degradation (breakdown of the cavitation performance).

3.2. Identification of Cavitation Instability

3.2.1. Identification of Cavitation Instability with Unsteady Pressure Measurement

Cavitation instabilities at the design flow rate have been identified. Fast Fourier Transform (FFT) analysis has been used to determine the frequency of the instability. The nature of the instability and the number of rotating instability cells have been determined from the cross-correlation of signals from two unsteady pressure transducers. For axial instabilities, the phase of the cross-correlation between the two unsteady pressure signals is equal to 0°. For rotating instabilities, the ratio of the phase of the cross-correlation (ϕ) and the angular distance between the pressure transducers ($\Delta\theta$) is equal to the number of the rotating cells (n_{cell}).

$$n_{cell} = \phi/\Delta\theta \tag{2.18}$$

The frequency of instability (f_r) is then determined by dividing

the detected frequency (f_d) by the rotating cell number (n_{cell}).

$$f_r = f_d / n_{cell} \tag{2.19}$$

Two kinds of cavitation instabilities have been identified in the test inducer at the design flow rate. Figure 3.5 shows the power spectral density peaks from one unsteady pressure transducers corresponding to f/Ω = 3.0 (A), 1.14 (B), and 1.0 (C) where f/Ω = 3.0 is the blade passing frequency. For σ > 0.072, the peak at f/Ω = 3.0 (A) is dominant due to blade passing and symmetric cavitation. For 0.053 < σ < 0.072, the dominant peak exists at f/Ω = 1.14 (B). Finally, for σ < 0.053, f/Ω = 1.0 is the dominant peak (C). To determine the type of instability occurring at f/Ω = 1.14 and 1.0, the power spectral density, phase, and coherence analysis have been performed using the cross-correlation of signals from two adjacent unsteady pressure transducers ($\Delta\theta$ = 45°) at σ = 0.068 and 0.046 (Fig. 3.6 and 3.8), respectively.

3.2.2. Rotating Cavitation

Peak B propagates at a super-synchronous speed (f/Ω = 1.14). The phase difference between the two transducer signals is 45° at the same frequency with a value of coherence near unity (Fig. 3.6). Therefore, peak B represents rotating cavitation instability which has been previously identified [[24], [25]]. The occurrence of cavitation instability has been confirmed through visualization. Fig. 3.7 is the high speed camera pictures when rotating cavitation occurs at σ = 0.069. When rotating cavitation occurs, cavitation region at each blade becomes uneven forming 2 large cavitation

regions and 1 small cavitation region. In Fig. 2.22, red circle indicates the small cavitation region for each rotation. During 6 revolution, the small cavitation region propagates from blade 3 to blade 1 and the back to the blade 3, which is the same frequency ($f/\Omega = 1.16$) from the unsteady pressure measurement.

3.2.3. Asymmetric Attached Cavitation and Transition

Peak C propagates at the synchronous speed ($f/\Omega = 1.0$). In Figure 3.8, there is a peak at the rotational frequency, which the magnitude is much higher than cavitation number above 0053. The phase difference of the two transducer signals is 45° with coherence near unity at this frequency. This result indicates asymmetric cavitation which is visualized in Figure 2.24 at $\sigma = 0.051$. The red circle in Fig. 3.9 where asymmetric attached cavitation occurs. For asymmetric attached cavitation, cavitation region at each blade also becomes uneven forming 2 large cavitation region and 1 small cavitation region like rotating cavitation. However, uneven cavitation region is attached to the blade and rotates with the inducer blade. Thus, peak C is asymmetric attached cavitation rotating at the synchronous speed [[12], [25]].

After rotating cavitation disappears, a transition region occurs before asymmetric attached cavitation occurs. During the transition region, uneven cavitation region becomes even as shown in Fig. 3.10, thus, the frequency is the same with the inducer rotational frequency. After the transition region, cavitation region at each blade becomes uneven again due to the occurrence of asymmetric attached cavitation.

3.2.4. Cavitation Performance and Rotating Cavitation

Figure 3.7 shows the plots of the mean head coefficient and the amplitude of the head coefficient fluctuation at the frequency of rotating cavitation versus the cavitation number at 298 K and the design flow coefficient. The critical cavitation number (σ_{crit}=0.072) corresponds to the beginning of the rise of the head coefficient fluctuation amplitude at the rotating cavitation frequency. This result indicates that the onset of rotating cavitation correlates with the start of the head coefficient degradation for the current inducer environment and the design flow coefficient.

Repeatability for the onset of rotating cavitation has been confirmed by 3 separate tests, and σ_{RC} is repeatable to within 0.7 % at the design flow coefficient.

3.3. PIV Set-up for Incidence Angle Measurement

3.3.1. Particle Image Velocimetry (PIV)

To measure the velocity field upstream of the inducer, PIV measurement technique has been adapted in this study. PIV technique is a non-intrusive laser optical velocity measurement technique used in plane (2-D or Stereo PIV) or volume velocity. From PIV measurement, instantaneous plane velocity field can be obtained. In PIV, velocity vectors are derived from sub-sections (called interrogation area) of the target area of the seeded flow by

measuring the movement of particles between two laser pulses.

$$\vec{V} = \frac{\Delta \vec{X}}{\Delta t} \tag{3.1}$$

where $\vec{V}$ is velocity, $\vec{X}$ is distance vector, and Δt is time interval between the two laser pulses.

The basic principle of PIV technique is shown in Fig. 3.12 [73]. Two laser pulses are generated for a short time (Δt) and become laser sheet as they pass the laser sheet optics. Particle seeds in the flow is illuminated by the laser sheets. The camera needs to capture each laser sheet in separate image frames. Once a sequence of two light sheet is recorded in camera, the images are separated into small interrogation area. The interrogation areas of each image are correlated with each other, pixel by pixel. When the cross-correlation generates peak, the common particle displacement is identified. From the known time interval and measured displacement, the velocity components are obtained. Velocity vector map over the whole target area is obtained through repeating the cross-correlation for each interrogation area over the two image frames.

3.3.2. PIV Set-up for Measurement of Incidence Angle

PIV equipment used in this study is described in Chapter 2. Overview of the experimental parameters for PIV measurement is summarized in Table 3.1.

Measurement location

The purpose of this study is to measure the incidence angle under rotating cavitation condition. Axial velocity and tangential velocity should be measured simultaneously. Thus, the velocity field near the leading edge of the inducer tip region is required. To measure the incidence angle, lasher sheet has been aligned at the 0.95 radius of the inducer as shown in Fig. 3.13.

Experimental conditions

If the inducer rotational speed is as high as 5,000 rpm, the time interval between the two frames are too short and the velocity vectors are hard to obtain. Thus, in PIV measurement, the rotational speed is fixed at 3,600 rpm ± 1 rpm. In this case, the tangential tip velocity is about 16 m/s and the axial velocity is about 1.54 m/s.

It is recommended that the particle moves about 4−8 pixels during the time interval depending on the size of interrogation area (less than 25 % of interrogation area). From the calculation based on the maximum velocity, the time interval is less than 30 μs. As a result of the actual experiment, the ratio of error vectors was minimized at 20 μs. Thus, the time interval is set to 20 μs during the all PIV measurements.

Considering the out of plane motion, which means that particles pass through the laser sheet, the thickness of the laser sheet should be at least four times the distance that the particles move in the sheet thickness direction. In the present study, the laser sheet thickness needs to be larger than 700 μm. To narrow the laser sheet thickness, the 1.2 mm slot has been installed before the laser sheet enters to the transparent acryl casing.

Raw image

When laser sheet aligned precisely, the calibration plate is illuminated through laser as shown in Fig. 3.14. To accurately align the laser sheet, the laser should be passed down from the top of the calibration target. The degree of laser alignment is known from the degree of illumination of calibration plate. To align the laser sheet, a mirror and a laser sheet optic is aligned on the rotating and linear traverse. Figure 3.14 is applied to the calibration data of the PIV data processing.

Figure 3.15 shows the raw image of the PIV measurement in case of the tilted laser sheet. Laser power has been adjusted properly, not too strong (scattering problem of particles and cavitation region) or weak (difficulties in distinguish particles). Particle density is also important to capture the velocity vector accurately. It is recommended that at least 5 particles exist in the 32 x 32 pixels interrogation area. In this study, there are more than 20 particles (average value is about 30) in the 32 x 32 pixels interrogation area.

3.3.3. PIV Image Processing

In this study, PIV measurement performed in the rotating inducer. Thus, the velocity gradient is high near the rotating inducer. Conventional PIV data processing methods is not suitable to high velocity gradient flow. To solve this problem, the recently developed PIV post processing algorithm is used in this study, called ‘adaptive PIV’. The fundamental principle of Adaptive PIV

[74] is an iterative procedure: From the offset of the first interrogation area, vector is validated and is used as a new estimate. This iteration procedure gives more accurate vector information. The comparison of conventional PIV algorithm and Adaptive PIV algorithm is shown in Fig. 3.16. The conventional PIV algorithm cannot capture the drop out motion from the interrogation area. On the other hand, using Adaptive PIV method, dropout plane particles can be captured. Adaptive correlation also automatically calculates optimized interrogation area size and shape based on the flow gradients and gives 30 % less error than the conventional PIV algorithm [[75], [76]]. Thus, it gives more accurate results in high velocity gradient flow.

The evaluation of the velocity vector fields from the PIV measurement is performed with the commercial PIV software DynamicStudio 14.0 from Dantec. The interrogation areas of 32x32 pixels large, with 50 % overlap were used, resulting in 5,440 vectors for the 1,360 x ,1040 pixels. The ratio of error vector is less than 2.5 %. The final results are smoothed once with a 3x3 Gaussian kernel. Peak validation has been performed with the minimum accepted 0.25 peak height, 1.15 peak height ratio, and 4.0 S/N ratio. Uncertainty has been also automatically calculated in DynamicStudio with 3.7 % (velocity) and ± 1.21° (incidence angle). The uncertainty values are relatively higher due to the out of plane motion of the particle with rotating conditions.

Small cavitation bubbles also act as tracer particles. Velocity vectors inside the cavitation region are also calculated because patterns of the cavitation region movement is captured during the PIV data process.

3.4. The Cause of Rotating Cavitation

3.4.1. Identification of Rotating Cavitation

The occurrence of rotating cavitation has been identified with adjacent two unsteady pressure measurements with the casing without the step. Figure 3.17 represents the power spectrum density for the casing without the ramp at ϕ/ϕ_d=1.03. Rotating cavitation occurs at cavitation number 0.079. Frequency ranges from 1.17 Ω to 1.14 Ω as cavitation number decreases.

3.4.2. High Speed Camera Image of Cavitating Inducer

Figure 3.18 represents the cavitating inducer for the casing without the ramp used for PIV measurement. Backflow vortex cavitation is smaller in case of the casing without the step than the casing with the step (Fig. 2.4). As cavitation number decreases, tip leakage vortex cavitation region grows and backflow vortex cavitation is suppressed. Tip leakage vortex cavitation growth is related to the onset of rotating cavitation.

3.4.3. Incidence Angle Variation under Non-Rotating Cavitation Condition

The flow near the inducer is 3-D, thus, the velocity from PIV measurement is different with the real velocity. Especially, the velocity discrepancy near the edge of PIV plane is the largest. The

maximum discrepancy between the measured velocity and transformed velocity using the trigonometrical function is 3.7 %. The transformed velocity is used to calculate incidence angle contour. To minimize the velocity discrepancy effect, incidence angle is measured at the center of PIV images.

PIV measurement have been performed at the cavitation number immediately before rotating cavitation occurs and cavitation number when rotating cavitation occurs. σ_{RC} =0.079, thus, PIV measurement without rotating cavitation has been performed at σ=0.080. The incidence angle is defined as follows.

$$\alpha = \beta_1 - \tan^{-1}\frac{V_a}{V_t} \tag{3.4}$$

Measurement location of the incidence angle is 4 degree upstream of the inducer leading edge at 95 % radius [41]. Figure 3.19 represents the schematic of the detailed incidence angle measurement location.

Figure 3.20 and 3.21 show velocity vectors with raw image of PIV and incidence angle contour with velocity vectors from the ensemble average of the PIV images under no-rotating cavitation condition, respectively. Several sets of raw image result under no-rotating cavitation are shown in Appendix D. Under no rotating cavitation condition, 200 PIV images are used for the ensemble average. White (Fig. 3.20) and black (Fig. 3.21) bar represents the blade and the blade moves from top to bottom. The red circle indicates the measurement position of the incidence angle.

As shown in Fig. 3.20 and 3.21, the tip leakage vortex cavitation does not grow enough to affect the following blade. Thus, the incidence angle at the leading edge of the inducer is 6.06

ranging from 4.13° to 9.20°.

Based on the incidence angle contour, incidence angles far upstream of the inducer is about 4° which is the similar value from the inducer design specifications and flow coefficient (4.01°). As flow approaches to the inducer, incidence angle is slightly increased. The backflow and viscosity reduces the relative tangential velocity, thus the incidence angle near the blade is higher than the bulk flow.

3.4.4. Incidence Angle Variation under Rotating Cavitation Condition

PIV measurement also has been performed at σ=0.070, where rotating cavitation exists. Unsteady pressures also have been measured simultaneously to identify the occurrence of rotating cavitation when PIV particles are injected. Figure 3.22 shows the power spectrum density, phase difference, and coherence of unsteady pressure fluctuations with PIV particles. The occurrence of rotating cavitation with f/Ω = 1.17 has been confirmed.

Under rotating cavitation condition, large cavitation region and small cavitation region are formed. Cavitation region at each blade changes the flow field. Thus, for the large cavitation region, PIV images of similar tip leakage vortex cavitation are selected for the ensemble average. Following et al. [77], at least 24 pictures of PIV are needed for ensemble average. Under rotating cavitation condition, for large cavitation effect, 24 pictures have been selected and for small cavitation effect, 50 pictures have been selected in this study. Several sets of raw image result under rotating cavitation are shown in Appendix D.

Figure 3.23 and 3.24 show velocity vectors with raw image of PIV and incidence angle contour with velocity vectors from the ensemble average of the PIV images under rotating cavitation with the large tip leakage vortex cavitation effects. As shown in Fig. 3.22, the large tip leakage vortex cavitation regions from the backward blade to the following blade are observed. Due to the large cavitation region, velocity near the following blade leading edge is increased and the incidence angle of the following blade becomes negative value at −4.37° (−1.93° to −8.25°).

From the velocity vectors, axial and absolute tangential velocity increase near the leading edge of the following blade as shown in Fig. 3.22. Thus, the incidence angle near the following blade reduces to the negative values. Negative incidence angle suppresses the tip leakage vortex cavitation of the blade. Therefore, the large tip leakage vortex cavitation suppresses the next blade cavitation region.

Figure 3.25 and 3.26 also show velocity vectors with raw image of PIV and incidence angle contour with velocity vectors from the ensemble average of the PIV images under rotating cavitation with the small tip leakage vortex cavitation effects. As shown in Fig. 3.25, the cavitation region of the backward blade is not observed. The trend and value of velocity vectors of the small cavitation region are similar to the velocity vectors under no rotating cavitation condition. Consequently, the incidence angle contour values are also similar to the no rotating cavitation condition. With the small cavitation region, the incidence angle value recovers to the positive value 6.69° (4.32° to −9.44°). Incidence angles near the leading edge have positive values. Positive incidence angle promotes the tip leakage vortex cavitation of the blade. Thus, the

small tip leakage vortex cavitation promotes the next blade cavitation region.

3.4.5. Effect of the Tip Leakage Vortex Cavitation on the Flow Field

Velocity divergence (G) and 2nd invariant Q of velocity divergence (Q) have been employed to understand the flow field change under rotating cavitation based on the ensemble average of PIV measurement results. The definition of velocity divergence and 2nd invariant Q of velocity divergence are as follows;

$$G = \nabla \cdot u \tag{3.5}$$

$$Q = \frac{\partial U}{\partial x}\frac{\partial V}{\partial y} - \frac{\partial V}{\partial x}\frac{\partial U}{\partial y} \tag{3.6}$$

For positive peak of 2nd invariant Q, the vorticity magnitude prevails over the strain-rate magnitude, thus, it indicates the vortex core as identified from Hunt et al. [72].

Figure 3.27 and 3.28 represent the velocity divergence and 2nd invariant Q under rotating cavitation with large (a) and small (b) cavitation region. In case of the large cavitation, negative velocity divergence region is formed near the leading edge of the following blade acting as sink. Thus, the flow is sucked to the negative divergence region, leading to increase in the axial and absolute tangential velocity near the leading edge. This is also confirmed by the CFD results from Tani et al. [41]. This sink flow is formed by the vortex flow at to the closure region of tip leakage vortex

cavitation. As shown in Fig. 3.28 (a), positive peak of Q is located at the closure region of the tip leakage vortex cavitation, which means that the vortex core is located at the closure region of the cavitation region. Figure 3.29 represents vorticity near the inducer and the negative vorticity is formed near the vortex core. Consequently, the negative direction vortex core is formed at the closure region of the tip leakage vortex cavitation, and leads to decrease in the incidence angle of the following blade.

On the other hand, for small cavitation case, positive velocity divergence near the inducer leading edge. Positive peak of Q is also not found in the Q contour. Figure 3.30 also shows the velocity divergence and 2nd invariant Q under no rotating cavitation condition. The velocity divergence and 2nd invariant Q contours are similar to the small cavitation case under rotating cavitation. Thus, vortex core is not formed near the leading edge of the following blade in case of the small cavitation under rotating cavitation or no rotating cavitation case.

Another method to identify the vortex at the closure region of the tip leakage vortex cavitation is subtraction of velocity vectors for the rotating cavitation condition (σ=0.070) from the non-cavitating velocity vectors (σ=1.12) at the same phase. The velocity vector subtraction is not an accurate method, but it can approximately give clues how tip leakage vortex cavitation affects the flow field. Figure 3.31 shows the result of the velocity vector subtraction (velocity vectors of rotating cavitation condition - velocity vectors of non-cavitating condition). There are vortex core near the closure region of the tip leakage vortex cavitation region (red circular arrows) and penetration flow downward (red arrows heading to downward). These two vectors influences the

flow field near the inducer leading edge leading to increase in the axial velocity and reduce the relative tangential velocity. To investigate flow field near and inside the tip leakage vortex cavitation, tip leakage vortex cavitation at different blade locations is observed with the velocity field subtraction as shown in Fig. 3.32. Figure 3.32 shows the velocity vector subtraction images at different position of blade and tip leakage vortex cavitation region. White bare also represents the blade. Vortex region cores are also formed at the closure region of the tip leakage vortex cavitation as shown in Fig. 3.32.

Inside the cavitation region, PIV algorithm can capture the cavitation region movement, thus, it gives the velocity vectors. From the velocity vectors, tip leakage vortex cavitation structure can be observed, especially from Fig. 3.31 and 3.32, because the author subtracted the non-cavitating condition flow from the cavitating flow. Near the inducer blade, velocity vectors from the blade pressure side to the suction side are observed due to the tip leakage flow. The combined effects of the tip leakage flow and the vortex core near the closure region introduce the penetration flow (direction from top to bottom) as shown in Fig. 3.31 and 3.32.

3.5. Pulsation Mechanism of Rotating Cavitation

3.5.1. Pulsation Mechanism of Rotating Cavitation

Based on the cause of rotating cavitation, the pulsation

mechanism of rotating cavitation has been explained. Rotating cavitation is occurred when the tip leakage vortex cavitation reduces the next blade incidence angle to negative values as the cavitation region grows. When rotating cavitation occurs, uneven cavitation region is formed as shown in Fig. 3.33. In Fig. 3.33, white lines represent the blade 3, 2, and 1, respectively. When the cavitation region at blade 2 is large, (Fig. 3.33 (a)), tip leakage vortex cavitation region at blade 3 is suppressed and becomes small due to the negative incidence angle. When the cavitation region at blade 2 is small (Fig. 3.33 (b)), tip leakage vortex cavitation at blade 3 is promoted and becomes large. Following these mechanism, the cavitation region of each blade periodically grows and inhibits. This pulsation occurs sequentially for each blade, thus, the small cavitation region seems to move from blade 3 to blade 1 and return to blade 3, propagating forward as shown in Fig. 3.7. Figure 3.34 is the schematic of the pulsation mechanism of each cavitation region under rotating cavitation. This mechanism was suggested by the 3-D RANS simulation of cavitating inducer from Kang et al. [39] and Tani et al. [41] and is confirmed by experiments from this study.

Visualization of rotating cavitation (Fig. 3.7) also confirms the suggested pulsation mechanism above. The cavitation region at blade 3 is the smallest when the cavitation region at blade 2 is large for rotation 1. The small cavitation region at blade 3 seems to move to blade 2 and blade 1 and return to blade 3 during 6 revolutions. The frequency from the visualization is the same as the frequency from the unsteady pressure measurement.

The cavitation region of each blade pulsates attached to the blade, thus, the measured frequency of the rotating cavitation is sum of rotational frequency and the cavitation region pulsation

frequency, thus the measured frequency is super-synchronous as shown in Fig. 3.17. Based on the mechanism explained above and visualization of rotating cavitation, the frequency of the cavitation region pulsation under rotating cavitation is f/Ω = 0.17 when σ=0.070. This pulsation frequency decreases from f/Ω = 0.17-0.14 as cavitation number decreases as shown in Fig. 3.17.

From this experimental study, rotating cavitation onset is governed by the 3-D tip leakage vortex cavitation. Thus, an investigation of 3-D tip leakage vortex cavitation is further required.

3.5.2. Cavitation Region Length Change under Rotating Cavitation Condition

Tip leakage vortex cavitation region length has been measured with and without rotating cavitation through high-speed camera visualization. It is ambiguous to define the end of the tip leakage vortex cavitation length. In this study, the end of the tip leakage vortex cavitation is defined to where the tip leakage vortex cavitation is vanished. The length of the cavitation region has been determined by measuring how many degrees the cavitation region rotates from beginning to the end. There are errors due to the cavitation region fluctuation, ambiguous closure region definition. Even though there are errors, tip leakage vortex cavitation length fluctuation has been measured.

Figure 3.35 and 3.36 show that the tip leakage vortex cavitation length fluctuation with and without rotating cavitation, respectively.

The tip leakage vortex cavitation length is normalized by the blade spacing following Watanabe et al. [33]. X axis is number of revolution and y axis is the normalized tip leakage vortex cavitation length. The length of the cavitation region at each blade is shown in Fig. 3.35 and 3.36. Under rotating cavitation, the fluctuation is higher than the case without rotating cavitation. The peak to peak frequency is 1/6 rotation (f/Ω = 0.17). Thus, the fluctuation of the cavitation region length corresponds to the measured rotating cavitation frequency (f/Ω = 1.17).

The non-dimensional average lengths of the tip leakage vortex cavitation with and without rotating cavitation are 0.444 and 0.433. Thus, the critical length when rotating cavitation initiates is about 0.44. Following Watanabe et al. [33]' s analysis, the critical length is 0.65. The result from Yoshida et al. [45] also confirmed the analysis result. Franc et al. [6] reported that the rotating cavitation occurs when the blade cavitation region occupies 10 % of the blade spacing. In this study, rotating cavitation occurs when the tip leakage vortex cavitation occupies 44 % of the blade spacing. For the onset of rotating cavitation, the tip leakage vortex cavitation length is significant. However, the critical length is different from the inducer geometry. Therefore, it is difficult to estimate the onset of rotating cavitation by the length of the tip leakage vortex cavitation.

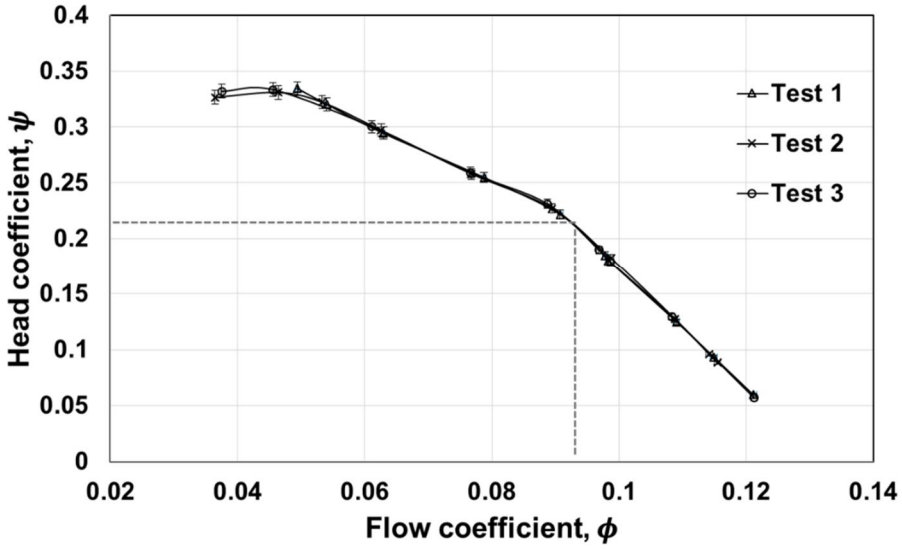

Figure 3.1 Non-cavitating suction performance curves (T_∞=298 K, 5,000 rpm).

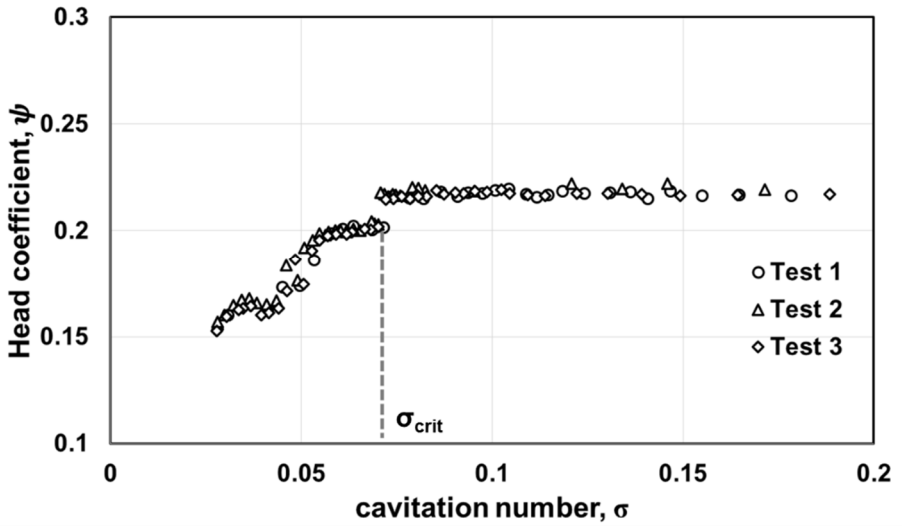

Figure 3.2 Cavitation performance (ϕ/ϕ_d=1.0, T_∞=298 K, 5,000 rpm).

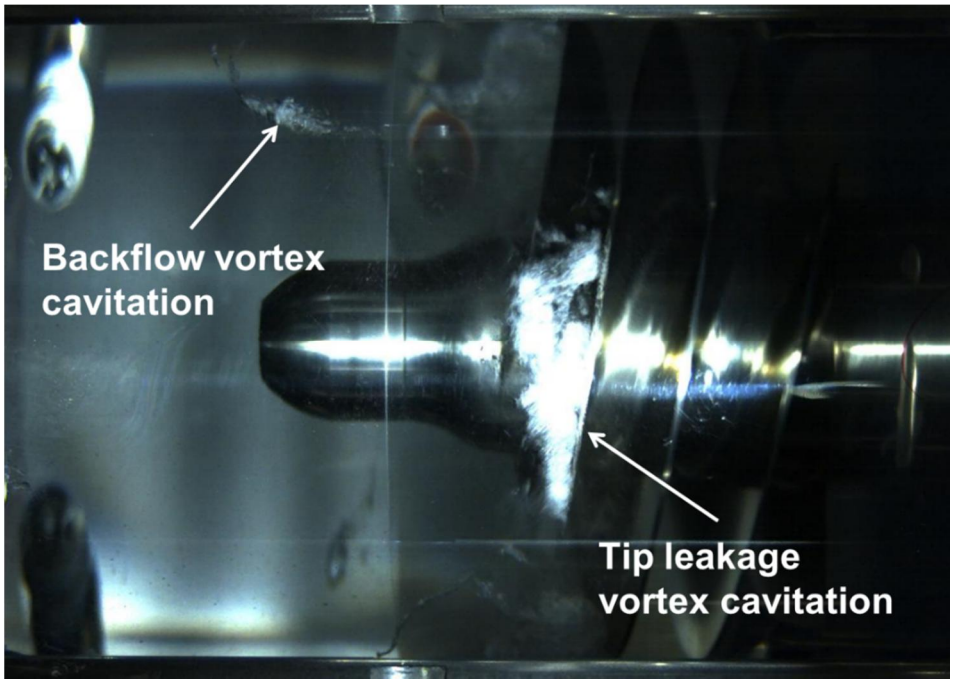

Figure 3.3 Visualization of cavitating inducer.

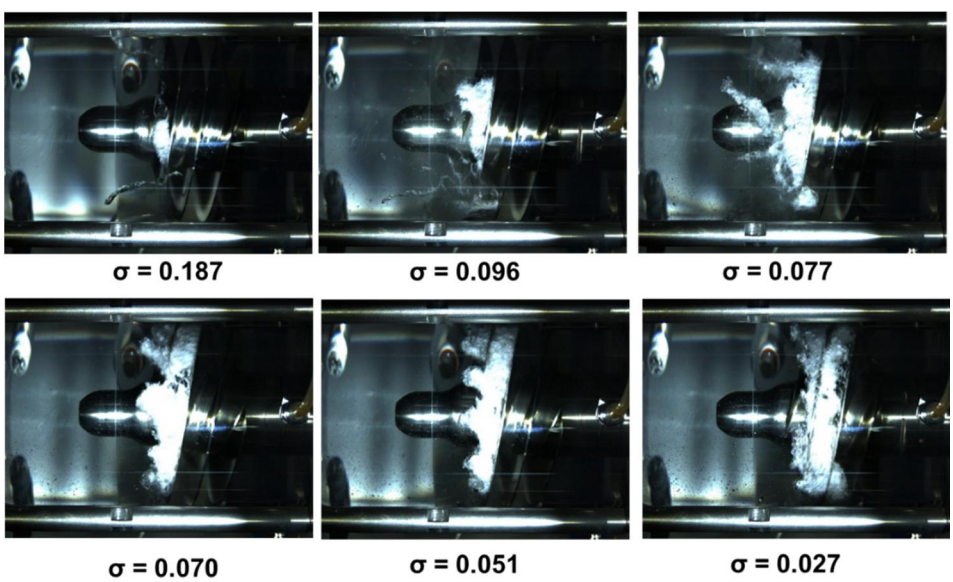

Figure 3.4 Variation in inducer cavitation according to cavitation number (ϕ/ϕ_d=1.0, T_∞=298 K, 5,000 rpm).

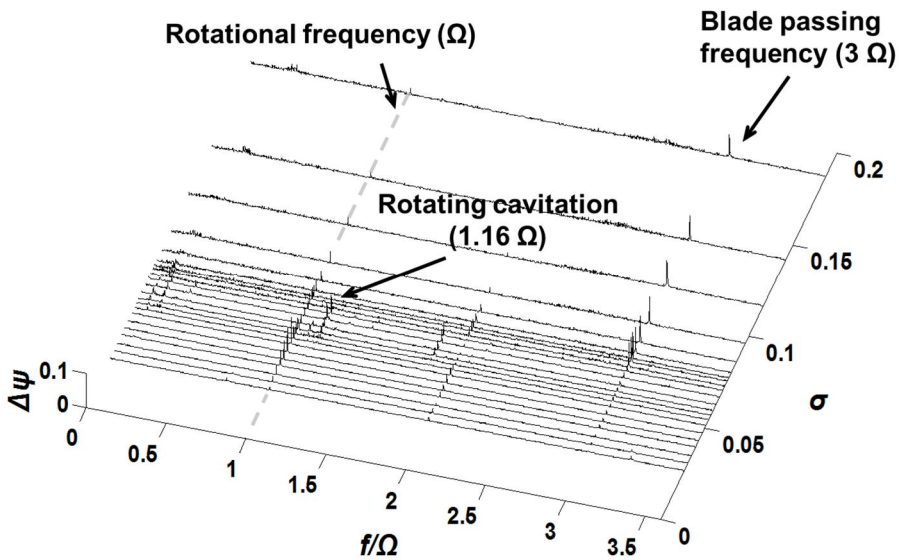

Figure 3.5 The power spectral density of inducer inlet pressure fluctuations for for casing with a ramp (ϕ/ϕ_d=1.0, T_∞=298 K, 5,000 rpm).

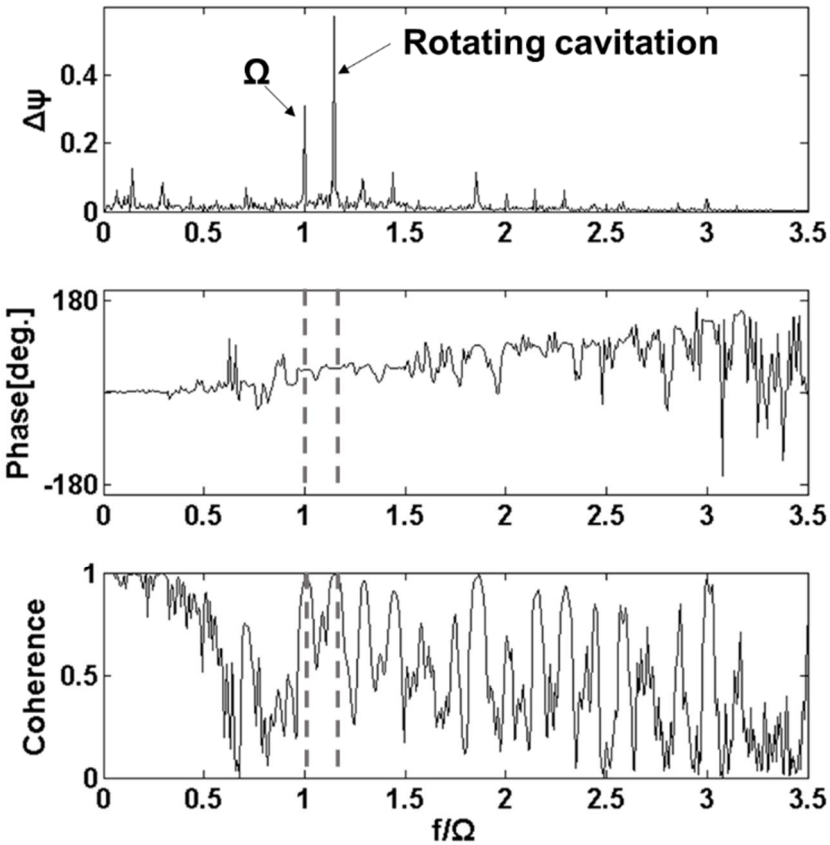

Figure 3.6 The power spectral density, phase difference, and coherence of unsteady pressure fluctuations from two pressure transducers with 45° angular separation in upstream of the inducer under rotating cavitation condition (σ=0.068, ϕ/ϕ_d=1.0, T_∞=298 K).

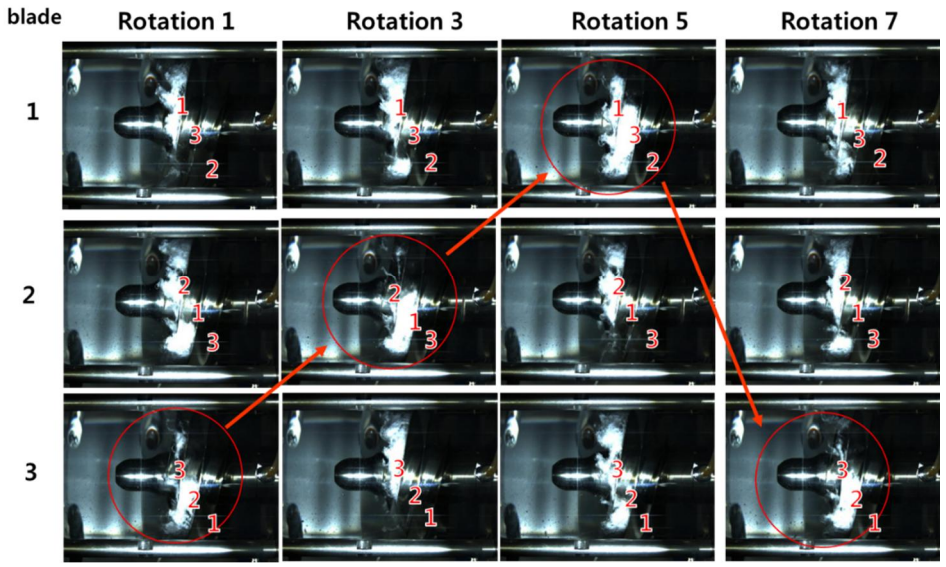

Figure 3.7 High speed images of rotating cavitation propagation. Red circles indicate the smallest cavitation region, and it propagates faster than the inducer rotational speed (σ =0.069, ϕ/ϕ_d=1.0, T_∞=298 K).

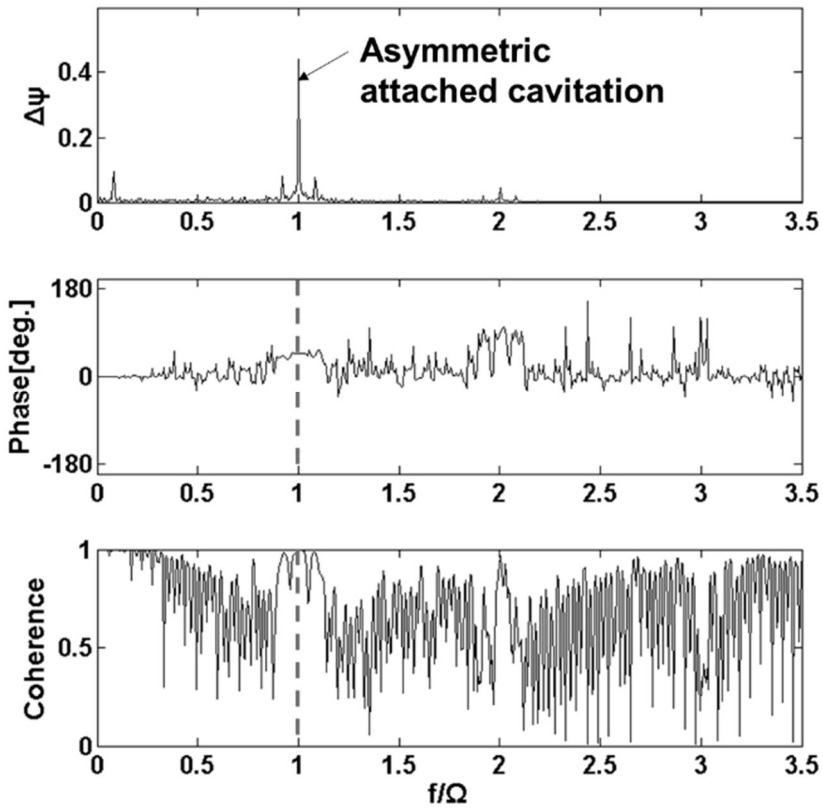

Figure 3.8 The power spectral density, phase difference, and coherence of unsteady pressure fluctuations from two pressure transducers with 45° angular separation in upstream of the inducer under asymmetric attached cavitation condition (σ=0.047, ϕ/ϕ_d=1.0, T_∞=298 K).

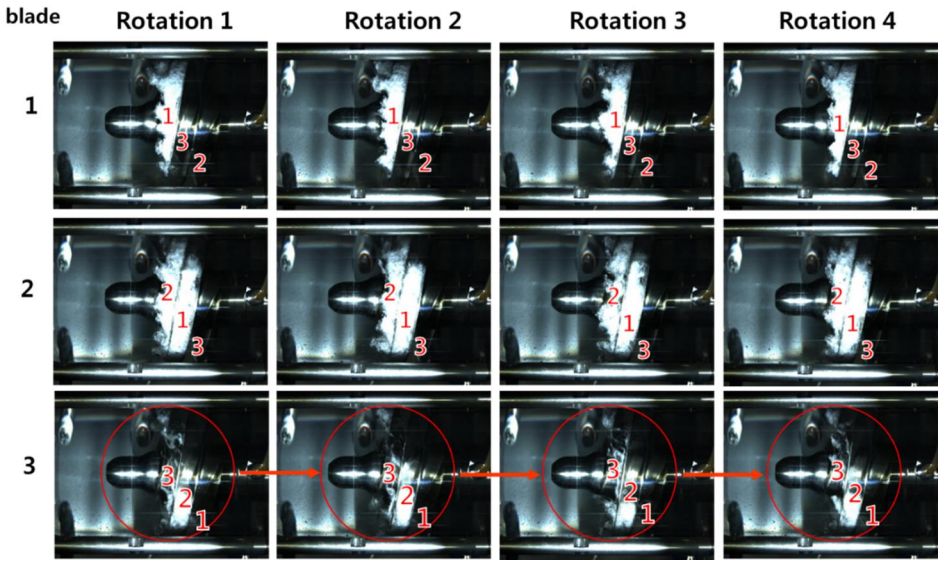

Figure 3.9 High speed images of asymmetric attached cavitation propagation. Red circles indicate the smallest cavitation region, and it is attached to blade rotating with the inducer rotational speed (σ =0.051, ϕ/ϕ_d=1.0, T_∞=298 K).

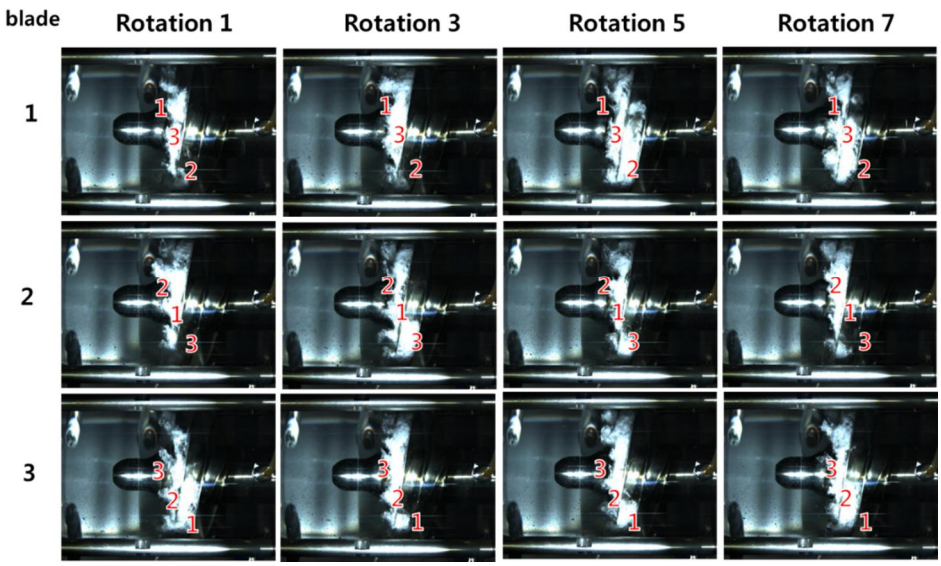

Figure 3.10 High speed images of transition region between rotating cavitation and asymmetric attached cavitation (σ =0.054, ϕ/ϕ_d=1.0, T_∞=298 K).

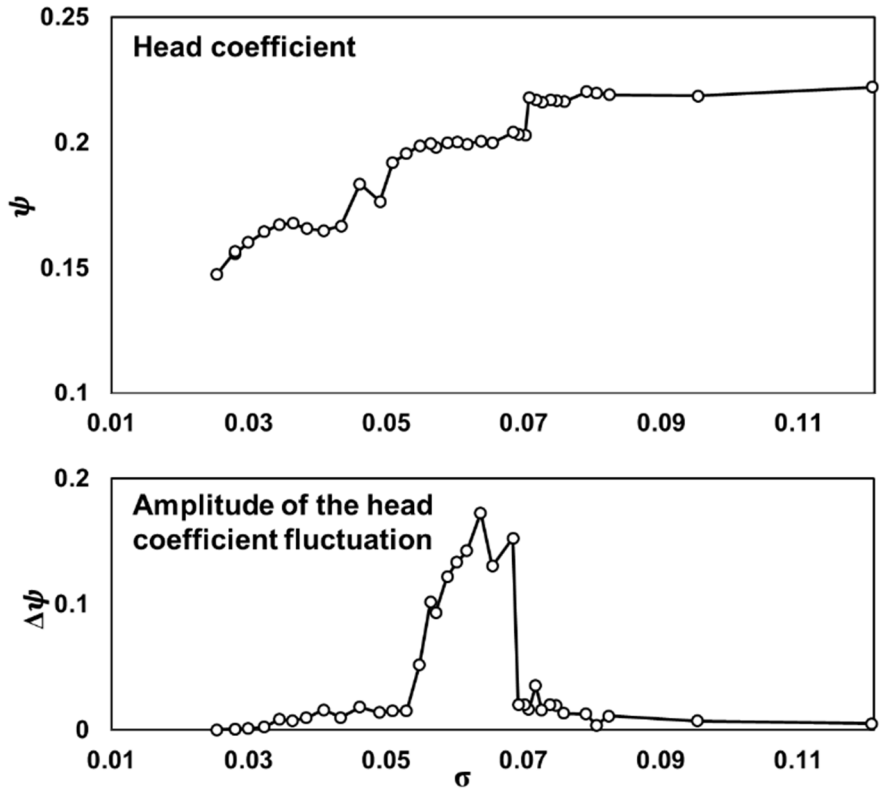

Figure 3.11 Cavitation performance and the amplitude of unsteady pressure fluctuation at the rotating cavitation frequency (ϕ_d=0.096, T_∞=298 K)

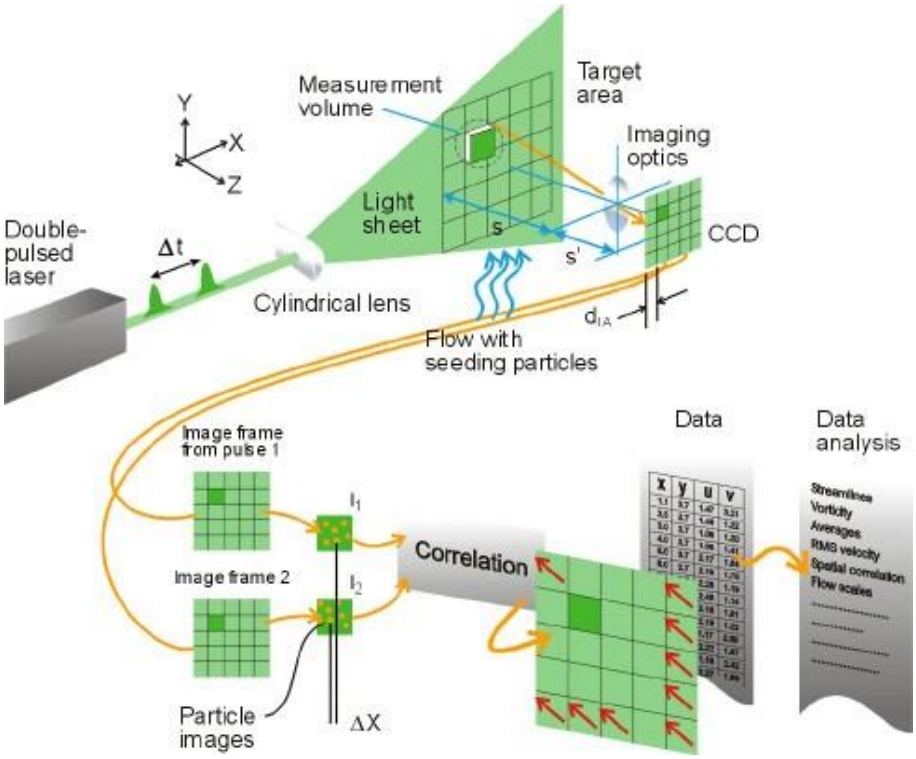

Figure 3.12 Schematic of PIV technique [73].

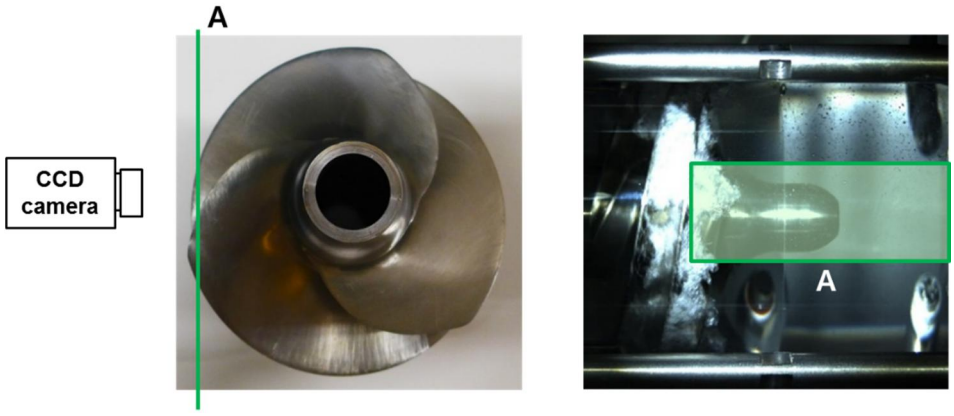

Figure 3.13 The location of laser sheet.

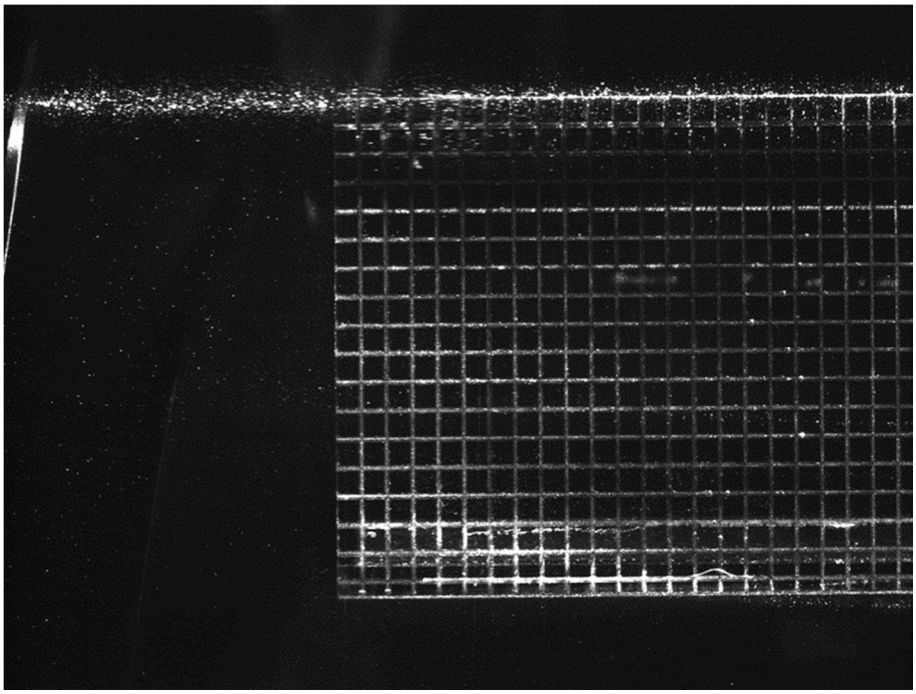

Figure 3.14 Calibration data.

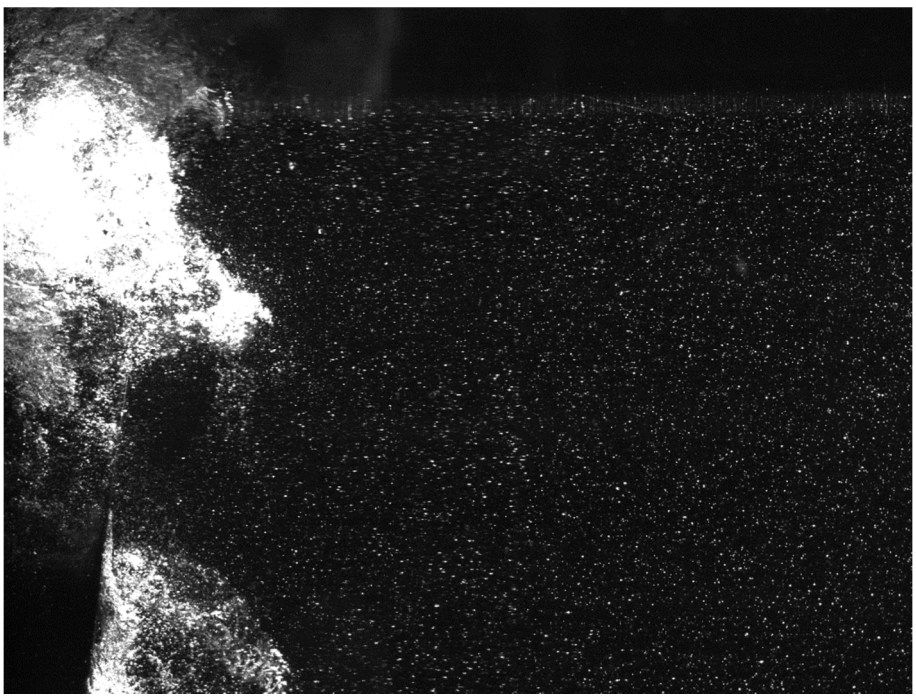

Figure 3.15 Raw image of tracer particles.

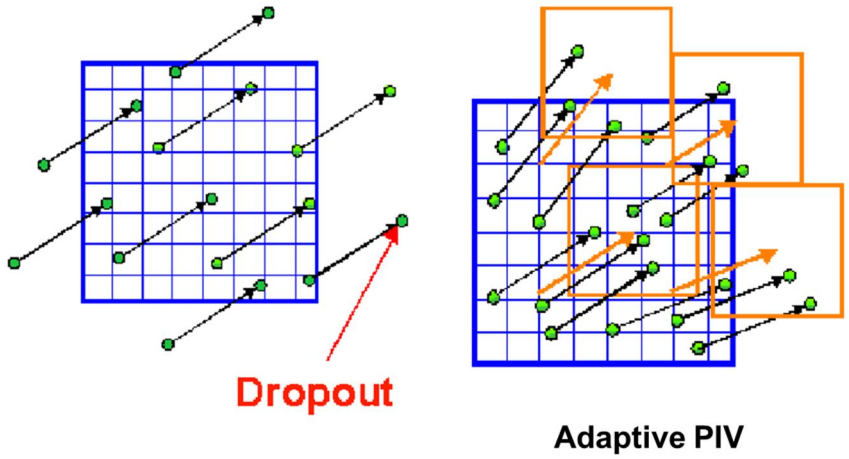

Figure 3.16 Principle of Adaptive PIV method [75].

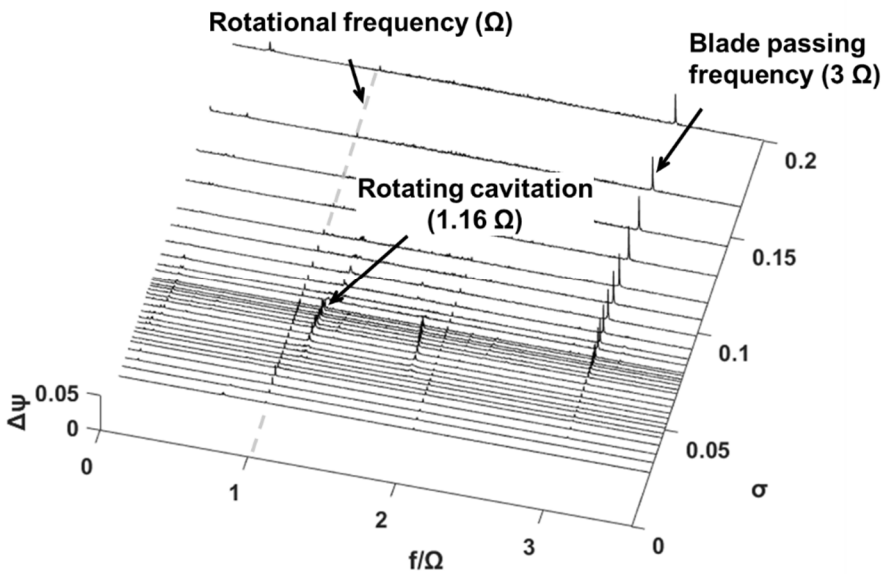

Figure 3.17 The power spectral density of inducer inlet pressure fluctuations for the casing without the ramp (ϕ/ϕ_d=1.03, T_∞=298 K, 5,000 rpm).

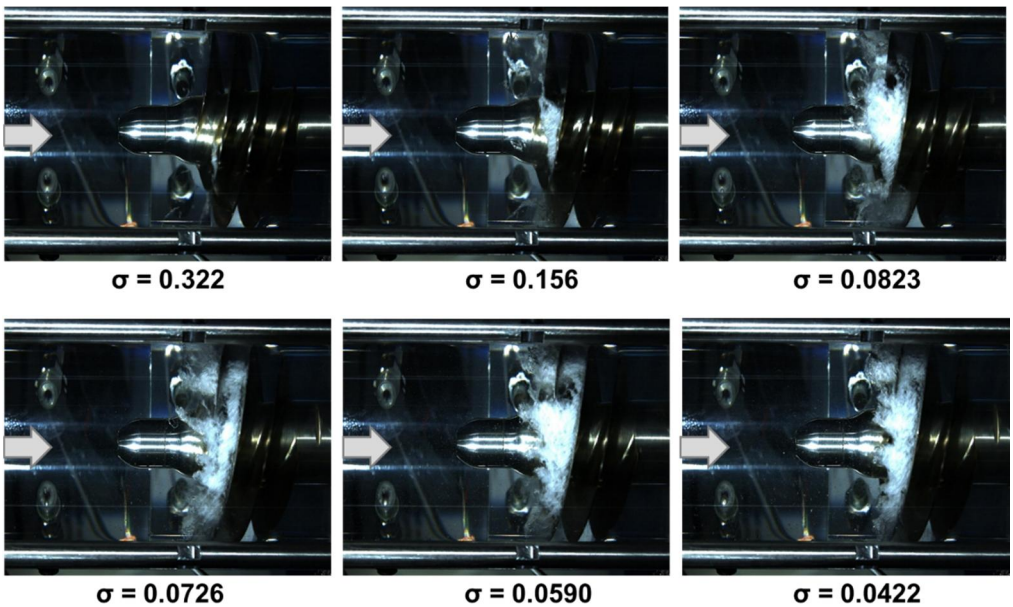

Figure 3.18 Development of tip leakage vortex cavitation at the inducer for the casing without the step.

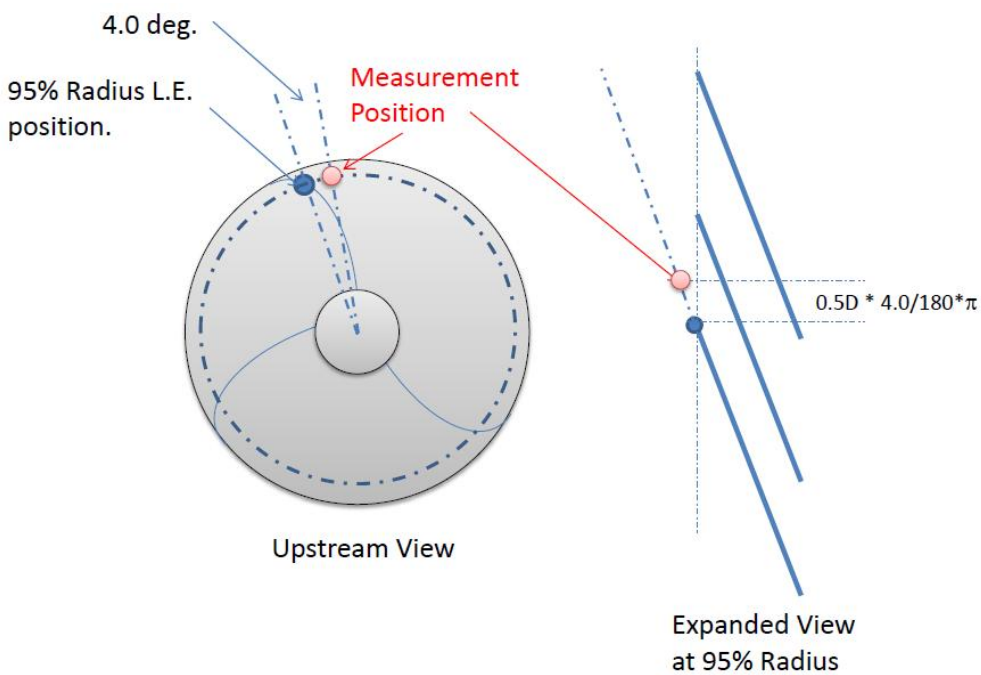

Figure 3.19 Measurement location of the incidence angle.

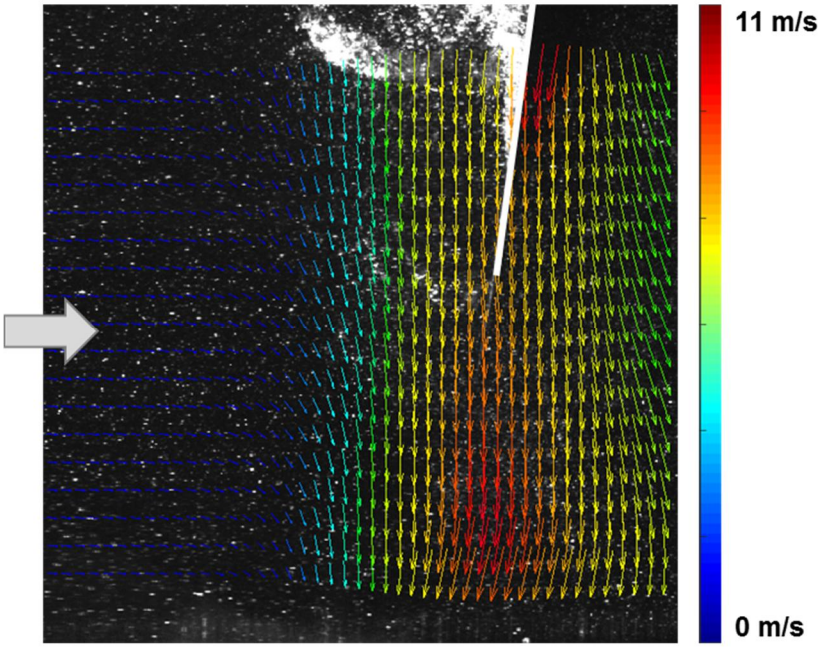

Figure 3.20 Raw image and velocity vector (200 pictures ensemble average) under no rotating cavitation.

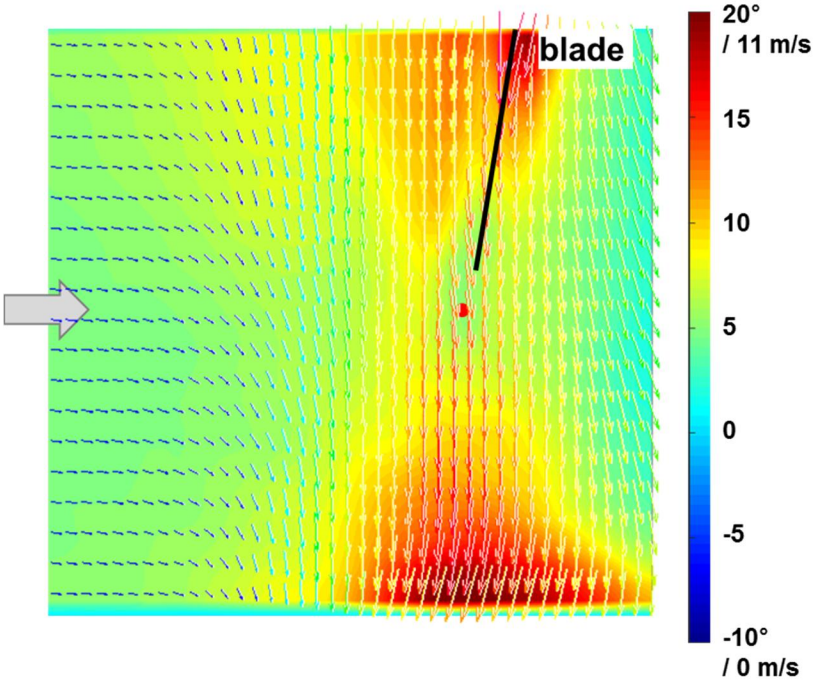

Figure 3.21 Incidence angle and velocity vector contours with ensemble average (200 pictures) under no rotating cavitation.

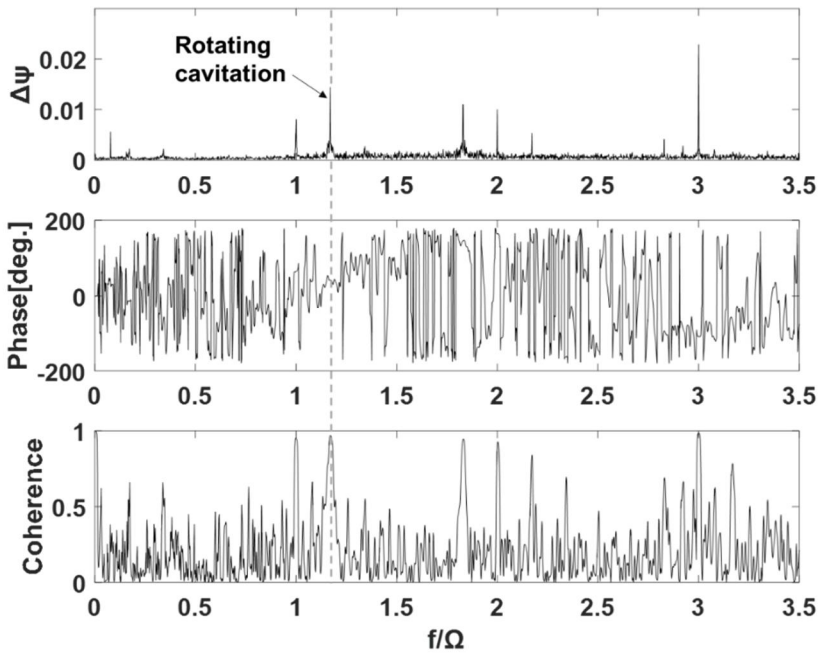

Figure 3.22 The power spectral density, phase difference, and coherence of unsteady pressure fluctuations from two pressure transducers with 45° angular separation in upstream of the inducer under rotating cavitation condition with PIV particles (σ=0.070, ϕ/ϕ_d=1.03, T_∞=298 K).

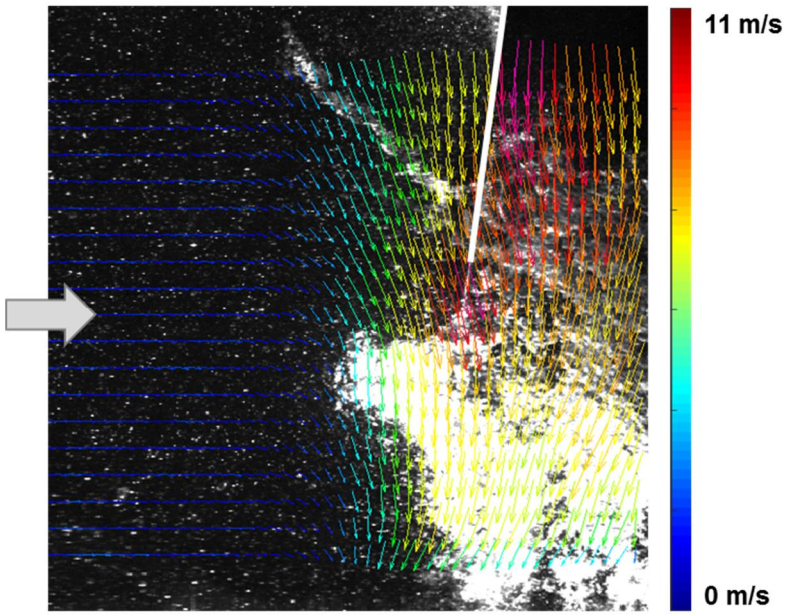

Figure 3.23 Raw image and velocity vector (24 pictures ensemble average) in case of the large cavitation under rotating cavitation.

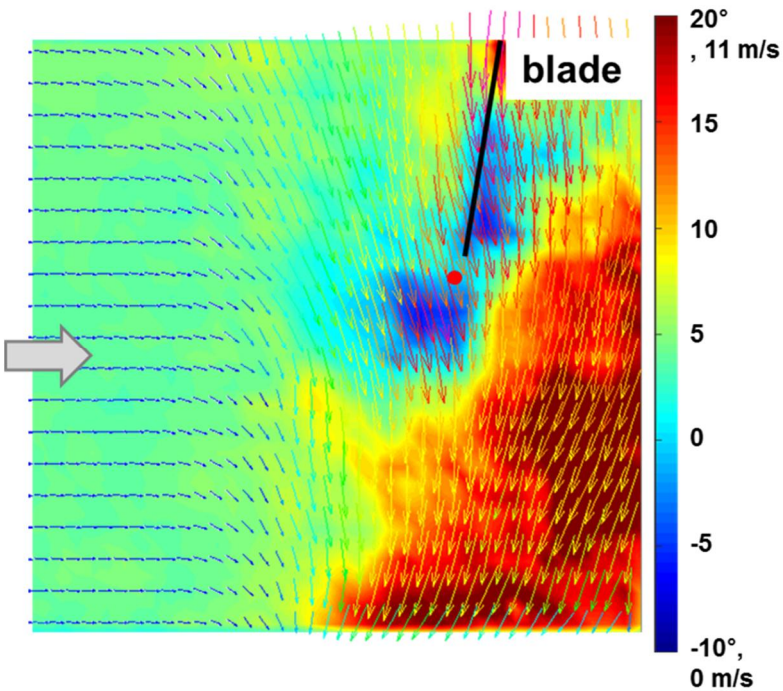

Figure 3.24 Incidence angle and velocity vector contours with ensemble average (24 pictures) in case of the large cavitation under rotating cavitation.

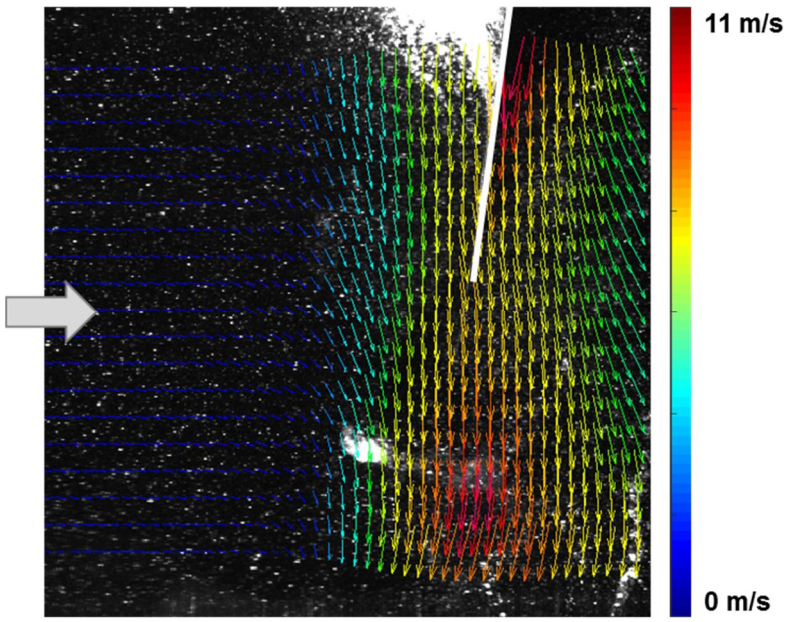

Figure 3.25 Raw image and velocity vector (24 pictures ensemble average) in case of the small cavitation under rotating cavitation.

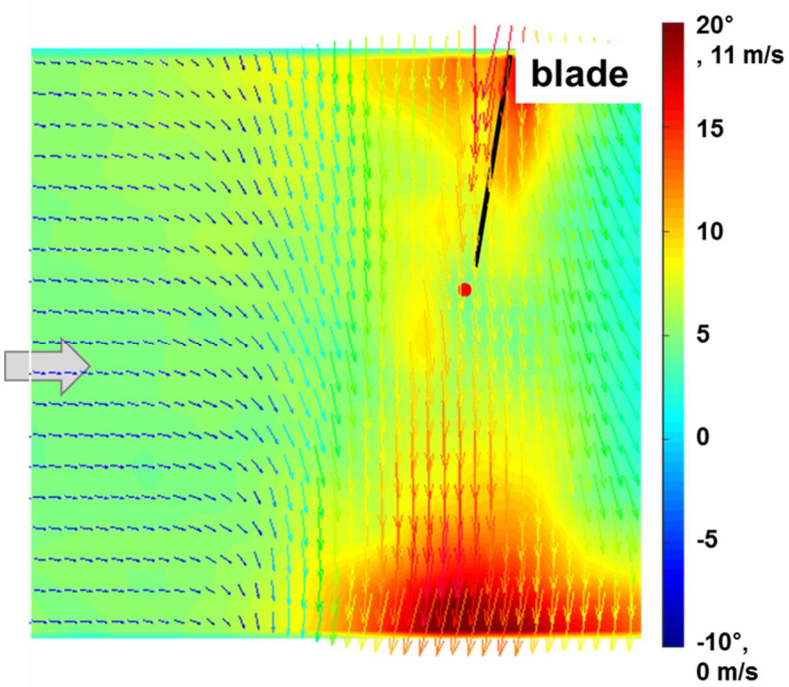

Figure 3.26 Incidence angle and velocity vector contours with ensemble average (24 pictures) in case of the small cavitation under rotating cavitation.

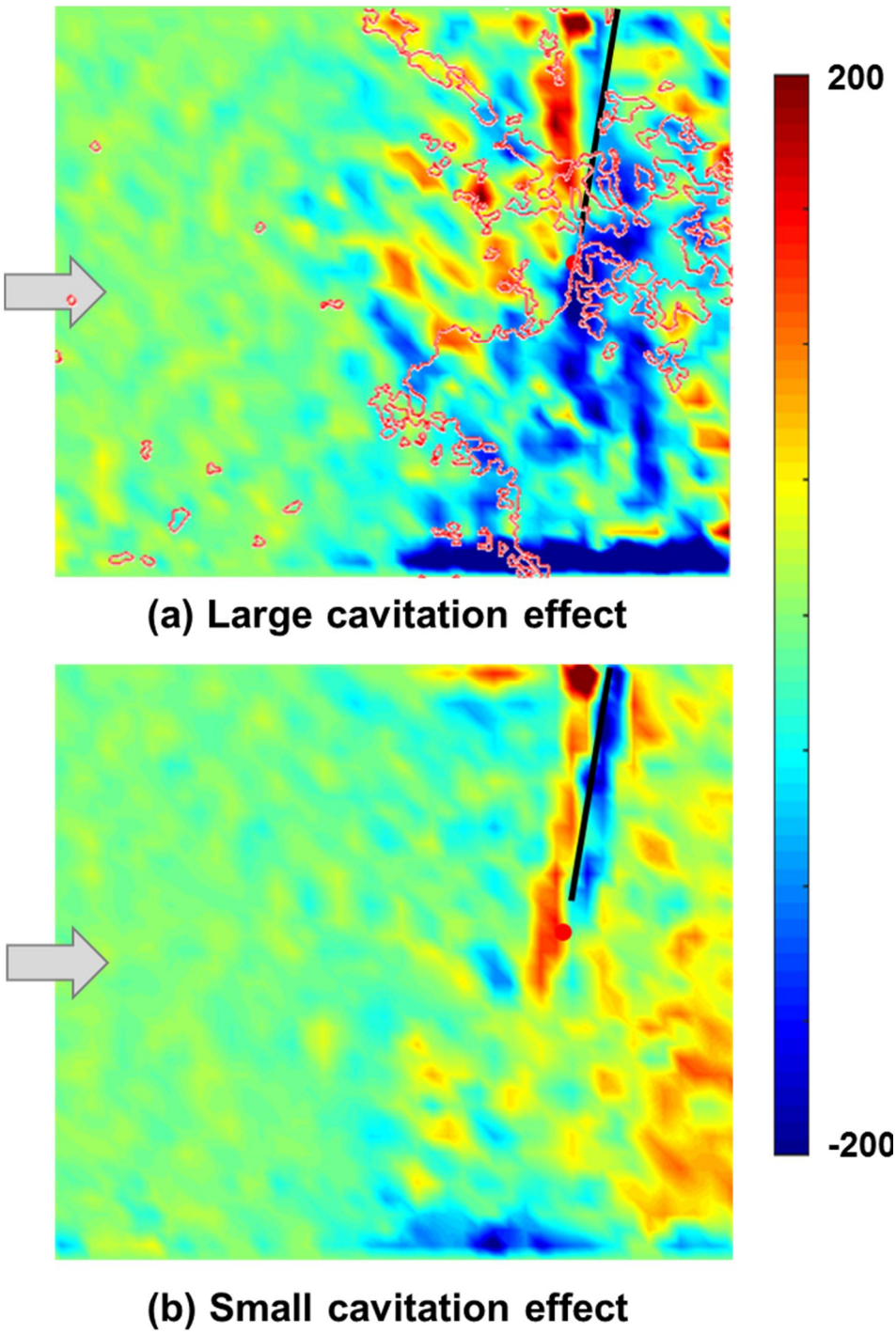

Figure 3.27 Velocity divergence contour of ensemble average at σ=0.070 for (a) large cavitation effect and (b) small cavitation effect.

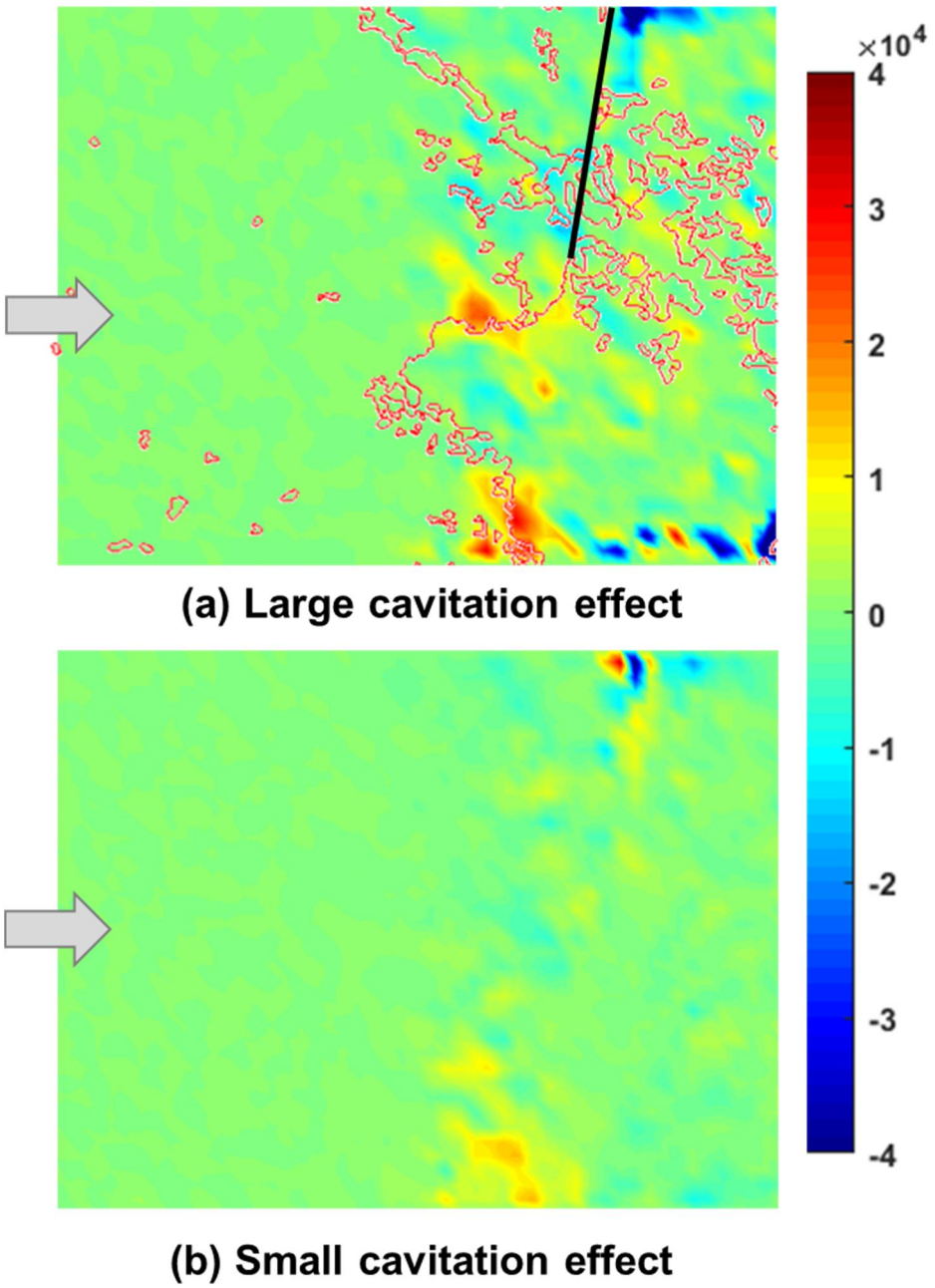

Figure 3.28 2nd invariant Q contour at σ=0.070 for (a) large cavitation case and (b) small cavitation case.

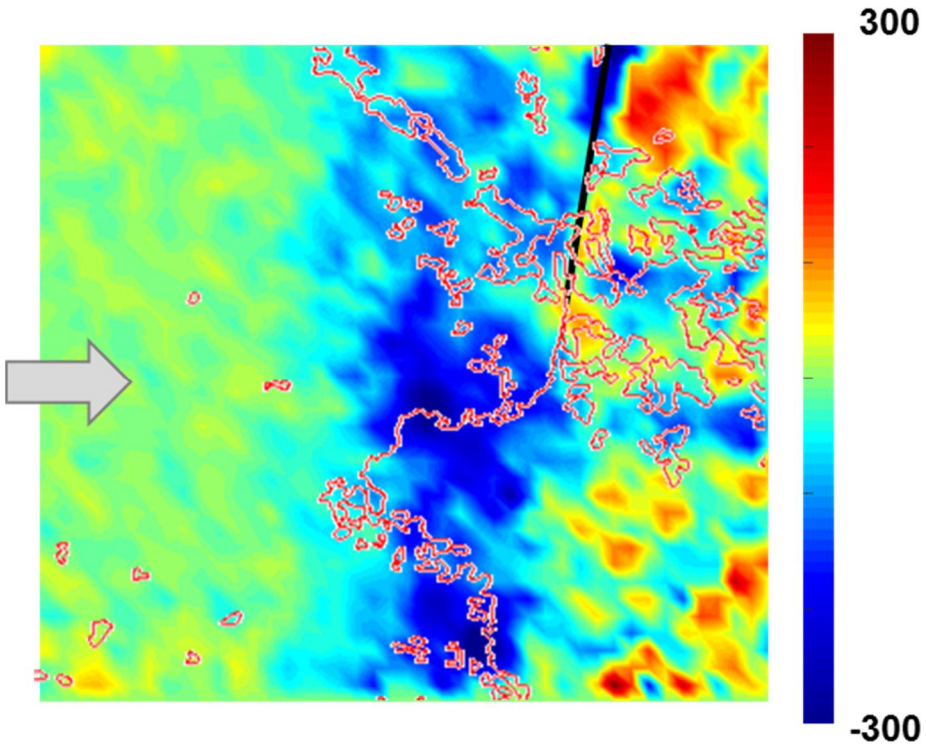

Figure 3.29 Vorticity contour at σ =0.070 for large cavitation case.

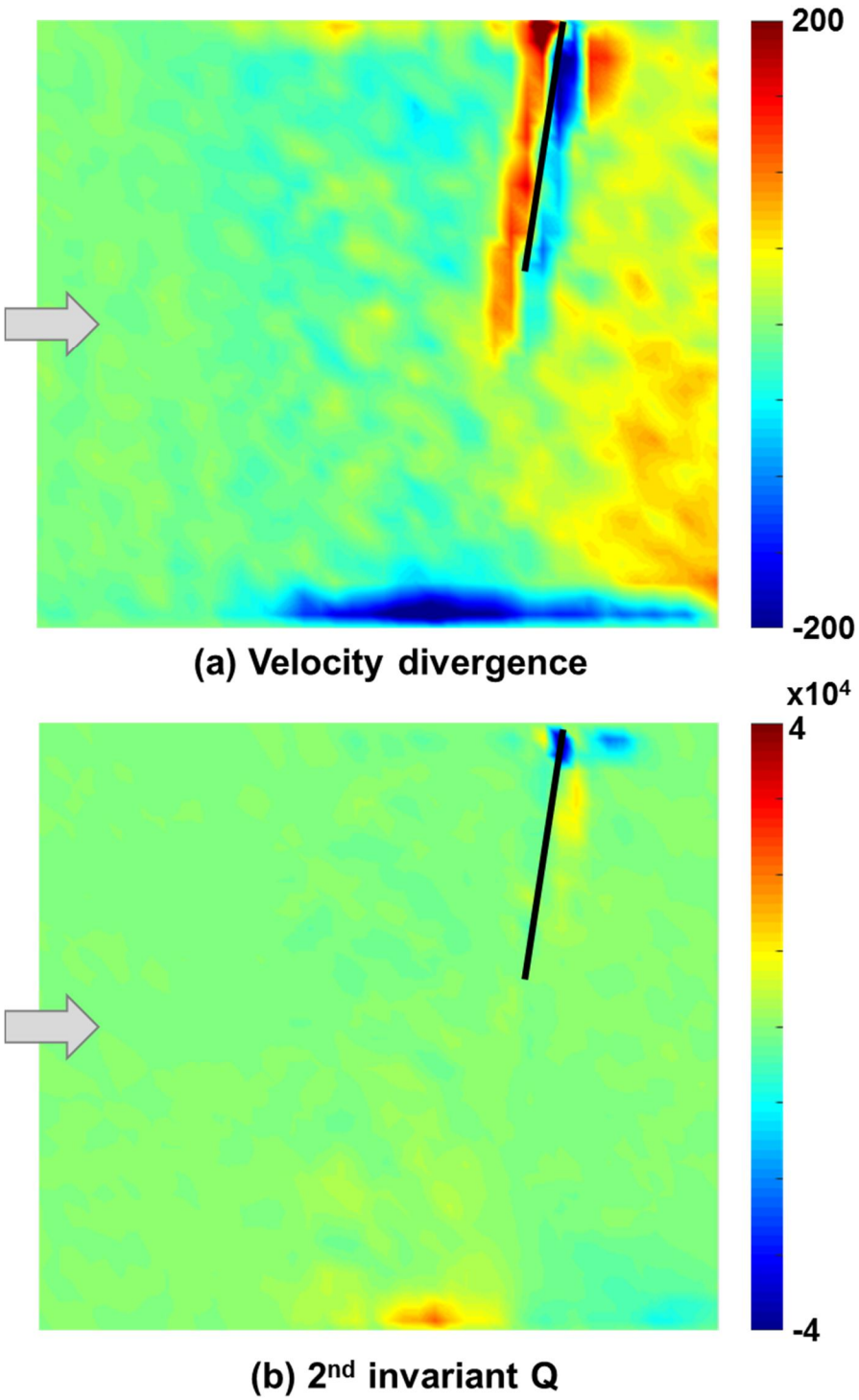

Figure 3.30 Velocity divergence and 2nd invariant Q contours under no rotating cavitation.

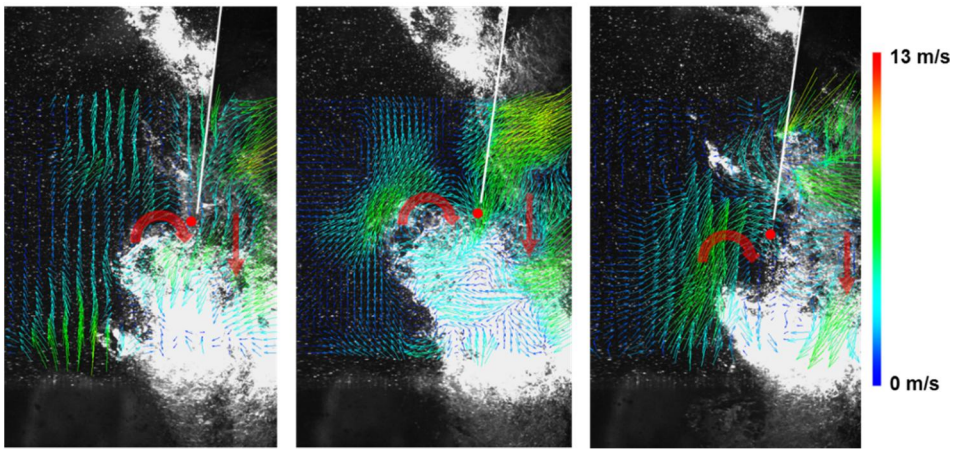

Figure 3.31 Rotating cavitation velocity vectors subtracted from the non-cavitating condition.

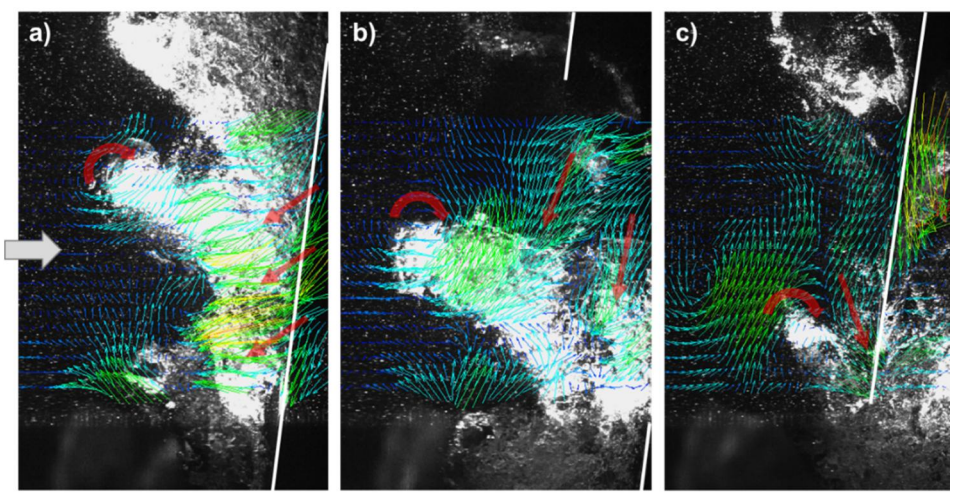

Figure 3.32 Velocity vectors of rotating cavitation conditions is subtracted from non-cavitating velocity vectors with different position of blade and tip leakage vortex cavitation region.

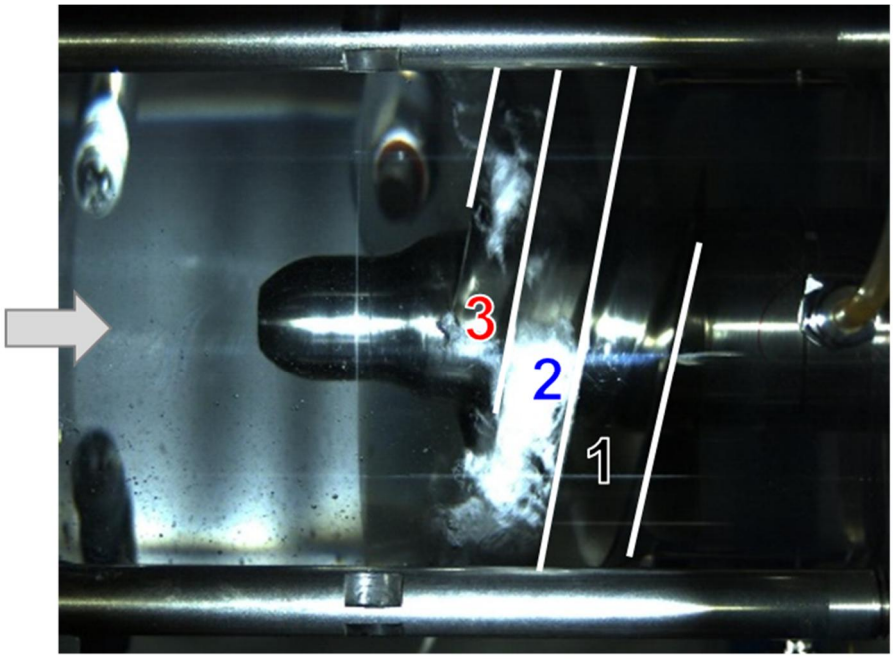

a) Small cavitation region of blade 3

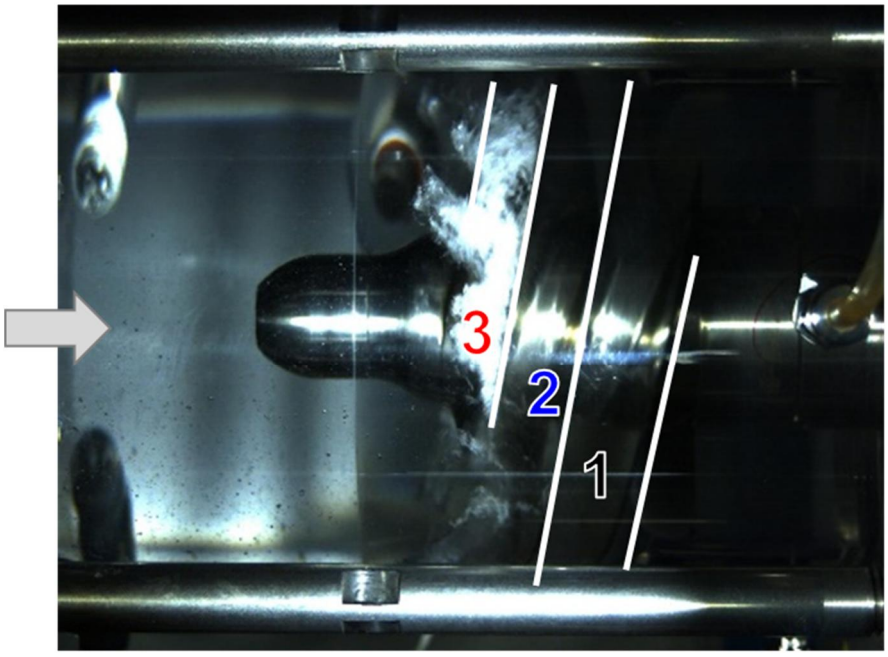

b) Large cavitation region of blade 3

Figure 3.33 High speed camera visualization when small cavitation region (a) and large cavitation region (b) at the front

blade under rotating cavitation.

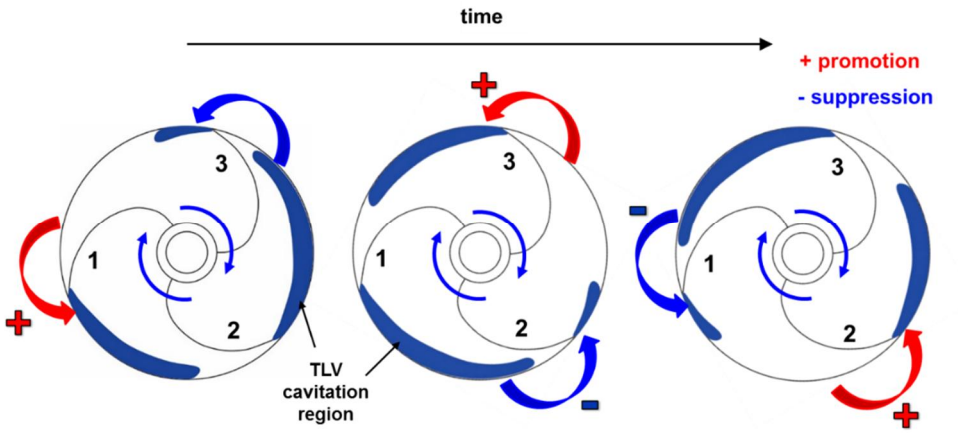

Figure 3.34 Pulsation mechanism of each cavitation region under rotating cavitation.

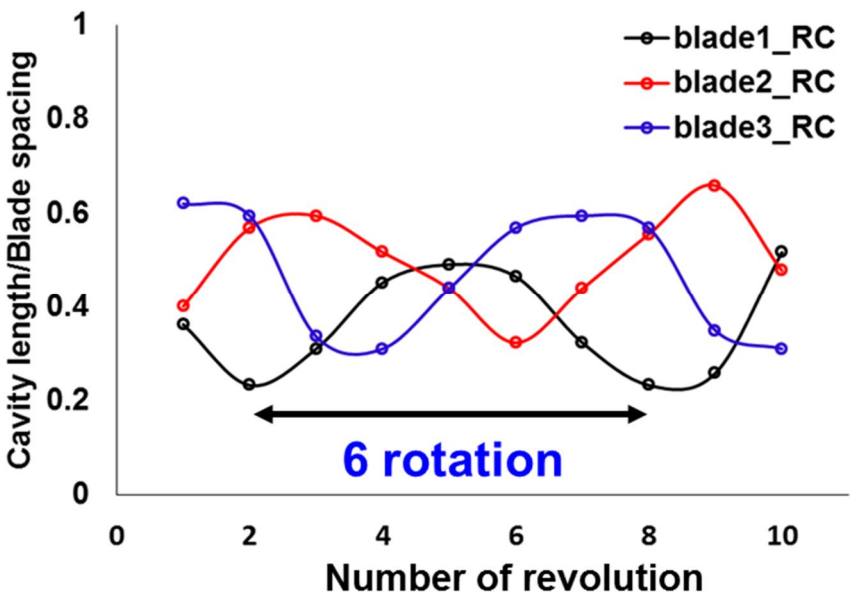

Figure 3.35 The normalized tip leakage vortex cavitation length change according to the revolution with rotating cavitation (σ=0.075).

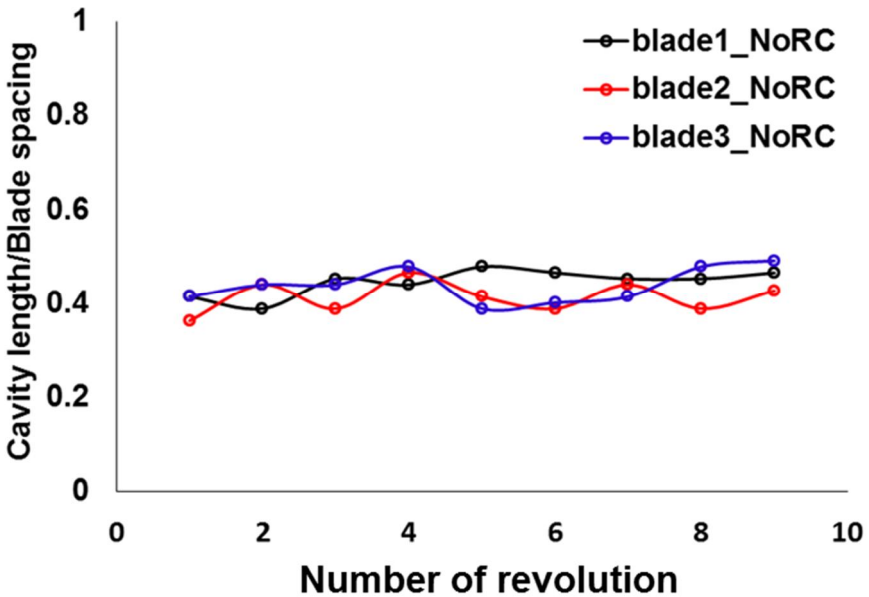

Figure 3.36 The normalized tip leakage vortex cavitation length change according to the revolution without rotating cavitation (σ=0.085).

Table 3.1 PIV experiment settings.

Laser sheet	Type	ND;Yag−532 nm
	Power	120 mJ
	Thickness	1.2 mm
Camera	Resolution	1376 x 1040 pixels
	Repetition rate	4 Hz
Seeding	Type	Silver coated hollow glass spheres
	Stokes number	0.003 (tracing error is less than 1 %)
Imaging	Lens focal length	45 mm
	F−number	4
	Δt	20 μs
PIV analysis	Software	Dantec DynamicStudio
	Interrogation area	32 x 32 pixels Grid step: 16 pixels 50 % overlap
	Averaging	3 x 3 average

Chapter 4. Thermal Effects on Cavitation Performance and Cavitation Instability

4.1. Temperature effects

4.1.1. Test Condition

To understand thermal effects on cavitation performance and cavitation instabilities, experiments have been firstly performed at various water temperature and constant rotational speed (5,000 rpm). Tests have been conducted at water temperatures of 298 K, 313 K, 328 K, 340 K, and 357 K, and the corresponding non-dimensional thermal parameters (Σ^*) are listed in Table 4.1. During the experiments, Bulk water temperature has been maintained to within ±0.1 K during the test. The inducer radius (0.047 m) and tip velocity (24.7 m/s) are the characteristic length and reference velocity. As water temperature increases, Σ^* is increased, and Σ^*value at 357 K is equivalent to Σ^* of liquid oxygen at cryogenic conditions. Thus, for this inducer, when the water temperature is above 357 K, cryogenic conditions in terms of Σ^* can be simulated.

4.1.2. Temperature Effects on Cavitation Performance and Rotating Cavitation Onset

Figure 4.1 shows plots of the head coefficient versus cavitation

number for various values of Σ^*. Arrows show the critical cavitation number for each Σ^* values. The critical cavitation number decreases as Σ^* increases. However, for cavitation numbers lower than the critical cavitation number, the head coefficient is independent of Σ^*. The sensitivity of cavitation instability to Σ^* also has been investigated. Figure 4.2 presents the power spectral density for Σ^* from 0.0539 to 1.80. The trend of dominant peak transition from f/Ω = 3.0 to 1.0 remains the same despite Σ^* variations. The onset cavitation number and amplitude of unsteady pressure fluctuation of rotating cavitation (RC) are decreased as Σ^* increases.

The dependence of the critical cavitation number and the rotating cavitation onset on Σ^* are clearly shown in Fig. 4.3. For Σ^* from 0.0116 to 0.540, the critical cavitation number is decreased by 15 %. For Σ^* from 0.540 to 1.80 (equivalent to the cryogenic condition), the critical cavitation number is independent of Σ^*. Therefore, similarity with cryogenic conditions in terms of Σ^* can be achieved with inducer water testing for $\Sigma^* > 0.540$.

Figure 4.3 also shows that the rotating cavitation onset cavitation number decreases by 15 % as Σ^* increases from 0.0116 to 0.540. As also indicated by Horiguchi et al. [34], rotating cavitation starts to occur when the cavity length reaches about 65 % of the blade spacing. Yoshida et al [46] also confirmed that cavitation region length is shorter at the high Σ^* than at the low Σ^* at same cavitation number. Thus, the cavitation number for the onset of rotating cavitation shifts to lower values at high Σ^*. Therefore, the onset of rotating cavitation is delayed as Σ^* increases. On the other hand, for Σ^* from 0.540 to 1.80, the onset cavitation number of rotating cavitation is independent of Σ^*.

Figure 4.3 also shows that the cavitation number corresponding to the onset of rotating cavitation correlates well with the critical cavitation number at all values of Σ^*. Thus, onset of the rotating cavitation leads to the onset of the head coefficient degradation regardless of Σ^* variations.

4.2. Non-dimensional Parameters for Cavitating Inducer

Previous researchers investigated the thermal effect on cavitating inducers by varying either the liquid temperature or rotational speed, but they did not consider viscous effects. However, when either the liquid temperature or rotational speed is changed, not only Σ^* but also the Reynolds number ($Re = 2\rho_l r\Omega^2/\mu_l$) is simultaneously changed. In above results, as Σ^* was increased from 0.0116 to 1.80, the Reynolds number ranged from 2.6×10^6 to 6.4×10^6 as well. It indicates that Reynolds number possibly affects the occurrence of rotating cavitation.

To identify the non-dimensional parameters governing cavitation growth in an inducer, the Rayleigh-Plesset equation for bubble dynamics is presented in Eq. (1.2). Following Franc et al. [54], time have been normalized by x/U where x is the distance along the streamline followed by the bubble; U is the inducer blade tip rotational speed; and C is the inducer radius. Surface tension (S) and non-condensable gas effects (p_{G0}) are negligible after the initial stage of bubble formation [4]. The resulting non-dimensional Rayleigh-Plesset equation is then:

$$\bar{R}\frac{d^2\bar{R}}{d\bar{x}^2}+\frac{3}{2}\left(\frac{d\bar{R}}{d\bar{x}}\right)^2+\left(\Sigma^*\sqrt{\bar{x}}+\frac{4}{Re\bar{R}}\right)\frac{d\bar{R}}{d\bar{x}}=-\frac{Cp+\sigma}{2} \quad (4.1)$$

In Eq. 4.1, Σ^* and Re are the two non-dimensional parameters which affect cavitation bubble growth. Increasing liquid temperature increases both Σ^* and Re. Increasing inducer blade tip velocity increases Re but decreases Σ^*.

4.3. Non-dimensional Parameter Effects

4.3.1. Non-dimensional Thermal Parameter (Σ^*) Effects for Constant Reynolds Number

To investigate the effects of Σ^* for constant Reynolds number, Σ^* has been varied from 0.0227 to 1.55 while Re has been held constant at 4.15×10^6. The test conditions are summarized in Table 4.2. From heat transfer analysis [78], the temperature difference between the bulk water and wall varies from 0.04 K (308 K and 6,400 rpm) to 0.09 K (347 K and 3,500 rpm). The analysis procedure is described in the Appendix B. The value of $\Sigma^* = 1.59$ is similar to $\Sigma^* = 1.81$ of the KARI liquid oxygen (LOX) inducer under the actual operating conditions (87 K and 20,000 rpm).

Figure 4.4 presents the power spectral density plots of the inlet unsteady pressure fluctuations for Σ^* ranging from 0.0229 to 1.59 at $Re = 4.15 \times 10^6$. The arrows indicate the onset of rotating cavitation, σ_{RC}. The onset cavitation number and magnitude of the rotating cavitation at $f/\Omega = 1.14$ are decreased as Σ^* increases.

Figure 4.5 shows the σ_{RC} plotted versus Σ^*. σ_{RC} monotonically decreases by 21 % as Σ^* is increased from 0.0229 to 1.59.

High-speed camera flow visualization qualitatively confirms this trend. Figure 4.6 (a) shows the cavitation region on an inducer blade for Σ^* = 0.0229, and Fig. 4.6 (b) shows the same blade for Σ^* = 1.59 at σ = 0.081 and Re = 4.15×10^6. The cavitation region for Σ^* = 1.59 is visibly smaller than that for Σ^* = 0.0229. The visualization data are qualitatively consistent with the unsteady pressure data and confirm that increasing Σ^* suppresses the rotating cavitation onset.

Ruggeri and Moore [42] defined the minimum cavitation number, σ_{eff}, which determines the cavitation bubble growth by considering the thermal effect (Eq. 4.2) as

$$\sigma_{eff} = \frac{p_\infty - p_{v,B}}{\frac{1}{2}\rho_l U^2} = \sigma + \frac{p_{v,\infty} - p_{v,min}}{\frac{1}{2}\rho_l U^2} = \sigma + \frac{\Delta p_v}{\frac{1}{2}\rho_l U^2} \quad (4.2)$$

where $p_{v,B}$ is the minimum vapor pressure within the cavitation bubble. The minimum cavitation number is the sum of the nominal cavitation number (σ) and the vapor pressure depression (Δp_v) normalized by the dynamic head ($\frac{1}{2}\rho_l U^2$). As Σ^* is increased, Δp_v of the cavitation bubbles is increased, and σ_{min} increases. Thus, increasing Σ^* inhibits rotating cavitation onset.

4.3.2. Reynolds Number Effects for Constant Non-dimensional Thermal Parameter (Σ^*)

Table 4.3 lists the test conditions for Re effects. Figure 4.8 shows the cavitation performance at Re = 2.30×10^6, 2.50×10^6, and

3.17×10^6 for Σ^* = 0.0125. Figure 4.9 shows the corresponding data at Re = 4.81×10^6, 5.75×10^6, and 6.84×10^6 for Σ^* = 1.23. The each arrow indicates σ_{crit}. For Σ^* = 0.0125, σ_{crit} is constant as Re increases. For Σ^* = 1.26, σ_{crit} increases as Re increases from 4.81×10^6 to 6.84×10^6.

Figure 4.7 shows the power spectral density plots at Re = 2.30×10^6 (Fig. 4.7 (a)) and 3.17×10^6 (Fig. 4.7 (b)) for Σ^* = 0.0125. Figure 4.8 shows the corresponding data at Re = 4.81×10^6 (Fig. 4.8 (a)) and 6.84×10^6 (Fig. 4.8 (b)) for Σ^* = 1.26. The arrows indicate σ_{RC}. For Σ^* = 0.0125, σ_{RC} remains constant as Re increases. For Σ^* = 1.26, σ_{RC} at Re = 6.84×10^6 is higher than that at Re = 4.81×10^6.

The dependence of σ_{RC} on Re for various values of Σ^* is presented in Fig. 4.9. As described above, the dependence of σ_{RC} corresponds to the σ_{crit}. For Σ^* = 0.0125, σ_{RC} is independent of Re. On the other hand, for $\Sigma^* \geq 0.0537$, σ_{RC} increases with increasing Re, and such Re effects (e.g. $\frac{\partial(\sigma_{RC})}{\partial(Re)}$) become stronger as Σ^* increases. Visualization of the cavitation on inducer blades qualitatively confirms such Re effects. Figure 4.10 shows the inducer blade cavitation at Re = 2.30×10^6 (Fig. 4.10 (a)) and 3.17×10^6 (Fig. 4.10 (b)) for Σ^* = 0.0125. For Σ^* = 0.0125, the length of the inducer blade cavitation region is not affected by the Re change. For sufficiently low Σ^* (e.g. 0.0125), where the thermal effect is negligible [4], the vapor pressure depression is also negligible ($\Delta p_v \approx 0$). Therefore, σ_{min} (Eq. 4.2) and σ_{RC} are insensitive to Re for low Σ^*.

Figure 4.11 shows the cavitation region on an inducer blade for Σ^* = 1.23 at Re = 4.81×10^6 (Fig. 4.11 (a)) and 6.84×10^6 (Fig. 4.11 (b)). For Σ^* = 1.23, the length of the inducer blade cavitation

region at Re = 6.84×10^6 is visibly longer than that at Re = 4.81×10^6. Thus, the rotating cavitation onset depends on Re at Σ^* = 1.23. Tokumasu et al. [79] performed a numerical analysis of the Re effects on cavitation growth for a hydrofoil. They found that the cavitation region is bigger at a higher Re in liquid oxygen in which the thermal effect is significant. For high Σ^* values, where the thermal effect is significant, as Re increases, the dynamic head ($\frac{1}{2}\rho_l U^2$) in Eq. 4.2 increases, reducing σ_{min}. Thus, increasing Re promotes cavitation region growth, and the rotating cavitation onset occurs at a higher cavitation number. In typical rocket engines, Σ^* (1.5 ~ 30) and Re (1.0×10^7~10^8) are larger than the tested conditions. Thus, the effects of Σ^* and Re are expected to be more significant in real operating conditions.

4.3.3. Combined Effects of Non-dimensional Thermal Parameter (Σ^*) and Reynolds Number

Based on the current results, Fig. 3.14 can be explained as follows. Figure 4.12 shows the combined plots of Fig. 4.3 and Fig. 4.5. In temperature effects experiments, experiments had been performed by varying Σ^* while maintaining a constant rotational speed of 5,000 rpm. Thus, Re increased from 2.6×10^6 to 6.4×10^6 simultaneously as Σ^* was increased from 0.0116 to 1.80. In Fig. 3.25, σ_{RC} becomes independent of Σ^* for $\Sigma^* > 0.54$ at N = 5,000 rpm. On the other hand, σ_{RC} continues to decrease for $\Sigma^* > 0.54$ at Re = 4.15×10^6. In the N = 5,000 rpm study, the cavitation suppression effects due to the increase in Σ^* and the cavitation promotion effects due to the increase in Re occurred simultaneously. For $\Sigma^* < 0.54$, the Re effects were weaker, and, thus, σ_{RC} was

decreased as Σ^* increased. However, as Σ^* increased further, the Re effects became stronger, essentially cancelling out the Σ^* effects. Thus, σ_{RC} became "seemingly" independent of Σ^* for $0.54 < \Sigma^* < 1.80$ for N = 5,000 rpm. However, when Re is kept constant at 4.15×10^6 in the current study, σ_{RC} is decreased as Σ^* increases.

Similar experimental results supporting the current research had been shown in the results of Kikuta et al.' s [58] (Fig. 4.13). They performed experiments in liquid Nitrogen. They reported Σ^* effects on cavitating inducer for higher ranges of Re and Σ^*. Their Reynolds number range is on the order of 10^7, which satisfies the real rocket engine condition. They showed that the critical cavitation number is higher at Σ^* = 43.8 (86 K, 18,300 rpm) than at Σ^* = 30.9 (79 K, 10,000 rpm) in liquid nitrogen. In this case, Reynolds number at Σ^* = 43.8 is 2.25 times higher than that of Σ^* = 30.9. The increase in Reynolds number increases the critical cavitation number even though Σ^* is higher, which shows that the Reynolds number effects is stronger in high Σ^*. Therefore, the competing effect of Reynolds number and Σ^* on cavitating inducer exists in high Reynolds number. Σ^* and Reynolds number effects revealed in this study can be adapted to the real cryogenic flow inducer.

4.3.4. Non-dimensional Thermal Parameter (Σ^*) and Reynolds Number on the Critical Cavitation Number

Cavitation performances at various Σ^* and Reynolds number have been measured simultaneously. Figure 4.14 shows the cavitation performance for Σ^* ranging from 0.0229 to 1.59 at Re =

4.15×10^6. The arrows indicate the critical cavitation number, σ_{crit}. As Σ^* decreases, σ_{crit} is continuously reduced. Cavitation performances of Reynolds number variation at constant Σ^* values are shown in Appendix C (Fig. C.1 ~ C.6).

As shown in Fig. 2.26, σ_{RC} corresponds to σ_{crit} at the design flow coefficient. Figure 4.15 and 4.16 show the critical cavitation number trends for Σ^* variation at constant Reynolds number and Reynolds number variation at constant Σ^* values. The trends and the values of σ_{crit} correspond to σ_{RC} at the design flow coefficient. Thus, this coincidence occurs irrespective of thermal effects including variations of Σ^* and Reynolds number.

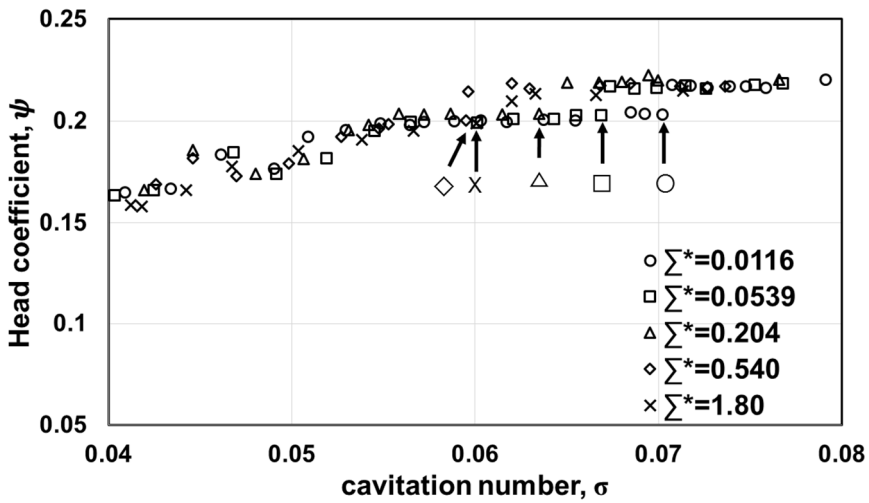

Figure 4.1 Cavitation performance of various non-dimensional thermal parameters at 5,000 rpm (ϕ/ϕ_d=1.0).

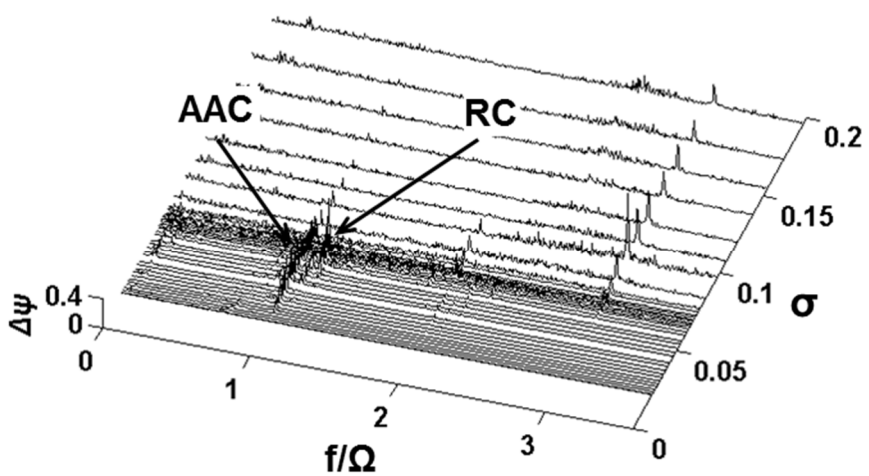

a) $\Sigma^* = 0.0539$ (T = 313 K)

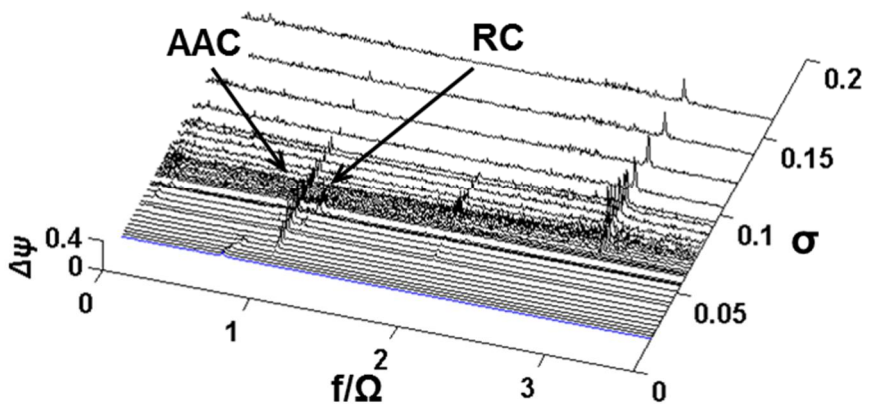

b) $\Sigma^* = 0.204$ (T = 328 K)

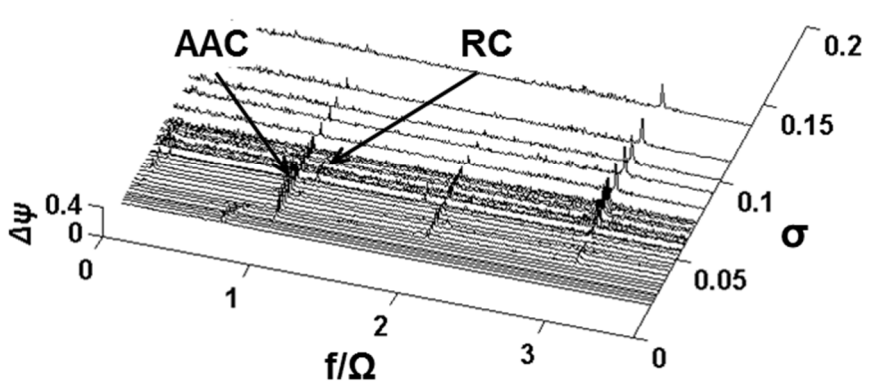

c) $\Sigma^* = 0.540$ (T = 340 K)

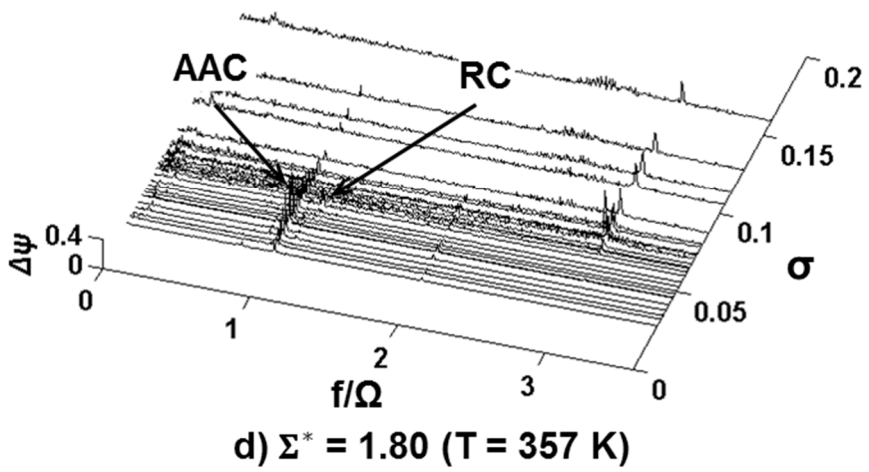

Figure 4.2 The power spectral density of inducer inlet pressure fluctuations for different Σ^* at 5,000 rpm: (a) Σ^* = 0.0539 (T = 313 K), (b) Σ^* = 0.204 (T = 328 K), (c) Σ^* = 0.540 (T = 340 K), and (d) Σ^* = 1.80 (T = 357 K) (ϕ/ϕ_d=1.0).

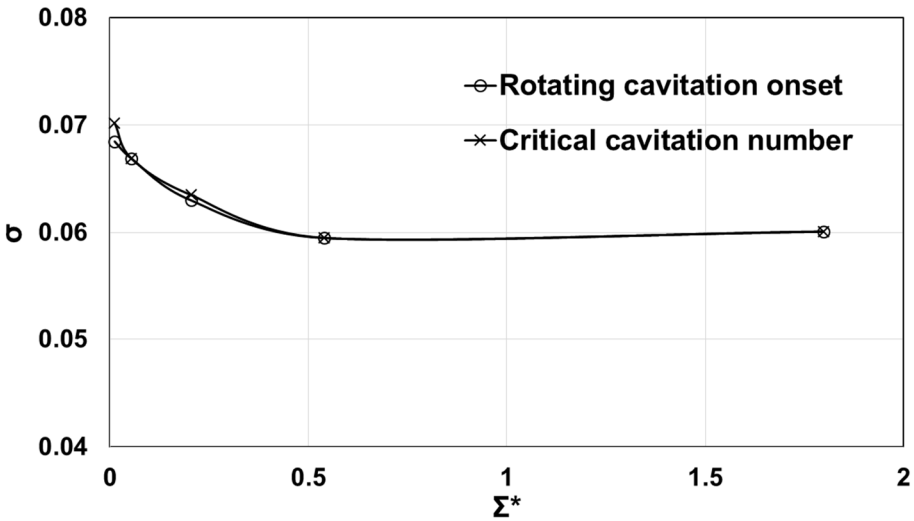

Figure 4.3 The rotating cavitation onset cavitation number and the critical cavitation number versus the non-dimensional thermal parameter at 5,000 rpm (ϕ/ϕ_d=1.0).

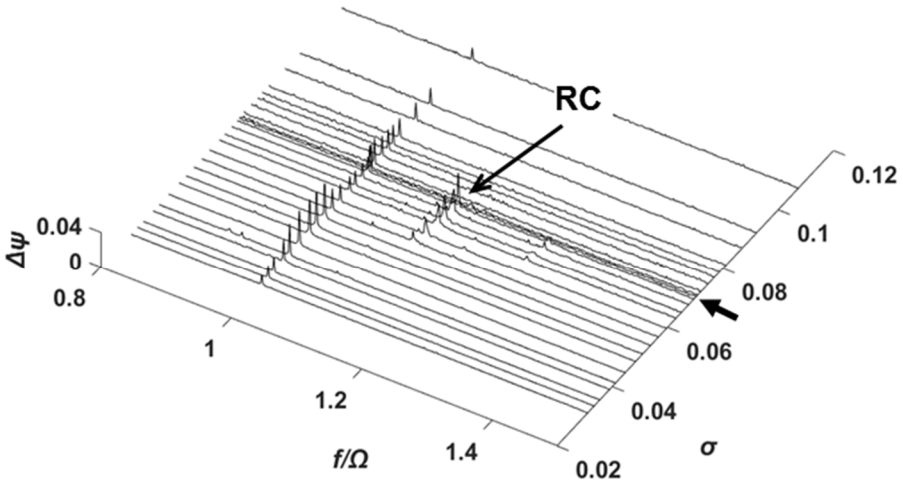

a) $\Sigma^* = 0.0229$

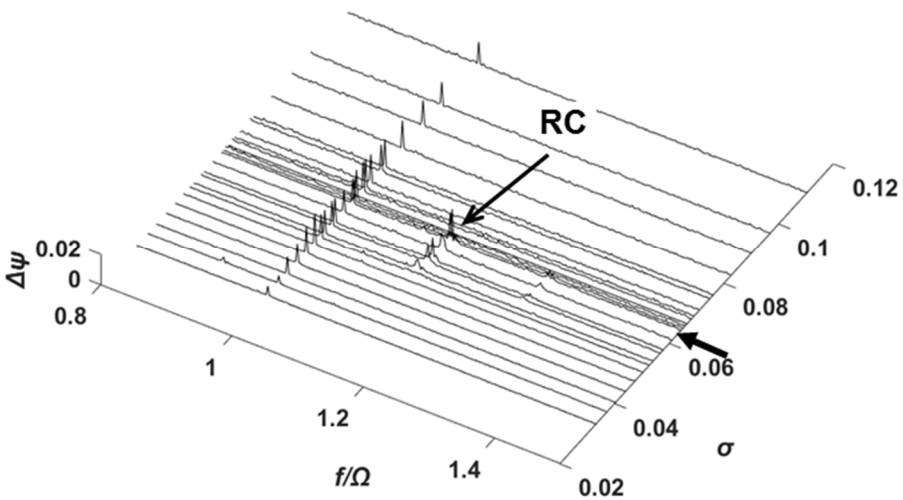

b) $\Sigma^* = 0.135$

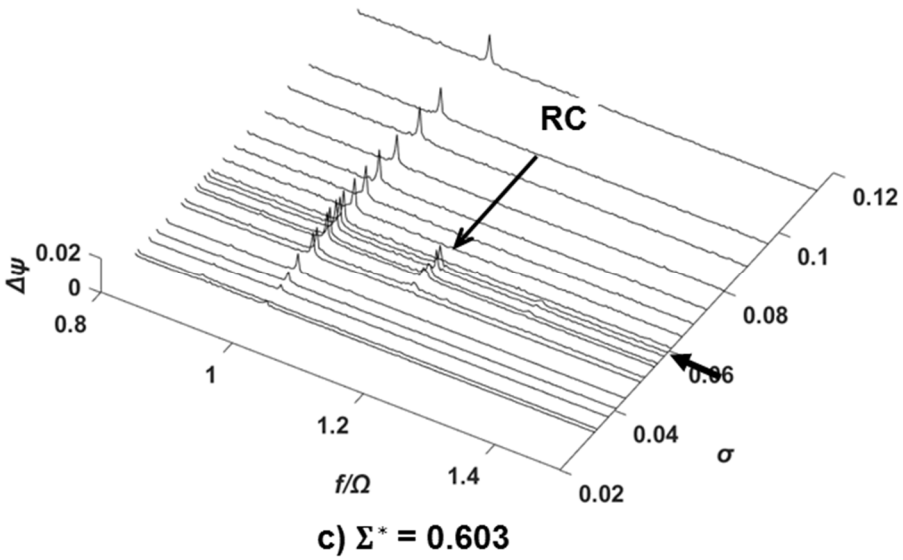

c) $\Sigma^* = 0.603$

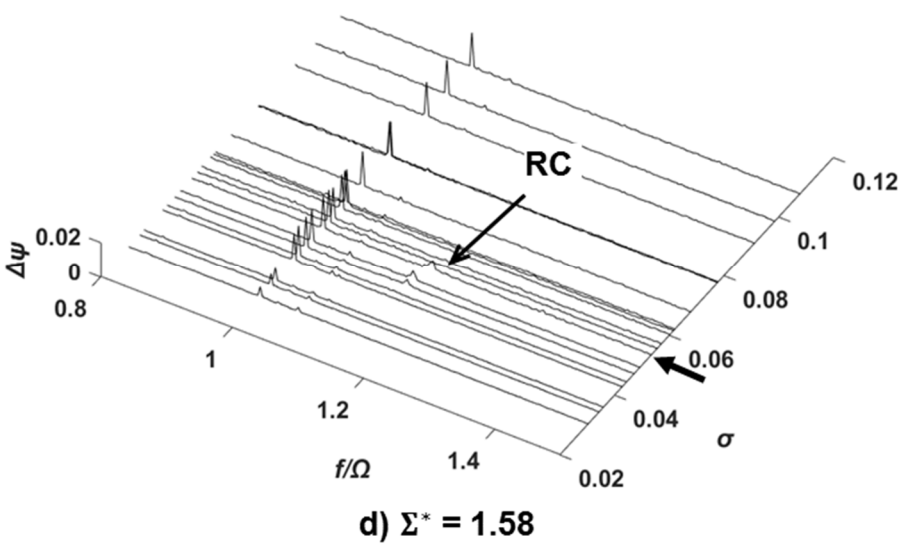

d) $\Sigma^* = 1.58$

Figure 4.4 The power spectral density of unsteady pressure fluctuation at various non−dimensional thermal parameter at Re=4.15×10^6 and ϕ/ϕ_d=1.0 ((a) Σ^*= 0.0229, (b) 0.135, (c) 0.603, (d) 1.58).

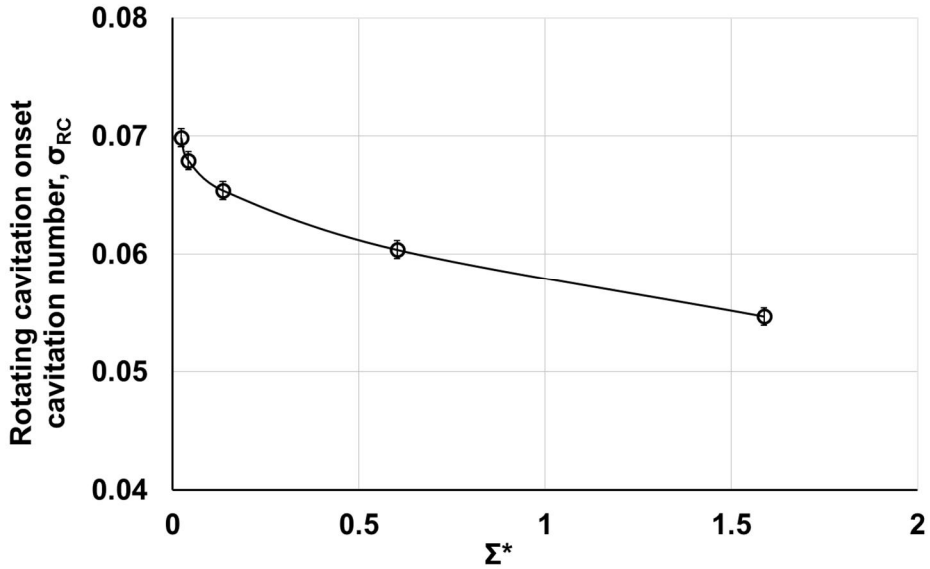

Figure 4.5 The rotating cavitation onset cavitation number versus the non-dimensional thermal parameter comparing at Re=4.15×10^6 and ϕ/ϕ_d=1.0.

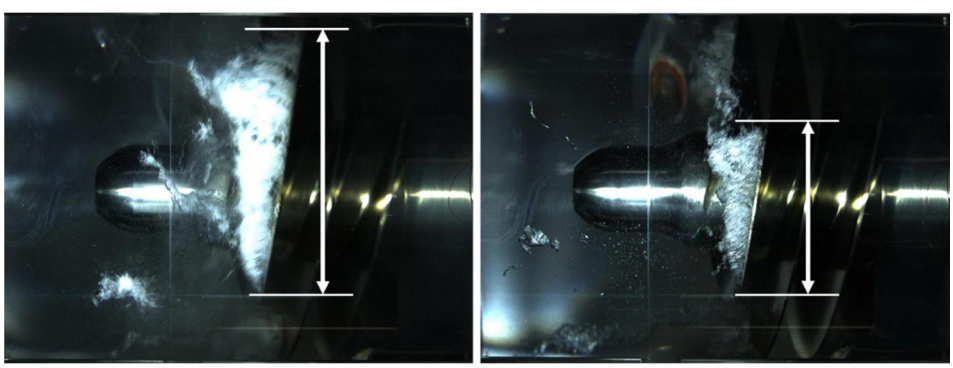

Figure 4.6 The tip leakage vortex cavitation at the inducer blade for Σ*=0.0227 (a) and 1.55 (b) (σ=0.081, ϕ/ϕ_d=1.0, Re=4.15×10^6).

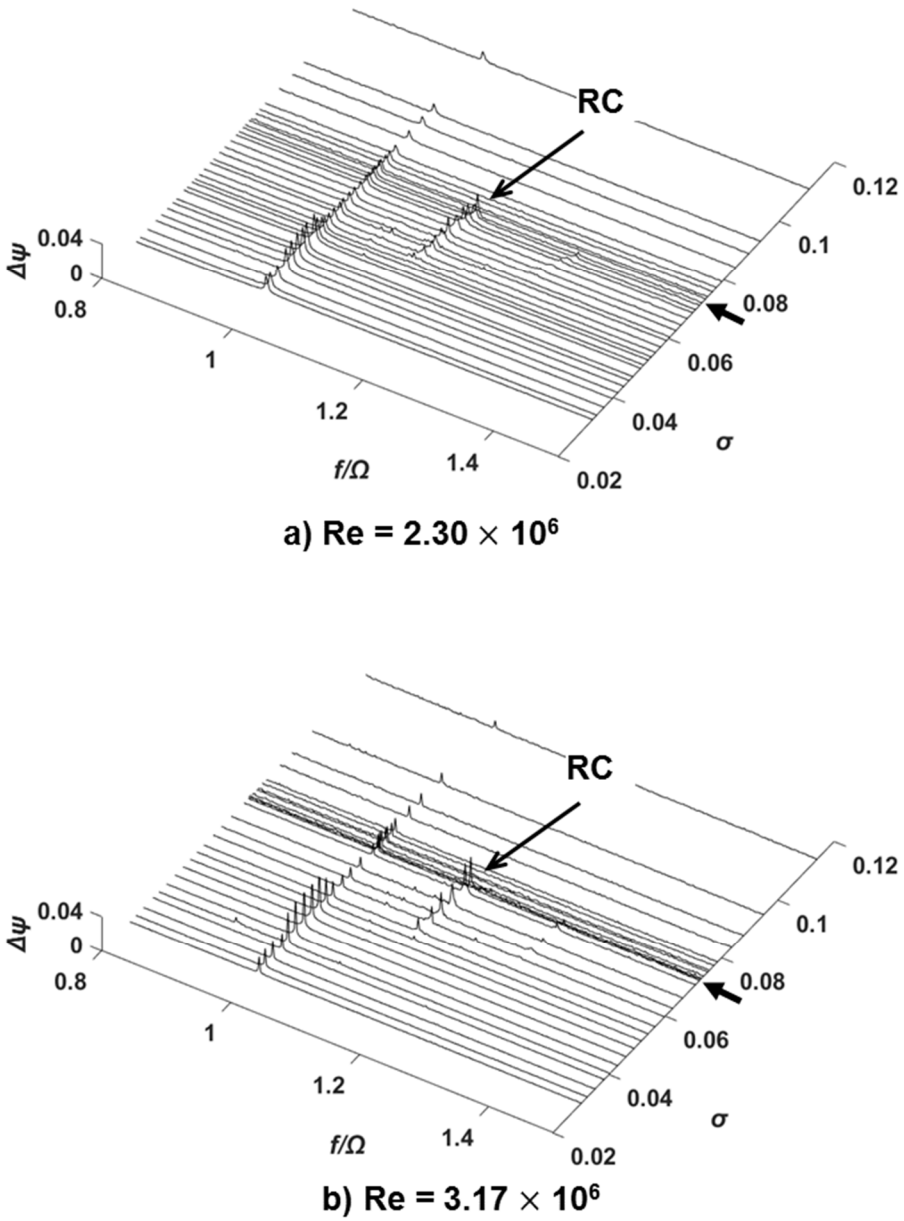

Figure 4.7 The power spectral density plots of unsteady pressure fluctuations at Σ^*=0.0125 and ϕ/ϕ_d=1.0 for Re=2.30×10^6 (a) and Re=3.17×10^6 (b).

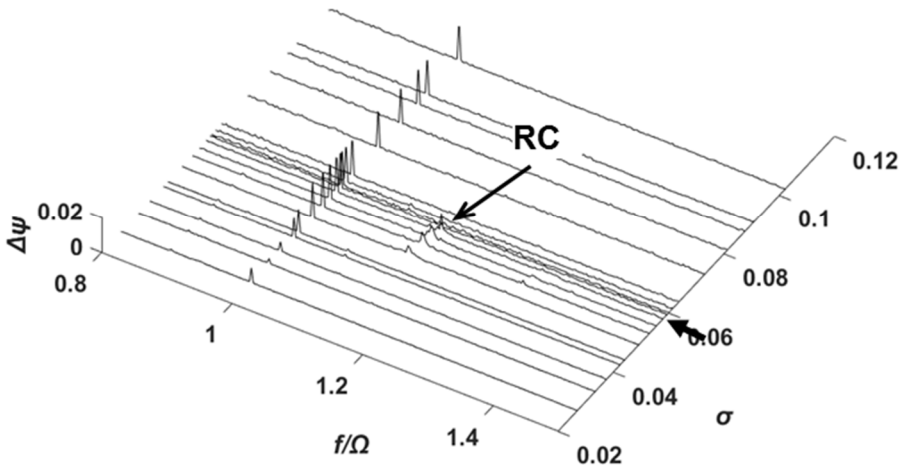

a) Re = 4.81 × 10⁶

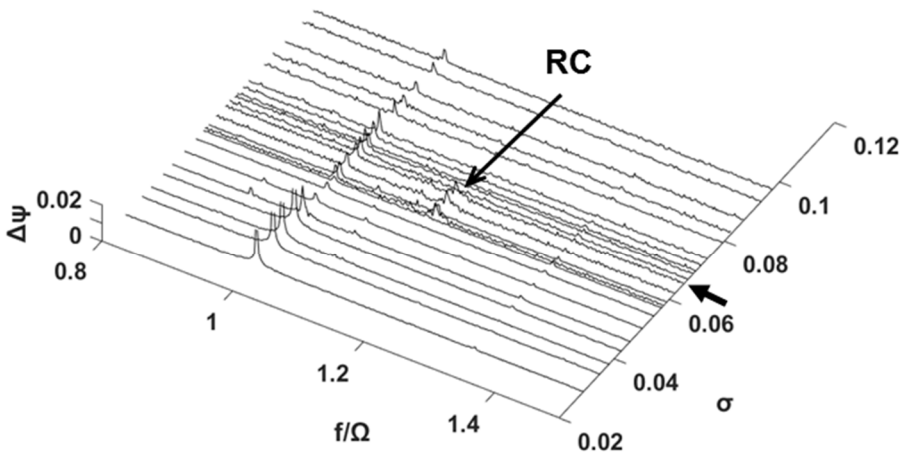

b) Re = 6.84 × 10⁶

Figure 4.8 The power spectral density plots of unsteady pressure fluctuations at Σ^*=1.26 and ϕ/ϕ_d=1.0 for Re=4.81×10^6 (a) and Re=6.84×10^6 (b).

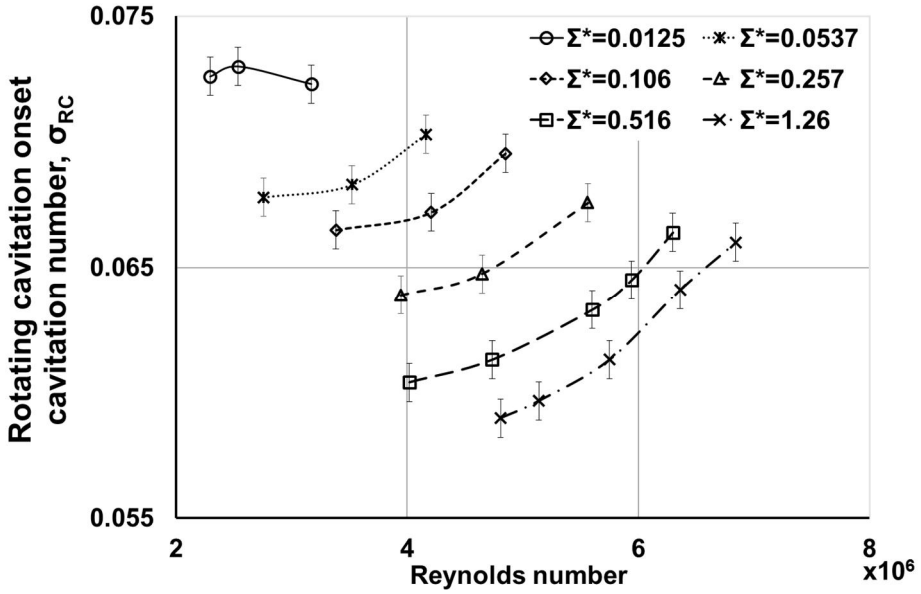

Figure 4.9 The rotating cavitation onset cavitation number and the critical cavitation number for varying Reynolds numbers and Σ^* at ϕ/ϕ_d=1.0.

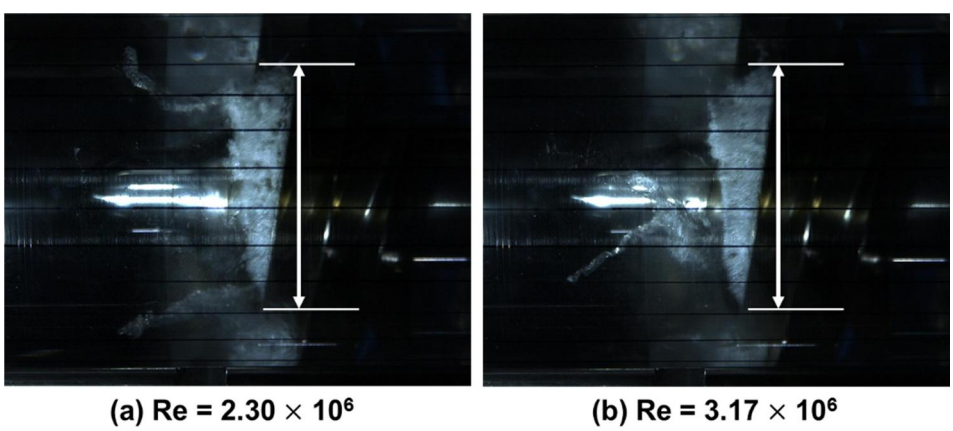

Figure 4.10 The tip leakage vortex cavitation at the inducer blade for Re=2.30×10^6 (a) and 3.17×10^6 (b) (σ=0.081, ϕ/ϕ_d=1.0, Σ^* =0.0125).

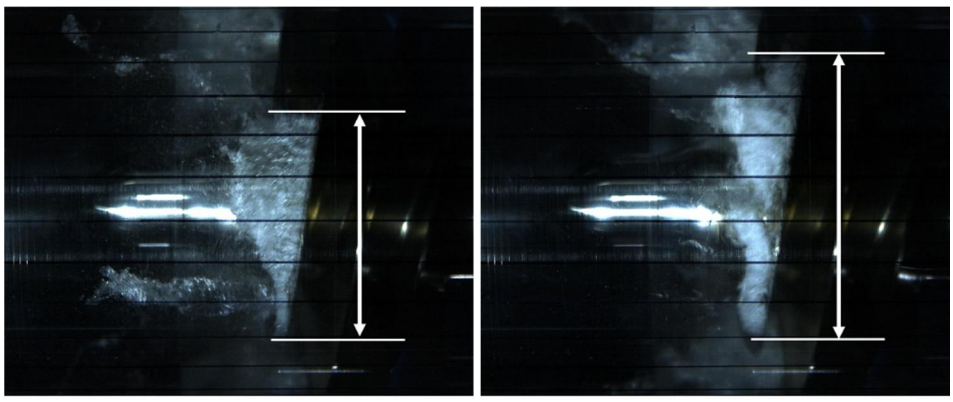

Figure 4.11 The tip leakage vortex cavitation at the inducer blade for Re=4.81×106 (a) and 6.84×106 (b) (σ =0.089, ϕ/ϕ_d=1.0, Σ^*=1.26).

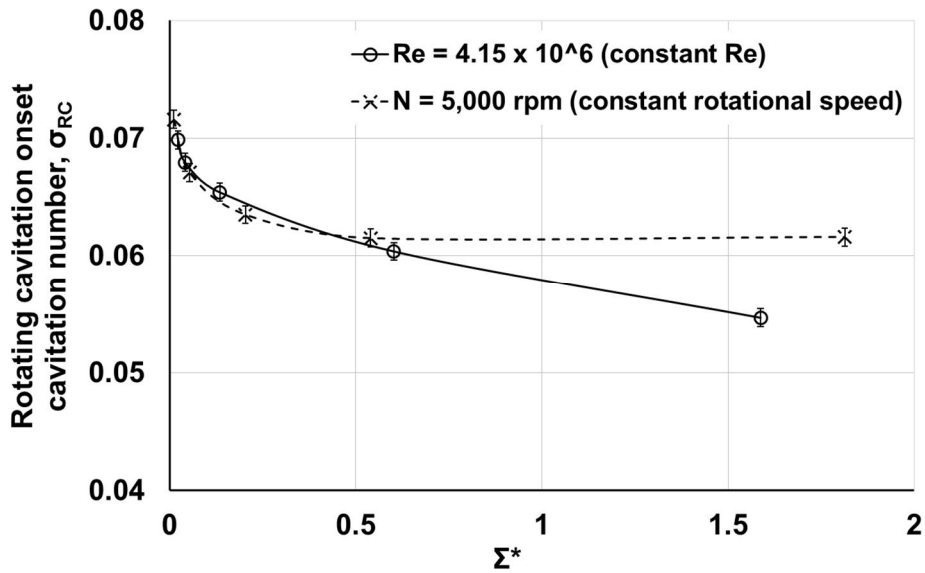

Figure 4.12 The rotating cavitation onset cavitation number versus the non-dimensional thermal parameter for constant Reynolds number and rotational speed at ϕ/ϕ_d=1.0.

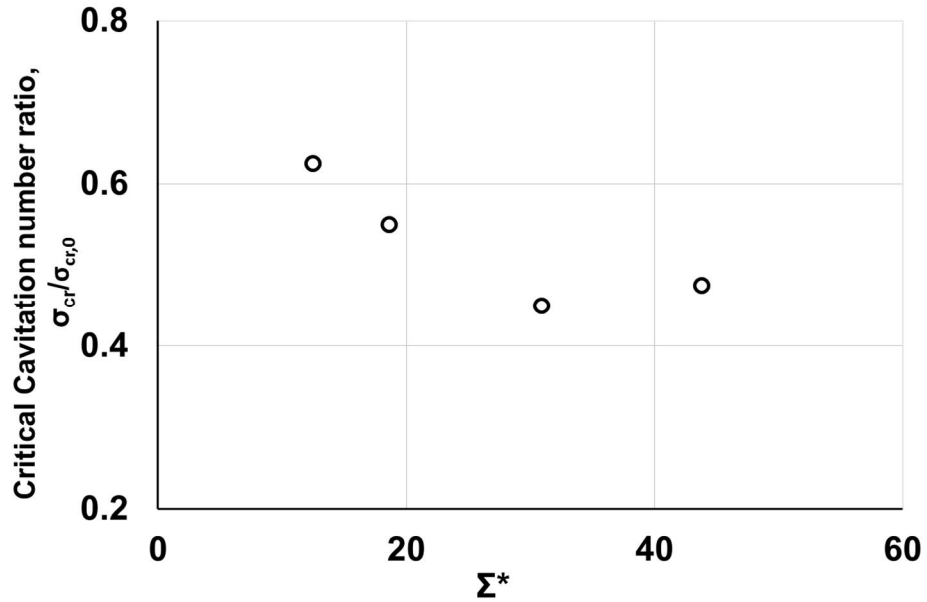

Figure 4.13 The critical cavitation number trends versus Σ^* (re-drawn from [58]).

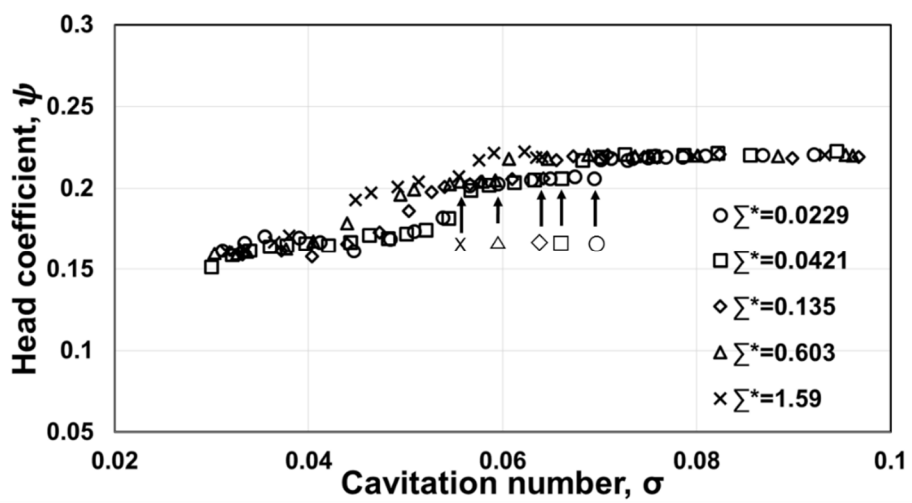

Figure 4.14 Cavitation performance of various non-dimensional thermal parameters at Re=4.15×10^6 (ϕ/ϕ_d=1.0).

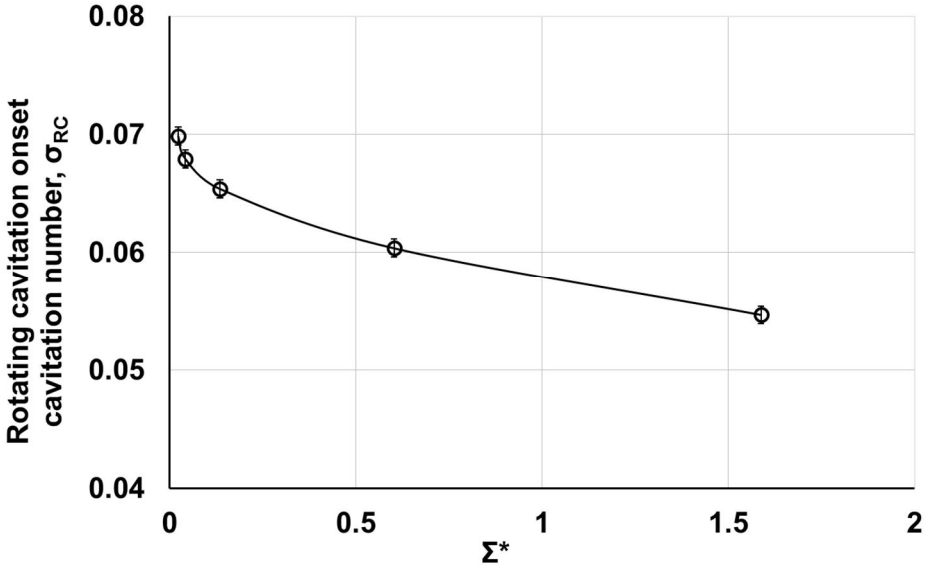

Figure 4.15 The critical cavitation number versus the non-dimensional thermal parameter comparing at Re=4.15×10^6 and ϕ/ϕ_d=1.0.

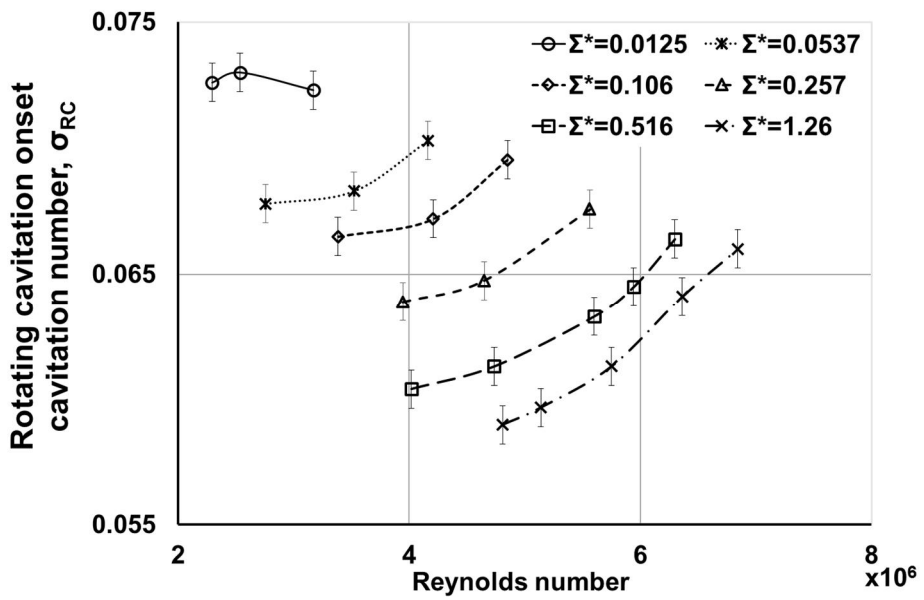

Figure 4.16 The critical cavitation number for varying Reynolds numbers and Σ^* at ϕ/ϕ_d=1.0.

Table 4.1 Test conditions for temperature effects tests.

	Temperature [K]	Rotational speed [rpm]	Σ [$m/s^{3/2}$]	$\Sigma^* = \Sigma\sqrt{C/U^3}$
Water	298	5,000	6.55	1.16×10^{-2}
	313	5,000	3.03×10^{1}	5.39×10^{-2}
	328	5,000	1.14×10^{2}	2.04×10^{-1}
	340	5,000	3.03×10^{2}	5.40×10^{-1}
	357	5,000	1.01×10^{3}	1.80
LOX	87	20,000	8.15×10^{3}	1.81

Table 4.2 Test conditions for thermal parameter effects tests.

	Temperature [K]	Rotational speed [rpm]	Reynolds number	Σ^*
Water	308	6,400	4.14×10^{6}	2.29×10^{-2}
	313	6,000	4.18×10^{6}	4.21×10^{-1}
	323	5,000	4.18×10^{6}	1.35×10^{-1}
	337	4,000	4.13×10^{6}	6.03×10^{-1}
	347	3,500	4.13×10^{6}	1.59
LOX	86.6	20,000	5.04×10^{7}	1.82

Table 4.3 Test conditions for Reynolds number effects tests.

Temperature [K]	Rotational speed [rpm]	Reynolds number	Σ^*
297	4,500	2.30×10^6	1.29×10^{-2}
298	4,900	2.50×10^6	1.22×10^{-2}
300.5	5,800	3.17×10^6	1.23×10^{-2}
310	4,150	2.76×10^6	5.33×10^{-2}
315	5,000	3.52×10^6	5.38×10^{-2}
318	5,700	4.16×10^6	5.42×10^{-2}
318	4,400	3.38×10^6	1.04×10^{-1}
321	5,200	4.21×10^6	1.06×10^{-1}
323	5,800	4.85×10^6	1.08×10^{-1}
328	4,350	3.95×10^6	2.57×10^{-1}
330.5	4,950	4.65×10^6	2.57×10^{-1}
333	4,700	5.56×10^6	2.57×10^{-1}
335	4,000	4.02×10^6	5.15×10^{-1}
337.5	5,550	4.74×10^6	5.18×10^{-1}
340	5,200	5.60×10^6	5.16×10^{-1}
341	5,450	5.94×10^6	5.16×10^{-1}
342	5,700	6.30×10^6	5.20×10^{-1}
346.5	4,100	4.81×10^6	1.22
348	4,300	5.14×10^6	1.26
350	4,700	5.75×10^6	1.26
351.5	5,100	6.36×10^6	1.26
353	5,400	6.84×10^6	1.27

Chapter 5. Summary and Conclusions

5.1. Summary

The present study focuses on rotating cavitation, one of the cavitation instabilities in a turbopump inducer. The objectives of this study are to investigate cause and mechanism of rotating cavitation and thermal effects on rotating cavitation onset experimentally.

To this end, a test facility for inducer water test has been designed and constructed in Seoul National University. Components and instrumentation have been selected based on the research objectives and rotordynamic analysis has been performed to confirm the safety. Non-cavitating suction performance and cavitation performance have been acquired. Using the unsteady pressure measurement and visualization, cavitation instabilities have been identified.

PIV measurement have been carried out to understand rotating cavitation experimentally. It is the first experiment to measure the flow field under rotating cavitation. Based on the incidence angle measurement, the cause and pulsation mechanism of rotating cavitation are explained and numerical simulations from Kang et al. [40] and Tani et al. [41] have confirmed the present results.

From a practical point of view, thermal effects on rotating cavitation onset has been experimentally investigated. Two non-dimensional parameters have been first proposed: non-dimensional thermal parameter (Σ^*) and Reynolds number (Re). The individual

effects of Σ^* and Reynolds number have been measured.

5.2. Conclusions

The main conclusions of this study are as follows.

Rotating Cavitation Mechanism

(1) Without rotating cavitation, tip leakage vortex cavitation region does not grow enough to change the flow field. The incidence angle at the inducer blade is positive and the variation is small.

(2) Rotating cavitation occurs when the tip leakage vortex cavitation region increases enough to reduce the following blade incidence angle to negative values.

(3) The large tip leakage vortex cavitation region influences the flow field of the following blade leading edge and reduces the incidence angle of the following blade to $-4.38°$. On the other hand, the small tip leakage vortex cavitation region does not affect the next blade leading edge and recovers the incidence angle to no-rotating cavitation conditions.

(4) The closure region of the tip leakage vortex cavitation increases the axial velocity and decreases the relative tangential velocity, therefore, the incidence angle of the next blade becomes negative values.

(5) The closure region of the tip leakage vortex cavitation

introduces the negative vortex core. It leads to the negative velocity divergence near the following blade leading edge acting as a sink. Therefore, the flow sucks to the negative divergence region increasing the axial and absolute tangential velocity near the leading edge of the following blade.

(6) The large tip leakage vortex cavitation region suppresses the cavitation region of the next blade, and the small tip leakage vortex cavitation region promotes the cavitation region of the next blade from visualization.

(7) Based on the suppression and growth mechanism of the tip leakage vortex cavitation, the cavitation region at each blade pulsates sequentially with sub-synchronous frequency. Thus, the measured frequency of rotating cavitation is super-synchronous and uneven cavitation region seems to propagate forward. This mechanism has been proposed from the 3-D RANS simulation [[40], [41]] and is confirmed by experiments from this study.

Thermal Effects on Rotating Cavitation Onset

(1) The value of Σ^* in the cryogenic conditions under LOX operation can be achieved in water tests through matching the water temperature and rotational speeds.

(2) When the rotational speed is fixed at 5,000 rpm and temperature is increased, the onset cavitation number decreased as Σ^* was increased for $\Sigma^* < 0.54$. However, for $\Sigma^* \geq 0.54$, the onset cavitation number remained constant as Σ^* was increased.

(3) From the non-dimensionalization process of Rayleigh-Plesset equation, Σ^* and Reynolds number are derived as non-dimensional parameters which affects the cavitation bubble growth.

(4) Increasing Σ^* at constant Reynolds number (Re) inhibits rotating cavitation onset.

(5) Rotating cavitation onset cavitation number (σRC) increases as the Reynolds number is increased for Σ^* higher than 0.0537. For Σ^* lower than 0.0125, the rotating cavitation onset is independent of the Reynolds number.

(6) Increasing Σ^* suppresses the rotating cavitation onset enhancing hydrodynamic stability of the inducer. Conversely, increasing Reynolds number promotes the rotating cavitation onset inducing the hydrodynamic instability.

(7) In perspective of cavitation performance, the critical cavitation number corresponds to the rotating cavitation onset for the casing with the enlargement step. This corresponding is independent of changes in temperature, rotational speed, and non-dimensional parameters.

(8) Consideration of non-dimensional thermal parameter (Σ^*) alone is insufficient to explain cavitation instability onset. In addition, Reynolds number (Re) has to be considered in the design process of turbopumps.

5.3. Recommended Future Works

Based on this research, several areas have been identified as important avenues for further investigations as follows.

(1) When cavitation number further decreases to lower than the rotating cavitation occurrence, asymmetric attached cavitation occurs. The cause and mechanism of the asymmetric attached cavitation and transition region between rotating cavitation and asymmetric attached cavitation have not been investigated. Asymmetric attached cavitation brings strong shaft vibration. Thus, it is important to investigate its cause and mechanism.

(2) For the upstream enlargement ramp casing, the rotating cavitation onset corresponds to the critical cavitation number. On the other hand, for the casing without the ramp, the rotating cavitation onset cavitation number is slightly higher than the critical cavitation number. The relation between cavitation performance and cavitation instability needs to be clarified.

(3) The flow coefficient effects on the onset of rotating cavitation has not been fully understood. Rotating cavitation does not occur when the flow coefficient is lower than the design flow coefficient. And the onset cavitation number of rotating cavitation increases as flow coefficient increases when the flow coefficient is higher than the design flow coefficient. If the flow coefficient is further increases to the 1.2 times of the design flow coefficient, the

author expects that rotating cavitation will be disappeared. Thus, the relation between the flow coefficient and the onset of rotating cavitation needs to be clarified.

(4) To understand POGO instability, the dynamics of cavitaitng inducer are required to be measured such as the mass flow gain factor (M) and cavitation compliance (K). However, measurement of cavitation volume variation is difficult. If visualization of cavitating inducer is performed using many high speed cameras at different angles simultaneously, the cavitation length at each blade can be acquired at the same time. From these measurement, the mass flow gain factor and cavitation compliance can be obtained. It will help to understand the dynamics of cavitating inducer and analysis of POGO instability.

(5) The tip leakage vortex cavitation is important in cavitation instabilities. However, the experimental or numerical investigations on tip leakage vortex cavitation and its effects on flow field has not been fully understood. It will be interesting to study the tip leakage vortex cavitation through experimental method including PIV measurements or numerical method in perspective of basic research.

Bibliography

[1] Florida turbine technology, Inc., http://www.fttinc.com/

[2] Plesset, M., and Prosperetti, A., 1977. "Bubble Dynamics and Cavitation. Journal of Fluid Mechanics", Vol. 9, pp. 145-185.

[3] Franc, J. P., 2006, Physics and Control of Cavitation, In design and Analysis of High Speed Pumps, Educational Notes, pp. 2-1 ~ 2-36.

[4] Brennen, C. E., 2013, *Cavitation and bubble dynamics*. Cambridge University Press.

[5] Franc, J. P., & Michel, J. M., 2006, *Fundamentals of cavitation* (Vol. 76), Springer Science & Business Media.

[6] Franc. J. P., Boitel, G., Riondet, M., Jason, E., Ramina, P., and Rebattet, C., 2010, "Thermodynamic Effect on a Cavitating Inducer-Part 1: Geometrical Similarity of Leading Edge Cavities and Cavitation Instabilities," Journal of Fluids Engineering, Vol. 132, p. 021303.

[7] Cavitating propeller in a water tunnel experiment at the David Taylor Model Basin, http://web.archive.org/web/20080205155941/http://www.dt.navy.mil/div/about/galleries/gallery4/095.html.

[8] Avellan, F., 2004, "Introduction to cavitation in hydraulic machinery," The 6th international conf. on Hydraulic Machinery and Hydrodynamics Timisoara, Romania, October, pp. 11-22.

[9] Shi, L., Zhang, D., Zhao, R., Shi, W., & BPM, B. V., 2017, "Visualized observations of trajectory and dynamics of unsteady tip cloud cavitating vortices in axial flow

pump," Journal of Fluid Science and Technology, 12 (1), JFST0007-JFST0007.

[10] Tan, David, Yuanchao Li, Ian Wilkes, Elena Vagnoni, Rinaldo L Miorini, and Joseph Katz, 2015, "Experimental Investigation of the Role of Large Scale Cavitating Vortical Structures in Performance Breakdown of an Axial Waterjet Pump," *Journal of Fluids Engineering* 137 (11), p. 111301.

[11] Brennen, C. E., 1994, *Hydrodynamics of Pumps*, Concepts ETI, Inc. and Oxford University Press.

[12] Fujii, A., Azuma, S., Uchiumi, M., Yoshida, Y., Tsujimoto, Y., 2003, "Unsteady Behavior of Asymmetric Cavitation in a 3-Bladed Inducer," Fifth International Symposium on Cavitation, Japan, Osaka.

[13] Longley, J. P., 1994, "A review of nonsteady flow models for compressor stability," Journal of Turbomachinery, Vol. 116, 202-213.

[14] Lee, K. H., Choi, J. W., & Kang, S. H., 2012, "Cavitation performance and instability of a two-bladed inducer," Journal of Propulsion and Power, Vol. 28 (6), pp. 1168-1175.

[15] Greitzer, E. M., 1976, "Surge and rotating stall in axial flow compressors—Part I: Theoretical compression system model," Journal of Engineering for Power, Vol. 98 (2), pp. 190-198.

[16] Fujii, A., Azuma, S., Yoshida, Y., Tsujimoto, Y., Horiguchi, H., and Watanabe, S., 2004, "Higher Order Rotating Cavitation in an Inducer," International Journal of Rotating Machinery, 10(4), pp.241-251.

[17] Tsujimoto, Y., and Semenov, A. Y., 2002, "New Types of Cavitation Instabilities in Iducers," Proceedings of the 4th

International Conference on Launcher Technology, 3-6 December, Liege, Belgium.

[18] Semenove, Y. A., A. Fujii, and Y. Tsujimoto, 2004, "Rotating Chock in Cavitating Turbopump Inducer", Journal of Fluids Engineering, Vol. 126, pp. 87~93.

[19] Watanabe, T., D. Kang, A. Cervone, Y. Kawata, and Y. Tsujimoto, 2008, "Choked Surge in a Cavitating Turbopump Inducer," Proceedings of the 7th International Symposium on Cavitation, No.1, pp.64-75.

[20] Ryan, R. S., 1994, "The Space Shuttle Main Engine Liquid Oxygen Pump High-Synchronous Vibration Issue, the Problem, the Resolution Approach, the Solution," 30th Joint Propulsion Conference and Exhibit, AIAA Paper 1994-3153.

[21] Goirand, B., Mertiz, A., Joussellin, F., and Rebattet, C., 1992, "Experimental Investigations of Radial Loads Induced by Partial Cavitation with a Liquid Hydrogen Inducer," Proceedings of the 3rd International Conference on Cavitation (ImechE '92), Vol. C453/056, Cambridge, U.K., pp. 263-269.

[22] Kamijo, K., Yoshida, M., and Tsujimoto, Y., 1993, "Hydraulic and Mechanical Performance of LE-7 LOX Pump Inducer," Journal of Propulsion and Power, Vol. 9, No. 6, pp. 819-826.

[23] Sekita, Ryuichi, Atsutaro Watanabe, Kunio Hirata, and Takayuki Imoto, 2011, "Lessons Learned from H-2 Failure and Enhancement of H-2a Project," Acta Astronautica, Vol. 48, no. 5, pp. 431-438.

[24] Kamijo, K., Shimura, T., and Watanabe, M., 1977, "An Experimental Investigation of Cavitating Inducer Instability," ASME paper 77-WA/FE-14.

[25] Tsujimoto, Y., Yoshida, Y., Maekawa, Y., Watanabe, S., and

Hashimoto, T., 1997, “Observations of Oscillating Cavitation of an Inducer,” Journal of Fluids Engineering, Vol. 119, pp. 775-781.

[26] Hashimoto, Tomoyuki, Makoto Yoshida, and Mitsuo Watanabe., 1997, "Experimental study on rotating cavitation of rocket propellant pump inducers." Journal of Propulsion and Power, Vol. 13 (4), pp. 488-494.

[27] Choi, Y. D., Kurokawa, J., and Imamura, H., 2007, “Suppression of Cavitation in Inducers by J-Grooves,” Journal of Fluids Engineering, Vol. 129 (1), pp. 15-22.

[28] Shimiya, N., Fujii, A., Horiguchi, H., Uchiumi, M., Kurokawa, J., and Tsujimoto, Y., 2008, “Suppression of Cavitation Instabilities in an Inducer by J Groove,” Journal of Fluids Engineering, Vol. 130, p. 021302.

[29] Kang, D., Arimoto, Y., Yonezawa, K., Horiguchi, H., Kawata, Y., Hah, C., and Tsujimoto, Y., 2010, “Suppression of cavitation instabilities in an inducer by circumferential groove and explanation of higher frequency components.” International Journal of Fluid Machinery and Systems, Vol. 3, p. 137-149.

[30] Lettieri, C., Spakovszky, Z., Jackson, D., & Schwille, J., 2017, “Characterization of Cavitation Instabilities in a Four-Bladed Turbopump Inducer,” Journal of Propulsion and Power, 1-11.

[31] Tsujimoto, Y., Kamijo, K., and Y. Yoshida, 1993, “A Theoretical Analysis of Rotating Cavitation in Inducers”, Journal of Fluids Engineering, Vol. 115, pp. 135-141.

[32] Tsujimoto, Y., Kamijo, K., Brennen, C. E., 2001, “Unified Treatment of Flow Instabilities of Turbomachines,” Journal of Propulsion and Power, Vol. 17 (3), pp. 636-643.

[33] Watanabe, S., Sato, K., Tsujimoto, Y., Kamijo, K., 1999,

"Analysis of Rotating Cavitation in a Finite Pitch Cascade Using a Closed Cavity Model and a Singularity Method," Journal of Fluids Engineering, Vol. 121, pp. 834-840.

[34] Horiguchi, H., Watanabe, S., Tsujimoto, Y., 2000, "A Linear Stability Analysis of Cavitation in a Finite Blade Count Impeller," Journal of Fluids Engineering, Vol. 122, No. 4, pp. 798-805.

[35] Iga, Y., Nohml, M., Goto, A., Shin, B. R., and Ikohagi, T., "Numerical Study of Sheet Cavitation Breakoff Phenomenon on a Cascade Hydrofoil," Journal of Fluids Engineering, Vol. 125, pp. 643-651.

[36] Iga, Y., Nohml, M., Goto, A., Ikohagi, T., 2004, "Numerical Analysis of Cavitation Instabilities Arising in the Three-Blade Cascade," Journal of Fluids Engineering, Vol. 126, pp. 419-429.

[37] Iga, Y., Yoshida, Y., 2011, "Mechanism of Propagation Direction of Rotating Cavitations in a Cascade," Journal of Propulsion and Power, Vol. 27(3), pp. 675-683.

[38] Kimura, T., Yoshida, Y., Hashimoto, T., Shimagaki, M., 2008, "Numerical Simulation for Vortex Structure in a Turbopump Inducer: Close Relationship with Appearance of Cavitation Instabilities," Journal of Fluids Engineering, Vol. 130, p. 051104.

[39] Hosangadi, A., Ahuja, V., and Ungewitter, R. J., 2007, "Simulations of Rotational Cavitation Instabilities in the SSME LPFT Inducer," 43rd AIAA/ASME/SAE/ASEE Joint Propulsion Conference & Exhibit, Cincinnati, OH, Report No. AIAA 2007-5536.

[40] Kang, D., Yonezawa, K., Horiguchi, H., Kawata, Y., Tsujimoto, Y., 2009, "Cause of cavitation instabilities in three dimensional

inducer," International Journal of Fluid Machinery and Systems, Vol. 2 (3), pp. 206-214.

[41] Tani, N., Yamanishi, N., Tsujimoto, Y., 2012, "Influence of Flow Coefficient and Flow Structure on Rotational Cavitation in Inducer," Journal of Fluids Engineering, Vol. 134, p. 021302.

[42] Rugger, R. S., and Moore, R. D., 1969, "Method for Prediction of Pump Cavitation Performance for Various Liquids, Liquid Temperatures, and Rotative Speeds," NASA Report. TN-5292.

[43] Kikuta, K., Yoshida, Y., Watanabe, M., Hashimoto, T., Nagaura, K., and Ohira, K., 2008, "Thermodynamic Effect on Cavitation Performances and Cavitation Instabilities in an Inducer," Journal of Fluids Engineering, Vol. 130, p. 111302.

[44] Franc. J. P., Jason, E., Morel, P., Rebattet, C., and Riondet, M., 2001, "Visualization of Leading Edge Cavitation in an Inducer at Different Temperatures," Fourth International Symposium on Cavitation, CAV2001, Pasadena, CA, 20-23, June.

[45] Yoshida, Y., Sasao, Okita, K., Hasegawa, S., Shimagaki, M., and Ikohagi, T., 2007, "Influence of Thermodynamic Effect on Synchronous Rotating Cavitation," Journal of Fluids Engineering, Vol. 129, pp. 871-876.

[46] Yoshida, Y., Sasao, Y., Watanabe, M., Hashimoto, T., Iga, Y., and Ikohagi, T., 2009, "Thermodynamic Effect on Rotating Cavitation in an Inducer," Journal of Fluids Engineering, Vol. 131, pp. 091302.

[47] Cervone, A., Testa, R., Bramanti, C., Rapposelli, E., and d' Agostino, L., 2005, "Thermal Effects on Cavitation Instabilities in Helical Inducers," Journal of Propulsion and Power, Vol. 21, pp. 893-899.

[48] Torre, L., Cervone, A., Pasini, A., and d' Agostino, L., 2011,

"Experimental Characterization of Thermal Cavitation Effects on Space Rocket Axial Inducers," Journal of Fluids Engineering, Vol. 133, pp. 111303.

[49] Tokuma, T., Sekino, Y., and Kamijo, K., 2003, "A New Modeling of Sheet Cavitation Considering the Thermodynamic Effects," fifth International Symposium on Cavitation, CAV2003, Osaka, 1-4, November.

[50] Hosangadi, A., and Ahuja, V., 2005, "Numerical Study of Cavitation in Cryogenic Fluids," Journal of Fluids Engineering, Vol. 127, pp. 267-281.

[51] Hosangadi, A., Ahuja, V., Ungewitter, R. J., and Busby, J., 2007, "Analysis of Thermal Effects in Cavitating Liquid Hydrogen Inducers," Journal of Propulsion and Power, Vol. 23(6), pp. 1225-1234.

[52] Gonclaves, E., Patella, R. F., Rolland, J., Pouffary, B., and Challier, G., 2010, "Thermodynamic Effect on a Cavitating Inducer in Liquid Hydrogen," Journal of Fluids Engineering, Vol. 132, pp. 11305.

[53] Stepanoff, A. J., 1964, "Cavitation Properties of Liquids," Journal of Engineering for Gas Turbines and Power, Vol. 86(2), pp. 195-200.

[54] Franc, J. P., Rebattet, C., and Coulon, A., 2004, "An Experimental investigation of Thermal Effect in a Caivtating Inducer," Journal of Fluids Engineering, Vol. 126, pp. 716-723.

[55] Cooper, P., 1967, "Analysis of Single and Two-Phase Flows in Turbopump Inducers," Journal of Engineering for Gas Turbines and Power, Vol. 89(4), pp. 577-586.

[56] Watanabe, S., Hidaka, T., Horiguchi, H., Furukawa, A., and Tsujimoto, Y., 2007, "Analysis of Thermodynamic Effects on

Cavitation Instabilities," Journal of Fluids Engineering, Vol. 129, pp. 1123-1130.

[57] Watanabe, S., Furukawa, A., and Yoshida, Y, 2008. "Theoretical Analysis of Thermodynamic Effect on Cavitation in Cryogenic Inducer Using Singularity Method," International Journal of Rotating Machinery, Vol. 2008, p. 125678.

[58] Kikuta, K., Yoshida, Y., Hashimoto, T., Nanri, H., Mizuno, T., and Shimiya, N, 2009, "Influence of Rotational Speed on Theromdynamic Effect in a Cavitating Inducer," ASME Fluids Engineering Division Summer Meeting, Colorado, USA, 2-6, August.

[59] Ehrlich, D. A., and Murdock, J. W, 2015, "A Dimensionless Scaling Parameter for Thermal Effects on Cavitation in Turbopump Inducers," Journal of Fluids Engineering, Vol. 137, p. 041103.

[60] D. A. Ehrlich, J. A. Schwille, R. P. Welle, J. W. Murdock, and B. S. Hardy, 2009, "A Water Test Facility fo Liquid Rocket Engine Turbopump Cavitation Testing", 7th International Symposium on Cavitation, Paper No. 11.

[61] E. Rapposelli, A. Cervone, and L. d' Agostino, 2002, "A New Cavitating Pump Rotordynamic Test Facility", 38th AIAA/ASME/SAE/ASEE Joint Propulsion Conference and Exhibit.

[62] Cristina Bramanti, "Experimental Study of Cavitation and Flow Instabilities in Space Rocket Turbopumps and Hydrofoils," Ph. D thesis, University of Pisa.

[63] Ito, Y., Kitano, S., Tani, N., 2012, "Nitrogen and Water Cavitation in Rotating Inducer," the 8th International Symposium on Cavitation, Singapore.

[64] Abhijit Bhattacharyya, 1994, “Internal Flows and Force Matrices in Axial Flow Inducers”, Phd. Thesis, California Institute of Technology.

[65] Choi, C., Noh, J., Kim, J., Hong, S., and Kim, J., 2006, “Effects of a Bearing Strut on the Performance of a Turbopump Inducer”, Journal of Propulsion and Power, pp. 1413~1417.

[66] Kalpakjian S., and Schmid, S. R., Manufacturing Processes for Engineering Materials, 5th edition, Pearson Prentice Hall.

[67] Balje, O. E., 1981, *Turbomachines. A guide to design, selection and theory*., John Wiley and Sons, New York.

[68] Ronald H. Aungier, 2000, *Centrifugal Compressors: A strategy for Aerodynamic Design and Analysis,* ASME Press.

[69] A Whitfield, N C Baines, 1990, *Design of radial turbomachines*, Longman Scientific & Technical.

[70] Kang, S. H., and Hong, S. S., 1999, “원심펌프의 회전차 출구 유동에 관한 실험적 연구”, 유체기계 연구개발 발표회 논문집, pp. 234-241. (Korean).

[71] Hugh W. Coleman, W. Glenn Steele, Jr.. 1989, “Experimentation and Uncertainty Analysis for Engineers”, John willey & sons.

[72] Hunt, J. C., Wray, A. A., & Moin, P., 1988, “Eddies, streams, and convergence zones in turbulent flows,” Center for Turbulence Research Report CTR-S88, pp. 193-208.

[73] Dantec Dynamics, https://www.dantecdynamics.com/measurement-principles-of-piv

[74] Dantec Dynamics, Adaptive correlation in DynamicStudio.

[75] Wieneke, B., & Pfeiffer, K., 2010, “Adaptive PIV with variable interrogation window size and shape.” 15th Int Symp on Applications of Laser Techniques to Fluid Mechanics, Lisbon,

Portugal.

[76] Theunissen, R., 2010, *Adaptive image interrogation for PIV: application to compressible flows and interfaces,* PhD Thesis, TU Delft, Delft University of Technology.

[77] Shimagaki, M., Kimura, T., Hashimoto, T., Watanabe, M., and Yoshida, Y., 2007, "Investigation of Backflow Structure in a Turbopump Inducer with the PIV Method," 43rd AIAA/ASME/SAE/ASEE Joint Propulsion Conference & Exhibit, Cincinnati, OH, Report No. AIAA 2007-5512.

[78] Bergman, T. L., and Incropera, F. P, 2011, *Introduction to heat transfer*, John Wiley & Sons, 5th edition.

[79] Tokumasu, T., Sekino, Y., and Kamijo, K., 2005, "The Numerical Analysis of the Effect of Flow Properties on the Thermodynamic Effect of Cavitation," Trans. Japan Society for Aeronautical and Space Science, Vol. 47 (156), pp. 146-152.

[80] Korea Aerospace Research Institute, www.kari.re.kr.

[81] Del Valle, J., Braisted, D. M., and Brennen, C. E., 1992, "The Effects of Inlet Flow Modification on Cavitating Inducer Performance", ASME Journal of Turbomachinery, Vol.114, pp.360~365.

[82] Kang, B. Y. and S. H. Kang, 2014, "Effect of the inlet shape on performance characteristics in a turbopump," 15th International Symposium on Transport Phenomena and Dynamics of Rotating Machinery.

[83] Fujii, A., Azuma, S., Yoshida, Y., Tsujimoto, Y., and Laffite, S., 2002, "Unsteady Stress of 4-Bladed Inducer Blades and the Effect of Inlet Flow Distortion", JSME International Journal, Vol.45 (1), pp.47-54.

[84] 이효성, 2011, "Effects of Large Tip Clearance on Aerodynamic

Performance in a Turbine Cascade," Seoul National University, Master thesis.

Appendix A

Test Facilities in Other Institutes

Aerospace Corporation [60], Pisa University [[61], [62]], Osaka University [[18], [25]], Japan Aerospace Exploration Agency (JAXA) [63], California Institute of Technology (Caltech) [64], and Korea Aerospace Research Institute (KARI) [65] are compared and analyzed to design the test facility in Seoul National University. Aerospace Corporation have built the vertical test facility as shown in Fig. A.1. They employed Helium sparging system for deaeration in water. The test facility in Pisa University (Fig. A.2) was built for the rotordynamic analysis, thus, it has a whirl motor to give the eccentricity of the shaft. Airbag system for pressurization of the test facility was employed to minimize the air contents in the test facility. Osaka University (Fig. A.3) installed the magnetic vibrator to give the oscillation of the flow. California Institute of Technology (Fig. A.4) installed the siren valve to investigate the POGO instability. KARI (Fig. A.5) also has the test facility to test the inducer performance and instability.

Figure A.1 Test facility in Aerospace Corporation.

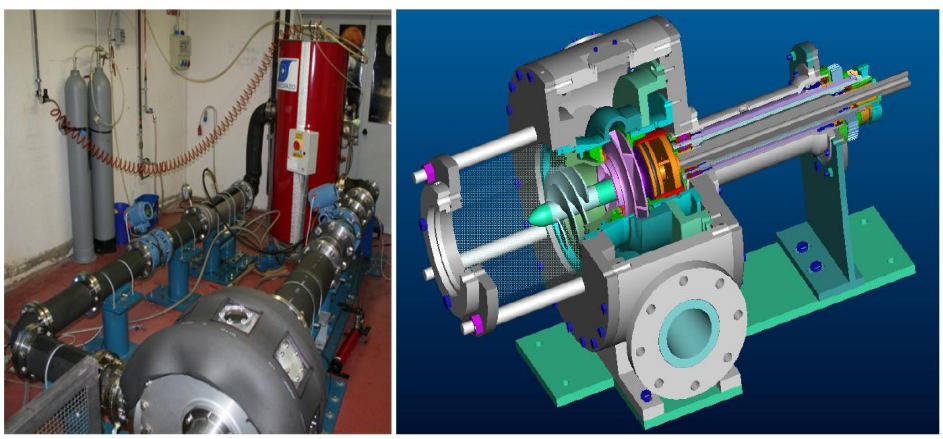

Figure A.2 Test facility in Pisa University.

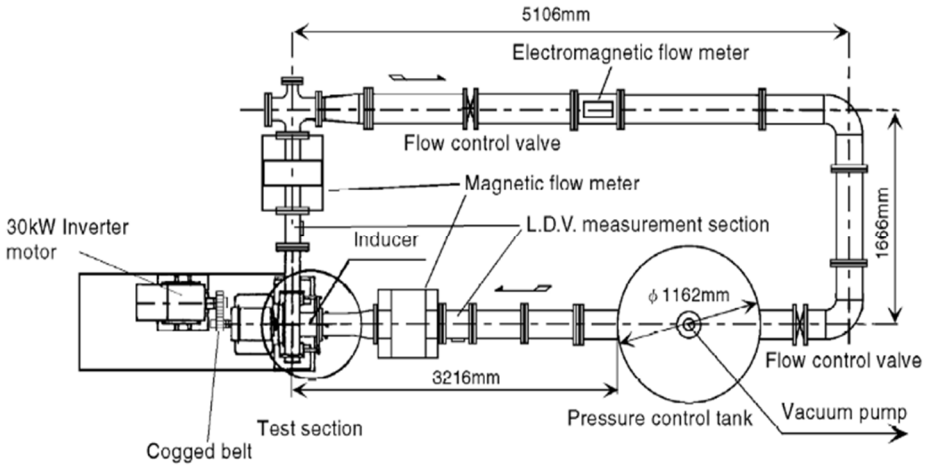

Figure A.3 Test facility in Osaka University.

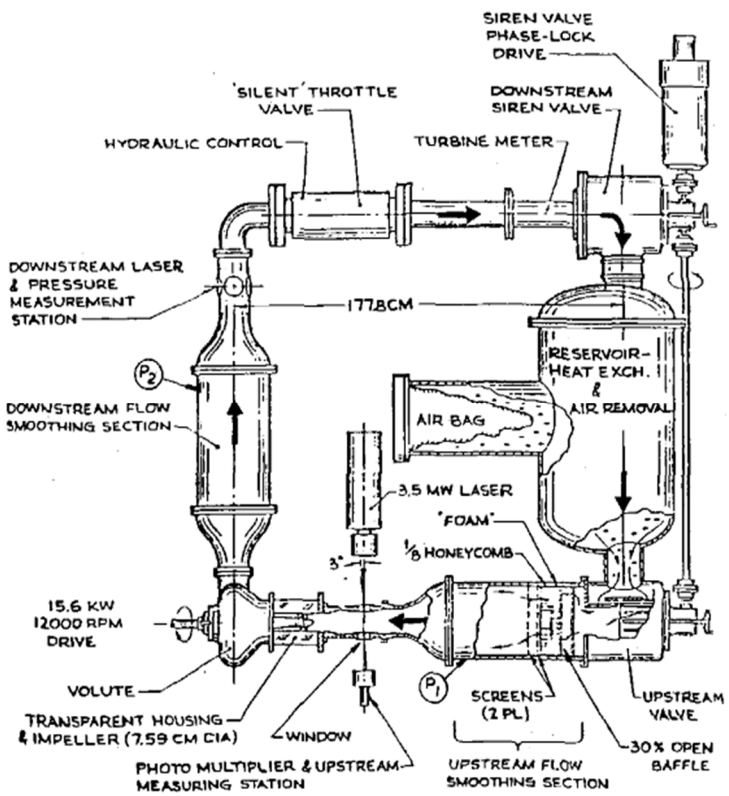

Figure A.4 Test facility in Caltech.

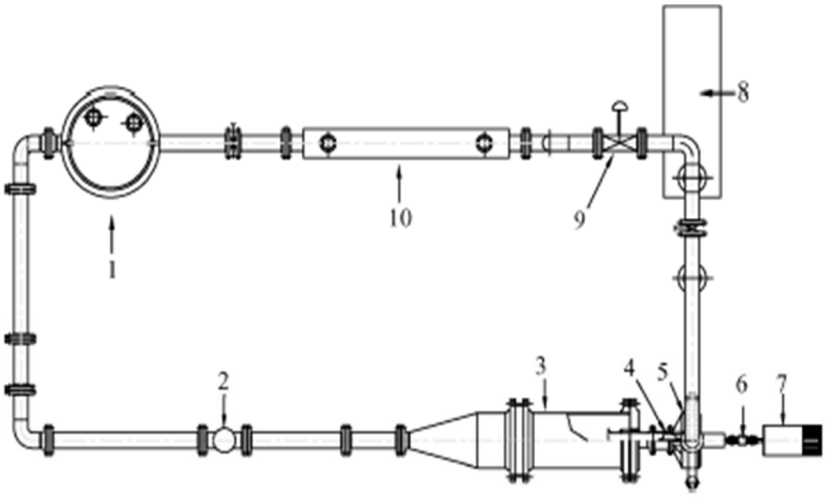

Fig. 1 Plane view of test loop: 1) water tank, 2) turbine flow meter, 3) settling chamber, 4) test inducer, 5) collector, 6) torque meter, 7) motor, 8) booster pump, 9) regulating value, and 10) heat exchanger.

Figure A.5 Test facility in KARI.

Appendix B

Heat Transfer Analysis of the Duct

Following Bergman and Incropera [71], an expression for the heat flux at the inducer inlet can be inferred from the resistance network as shown in Fig. B.1 (h_x is the convection heat transfer coefficient between the water flow and the inner surface of the wall; $R_{t,cond}$ is thermal resistance of cylindrical wall, h_o is natural convection heat transfer coefficient between the duct outer surface and the ambient air, 10 $W/m^2 \cdot K$). The following assumptions have been made.

[1] The flow is steady with constant properties.

[2] Viscous dissipation and pressure variations are negligible.

[3] Convection coefficient at outer surface of the duct is uniform

[4] The heat transfer rate for the duct is expressed as

$$q_s' = \frac{T_m - T_\infty}{[1/2\pi r h_x] + [R_{t,cond}] + [1/2\pi(r+t)h_o]} = \frac{T_m - T_s}{1/(2\pi r h_x)} \quad \text{(B.1)}$$

$$Nu_D = \frac{h_x D}{k} = 0.023 Re_D^{4/5} Pr^{0.3} \quad \text{(B.2)}$$

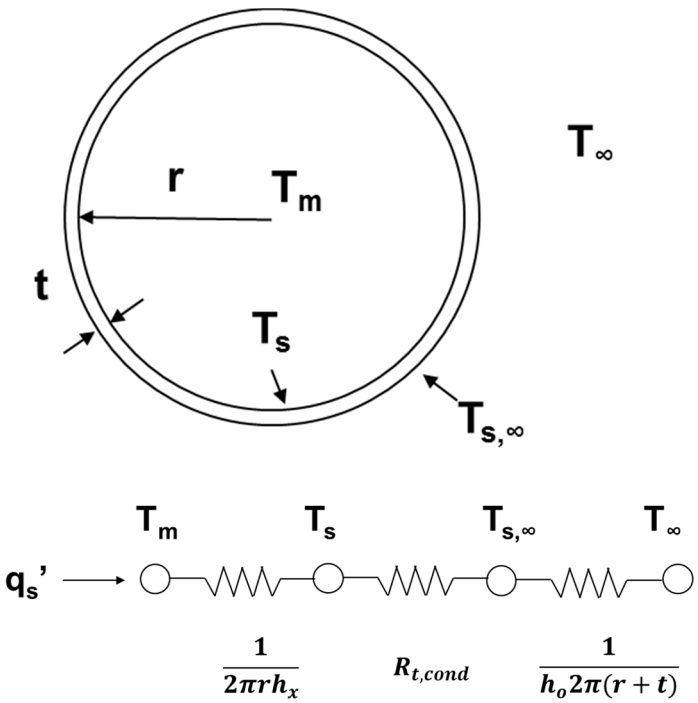

Figure B.1 Heat transfer analysis of the duct at the inducer inlet.

With such assumptions and heat transfer equations, the temperature difference between the bulk flow and flow near the wall ranges from 0.042 K (308 K, 6,400 rpm) to 0.091 K (353 K, 5,400 rpm).

Appendix C

Raw Data of Thermal Effects on Cavitation Performance and Rotating Cavitation Onset

Thermal effects on cavitation performance and rotating cavitation onset have been shown in Chapter 4. In Appendix C, raw experimental data of cavitation performance and power spectrum density from FFT analysis of unsteady pressure transducers for constant non-dimensional thermal parameters at different Reynolds number are shown as follows.

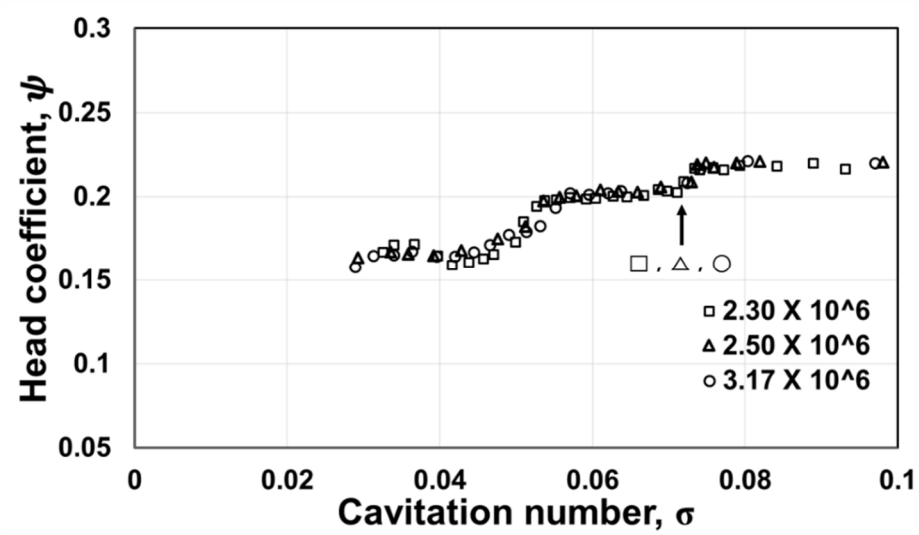

Figure C.1 Cavitation performance of various Reynolds number at Σ^*=0.0125 (ϕ/ϕ_d=1.0).

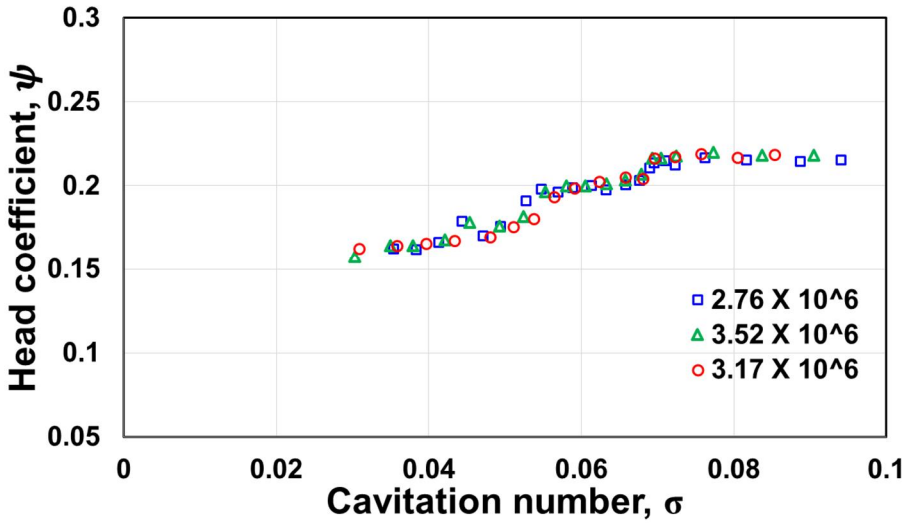

Figure C.2 Cavitation performance of various Reynolds number at Σ^*=0.0537 (ϕ/ϕ_d=1.0).

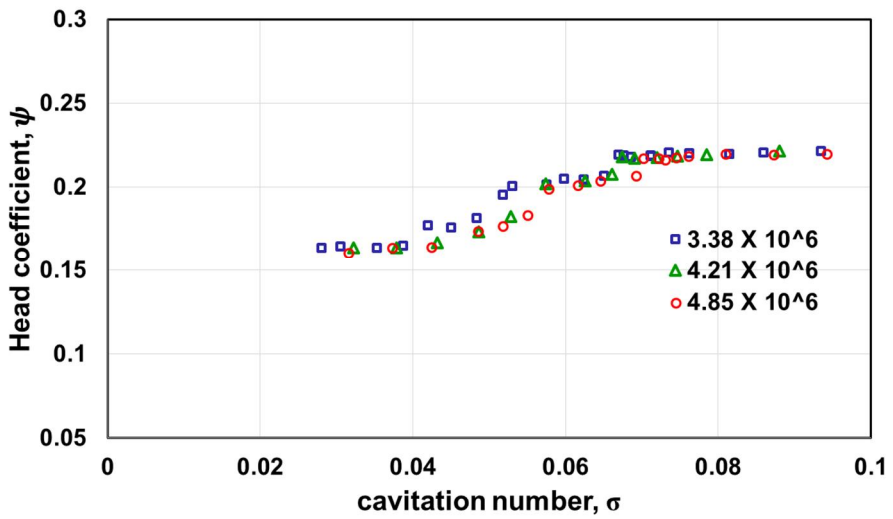

Figure C.3 Cavitation performance of various Reynolds number at Σ^*=0.106 (ϕ/ϕ_d=1.0).

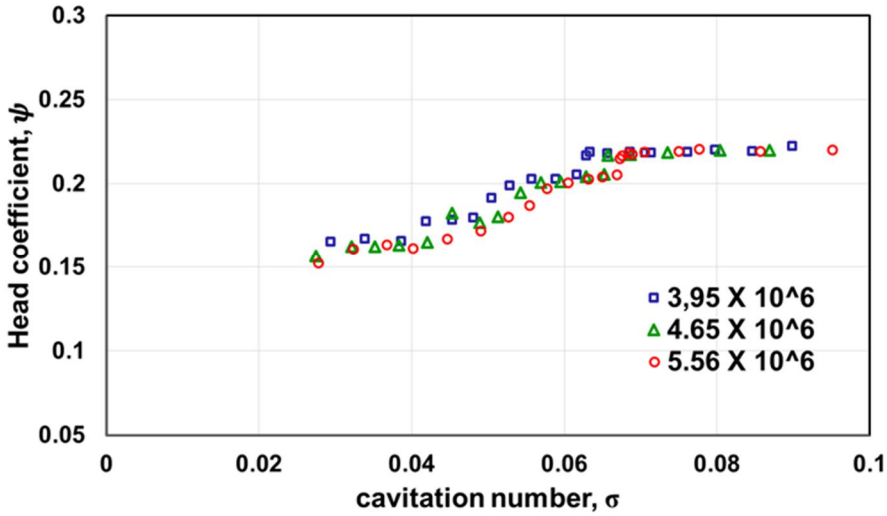

Figure C.4 Cavitation performance of various Reynolds number at Σ^*=0.257 (ϕ/ϕ_d=1.0).

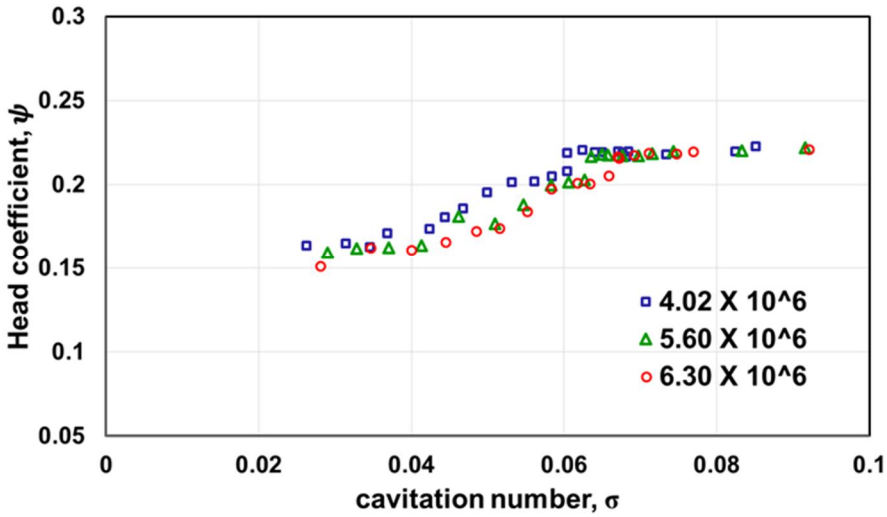

Figure C.5 Cavitation performance of various Reynolds number at Σ^*=0.516 (ϕ/ϕ_d=1.0).

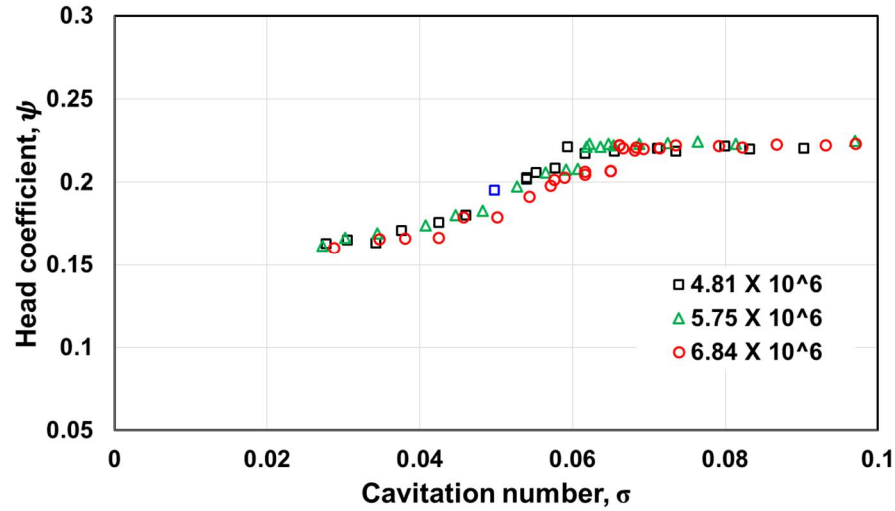

Figure C.6 Cavitation performance of various Reynolds number at $\Sigma^{*}=1.28$ ($\phi/\phi_d=1.0$).

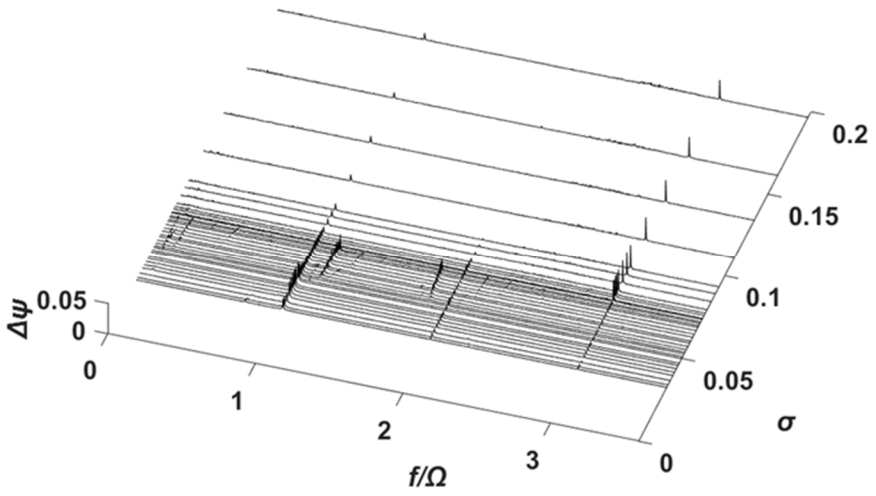

a) Re = 2.30 × 10⁶

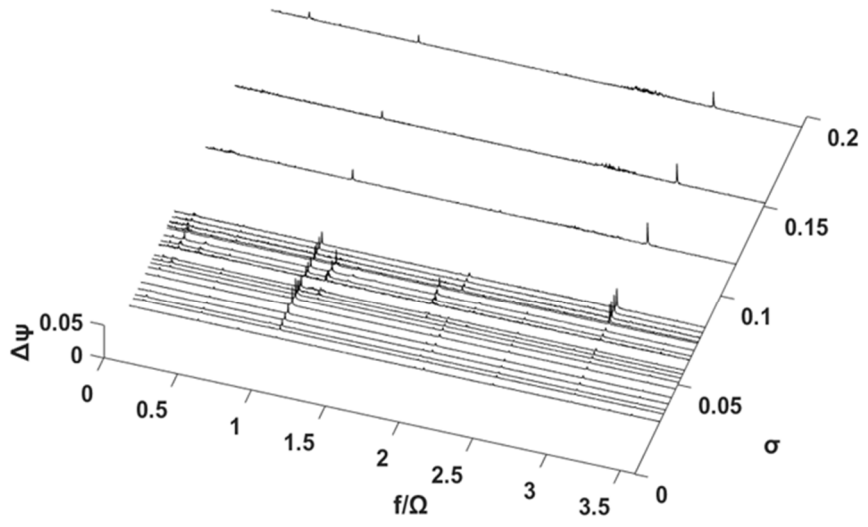

b) Re = 2.50 × 10^6

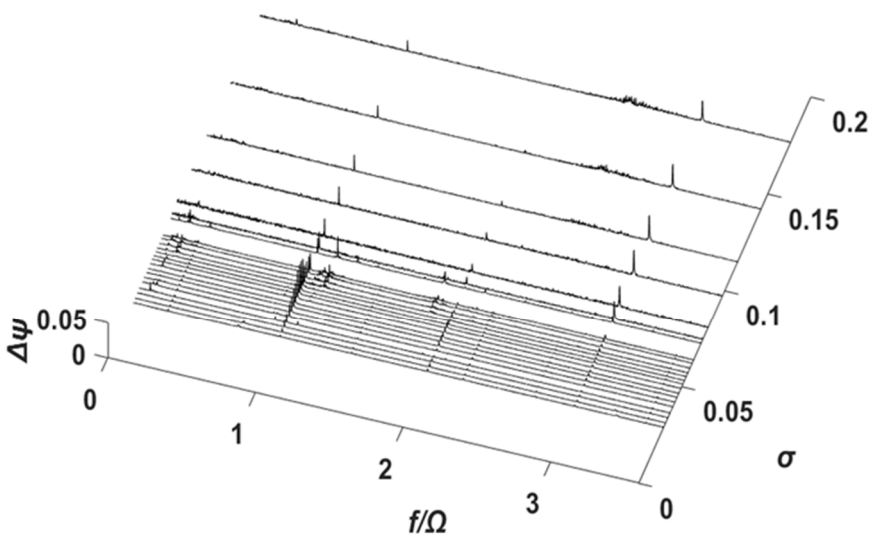

c) Re = 3.17 × 10^6

Figure C.7 The power spectral density plots of unsteady pressure

fluctuations at Σ^*=0.0125 and ϕ/ϕ_d=1.0 for Re=2.30×10^6 (a), Re=2.50×10^6 (b), and Re=3.17×10^6 (c).

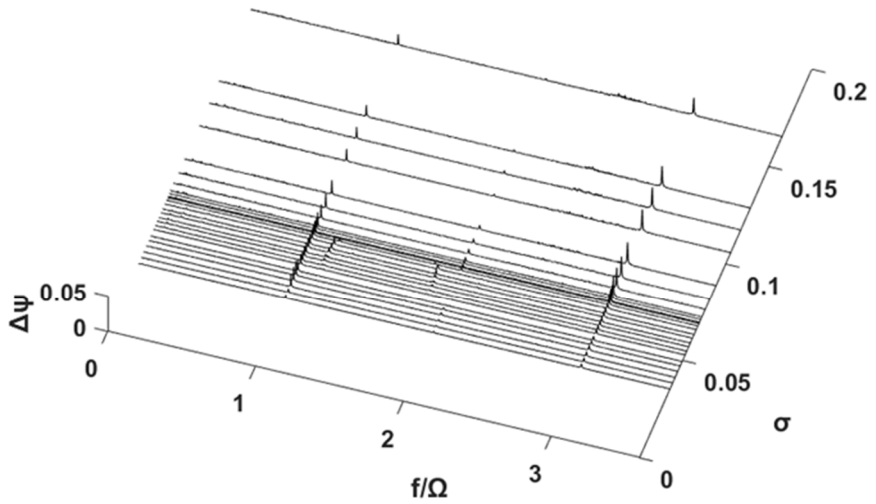

a) Re = 2.76 × 10^6

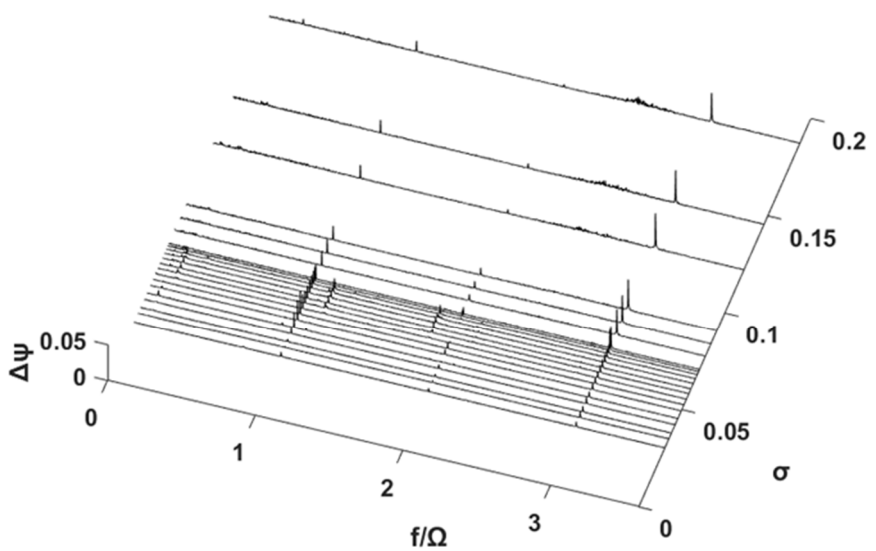

b) Re = 3.52 × 10^6

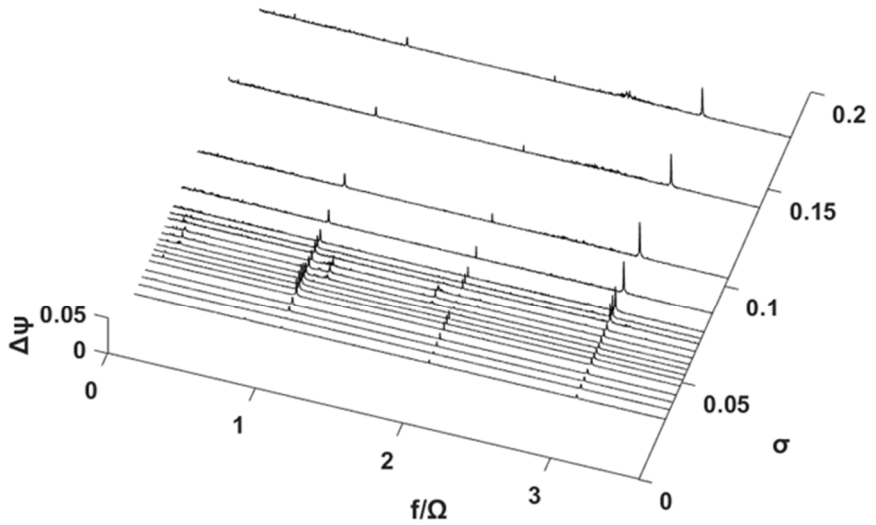

Figure C.8 The power spectral density plots of unsteady pressure fluctuations at Σ^*=0.0537 and ϕ/ϕ_d=1.0 for Re=2.76×10^6 (a), Re=3.52×10^6 (b), and Re=4.16×10^6 (c).

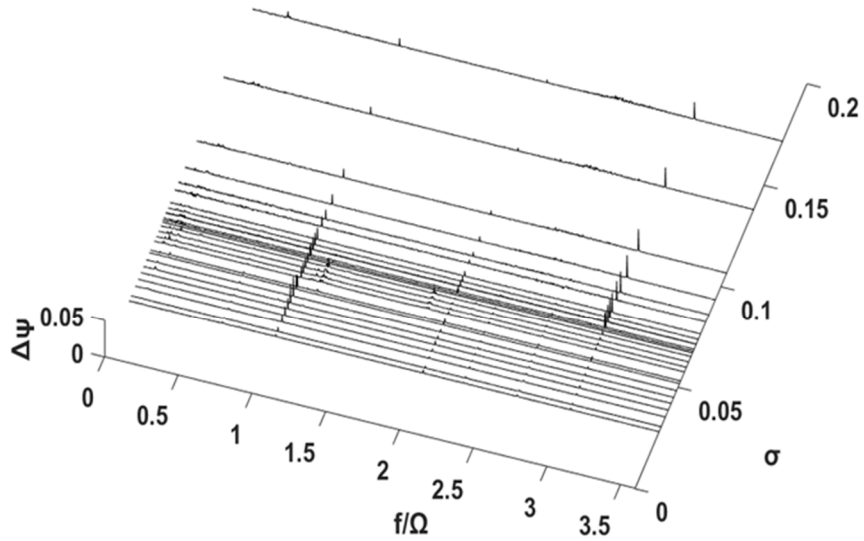

a) Re = 3.38 × 10^6

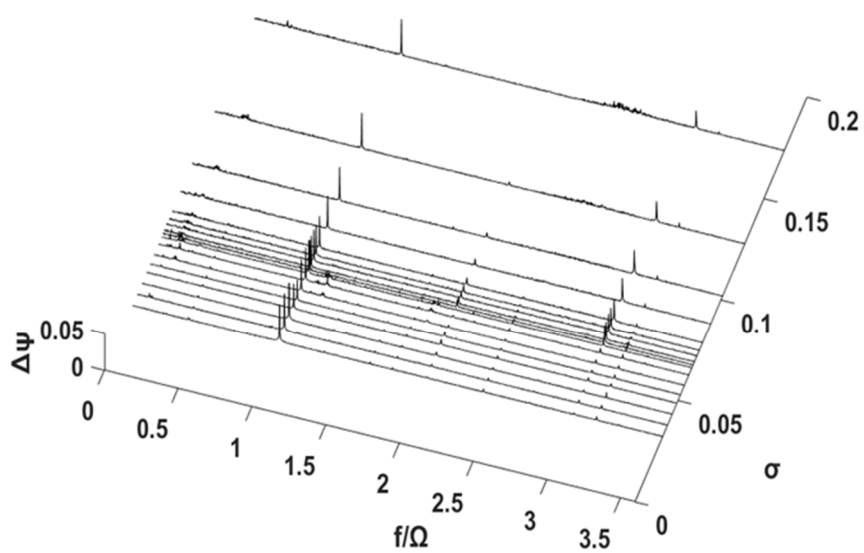

b) Re = 4.21 × 10^6

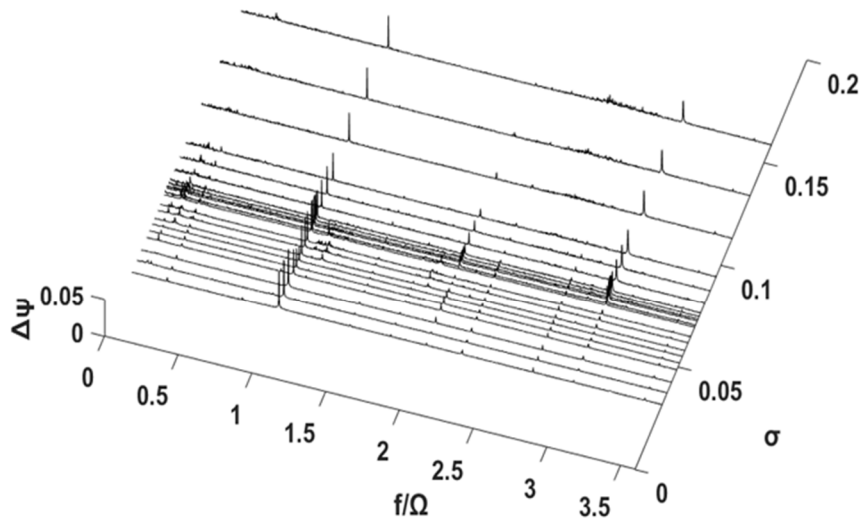

c) Re = 4.85 × 10⁶

Figure C.9 The power spectral density plots of unsteady pressure fluctuations at Σ^*=0.106 and ϕ/ϕ_d=1.0 for Re=3.28×10^6 (a), Re=4.21×10^6 (b), and Re=4.85×10^6 (c).

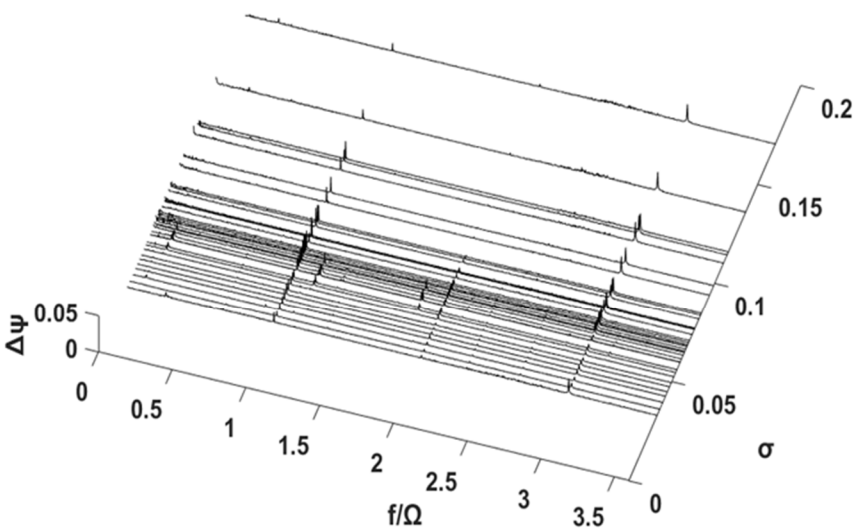

a) Re = 3.95 × 10⁶

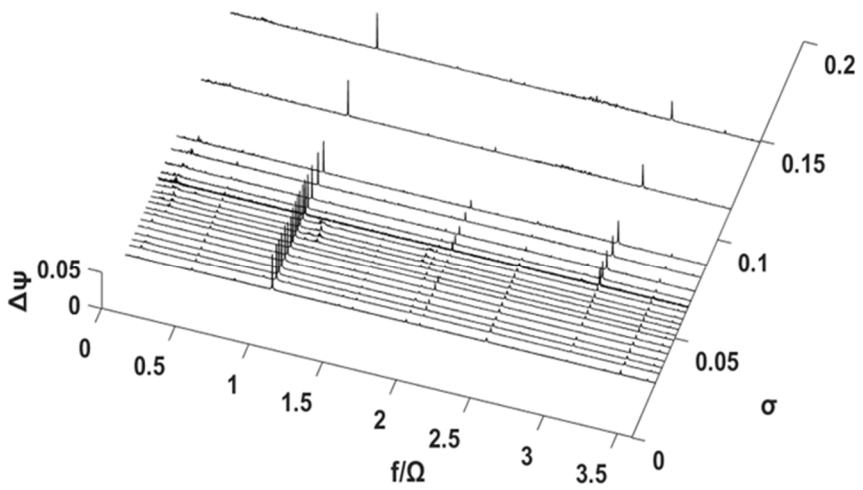

b) Re = 4.65 × 10^6

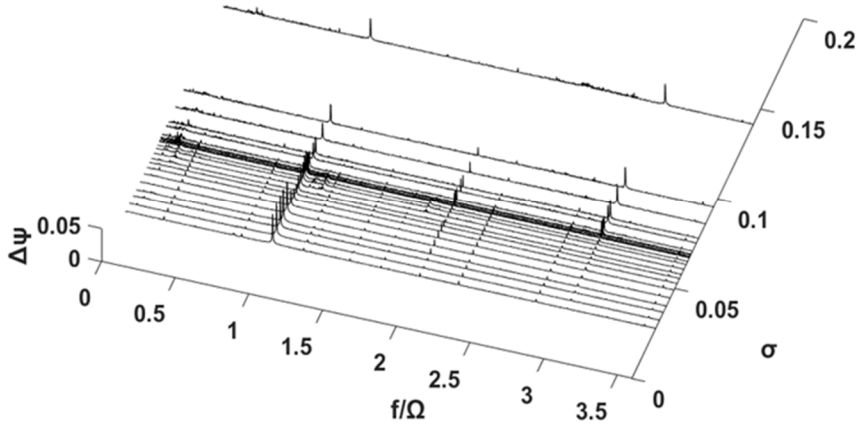

c) Re = 5.56 × 10^6

Figure C.10 The power spectral density plots of unsteady pressure

fluctuations at Σ^*=0.257 and ϕ/ϕ_d=1.0 for Re=3.95×10^6 (a), Re=4.65×10^6 (b), and Re=5.56×10^6 (c).

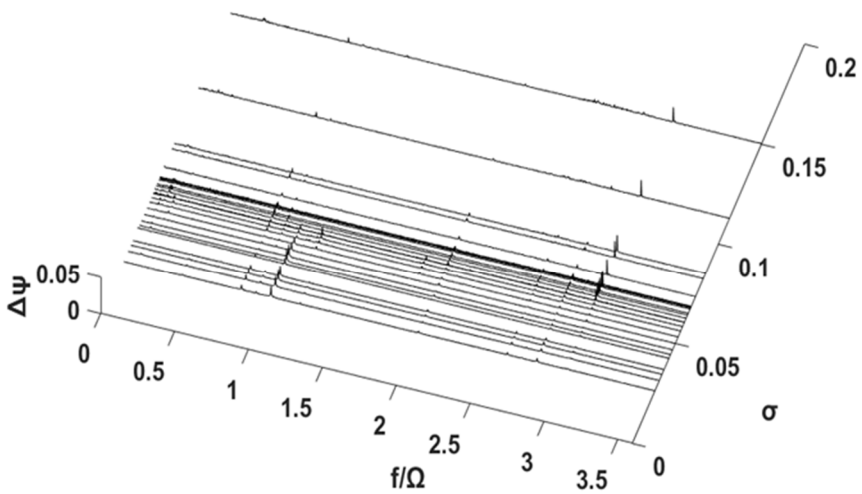

a) Re = 4.02 × 10^6

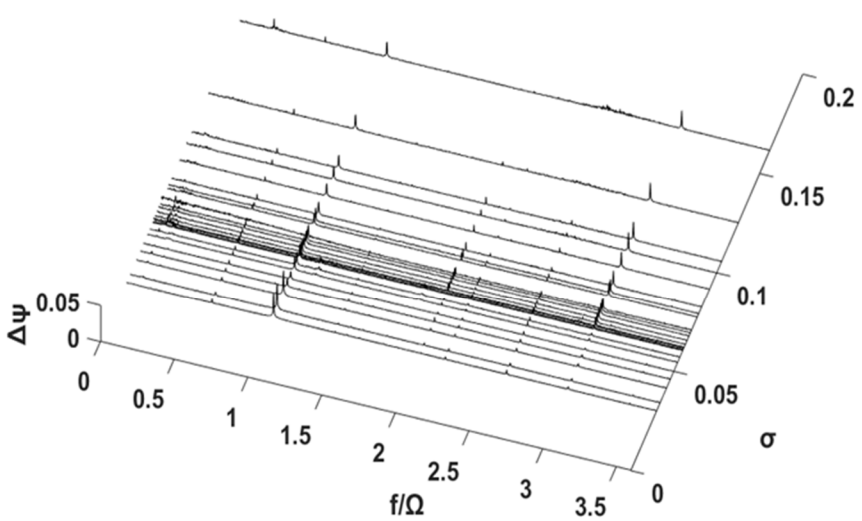

b) Re = 4.74 × 10^6

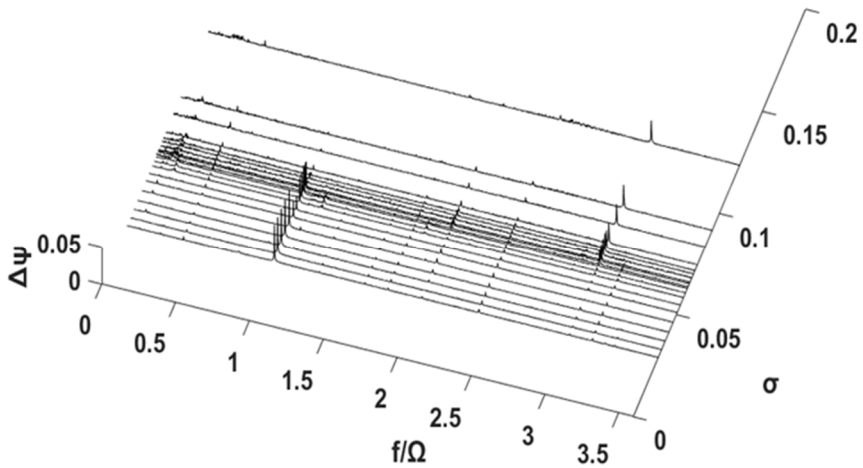

c) Re = 5.60 × 10^6

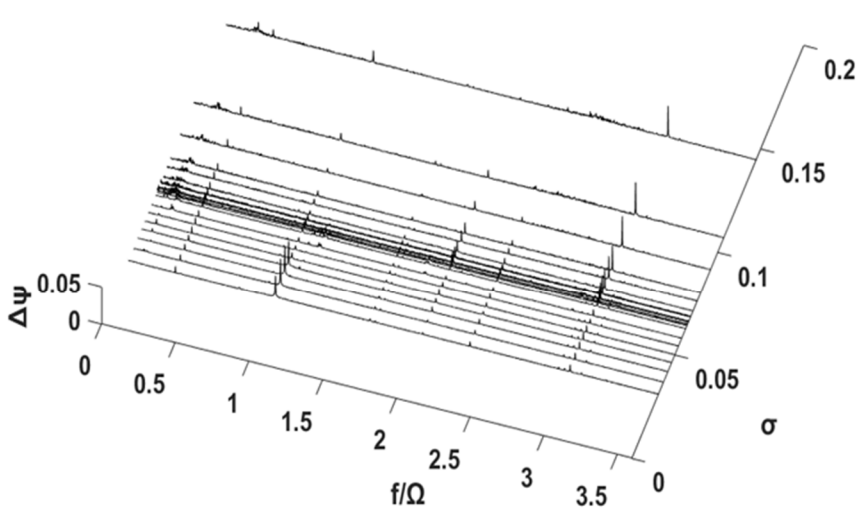

d) Re = 5.95 × 10^6

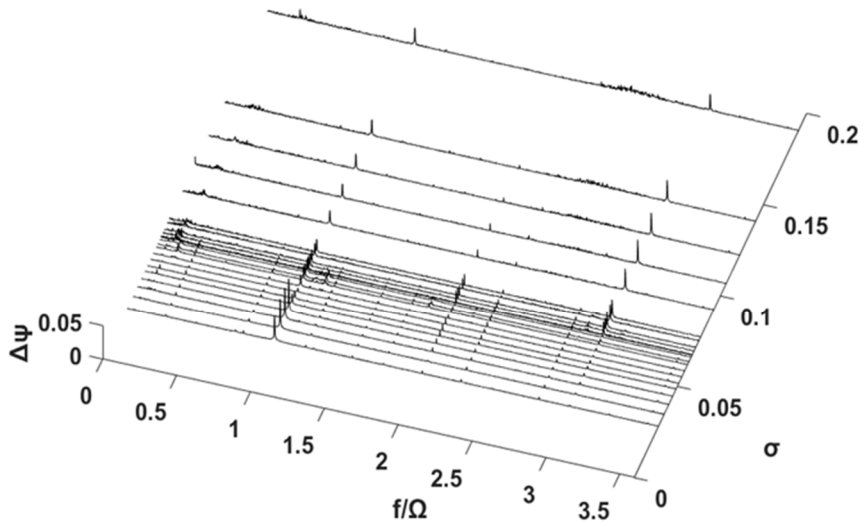

e) Re = 6.30 × 10^6

Figure C.11 The power spectral density plots of unsteady pressure fluctuations at Σ^*=0.516 and ϕ/ϕ_d=1.0 for Re=4.02×10^6 (a), Re=4.74×10^6 (b), Re=5.60×10^6 (c), Re=5.95×10^6 (d), and Re=6.30×10^6 (e).

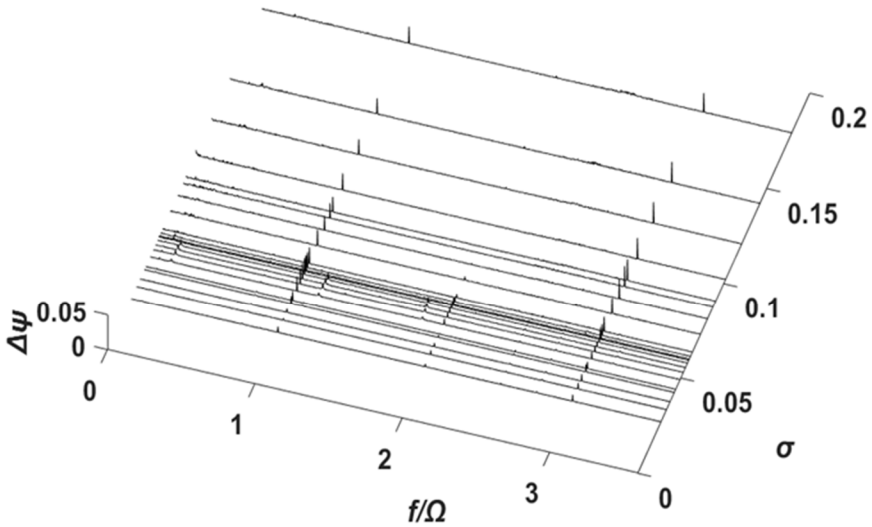

a) Re = 4.81 × 10^6

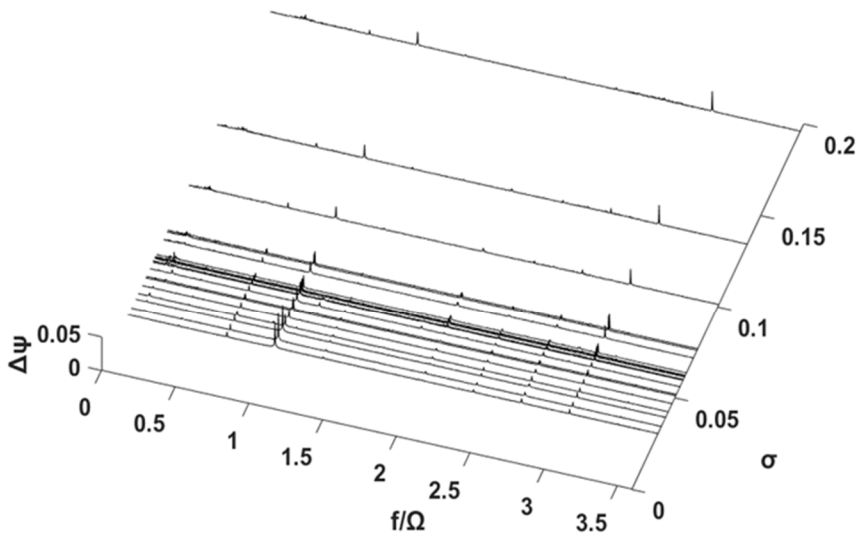

b) Re =5. 14 × 10⁶

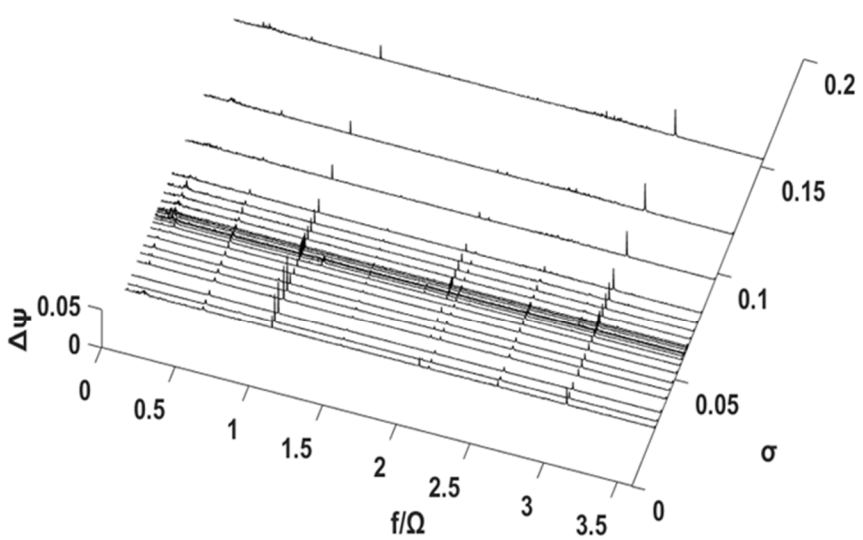

c) Re = 5.75 × 10⁶

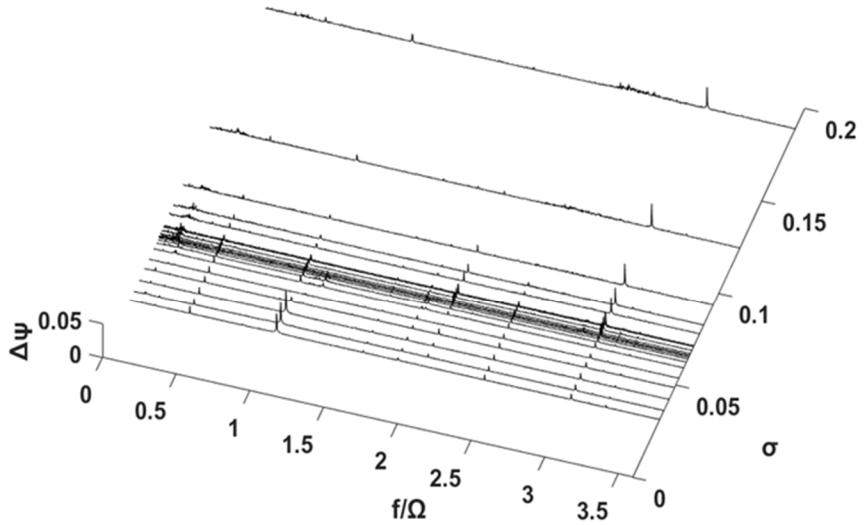

d) Re = 6.36 × 10^6

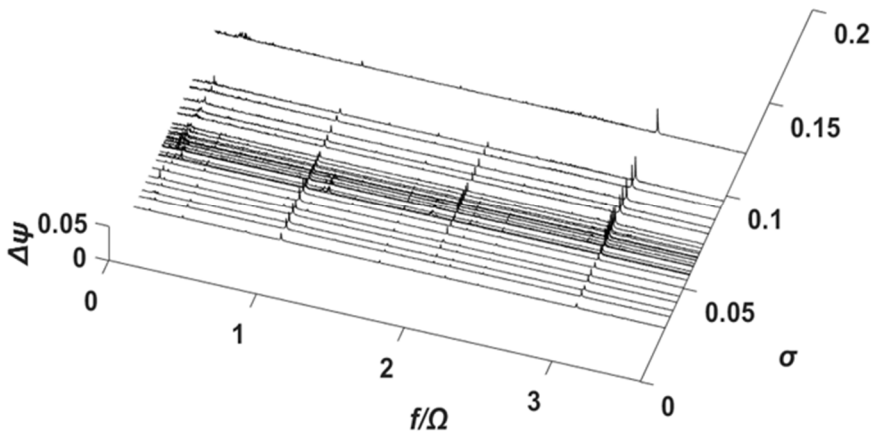

e) Re = 6.84 × 10^6

Figure C.12 The power spectral density plots of unsteady pressure fluctuations at Σ^*=1.26 and ϕ/ϕ_d=1.0 for Re=4.81×10^6 (a), Re=5.14 ×10^6 (b), Re=5.75×10^6 (c), Re=6.36×10^6 (d), and Re=6.84×10^6 (e).

Appendix D

PIV Raw Results

PIV results shown in Chapter 3 are ensemble averaged results. In Appendix D, 3 raw velocity vectors for each case (no rotating cavitation, large cavitation region under rotating cavitation, and small cavitation region under rotating cavitation) are shown, respectively.

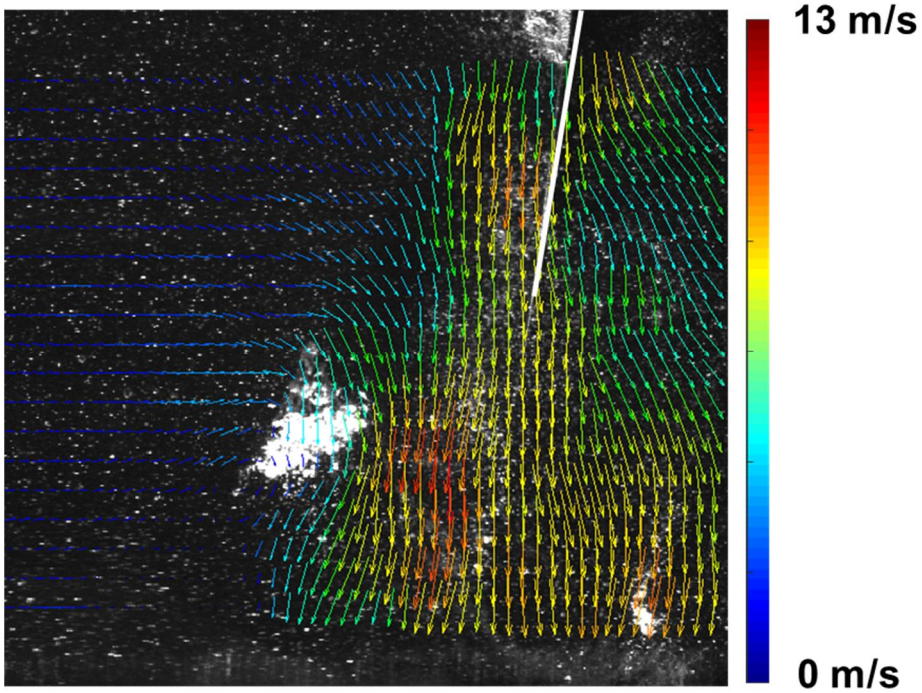

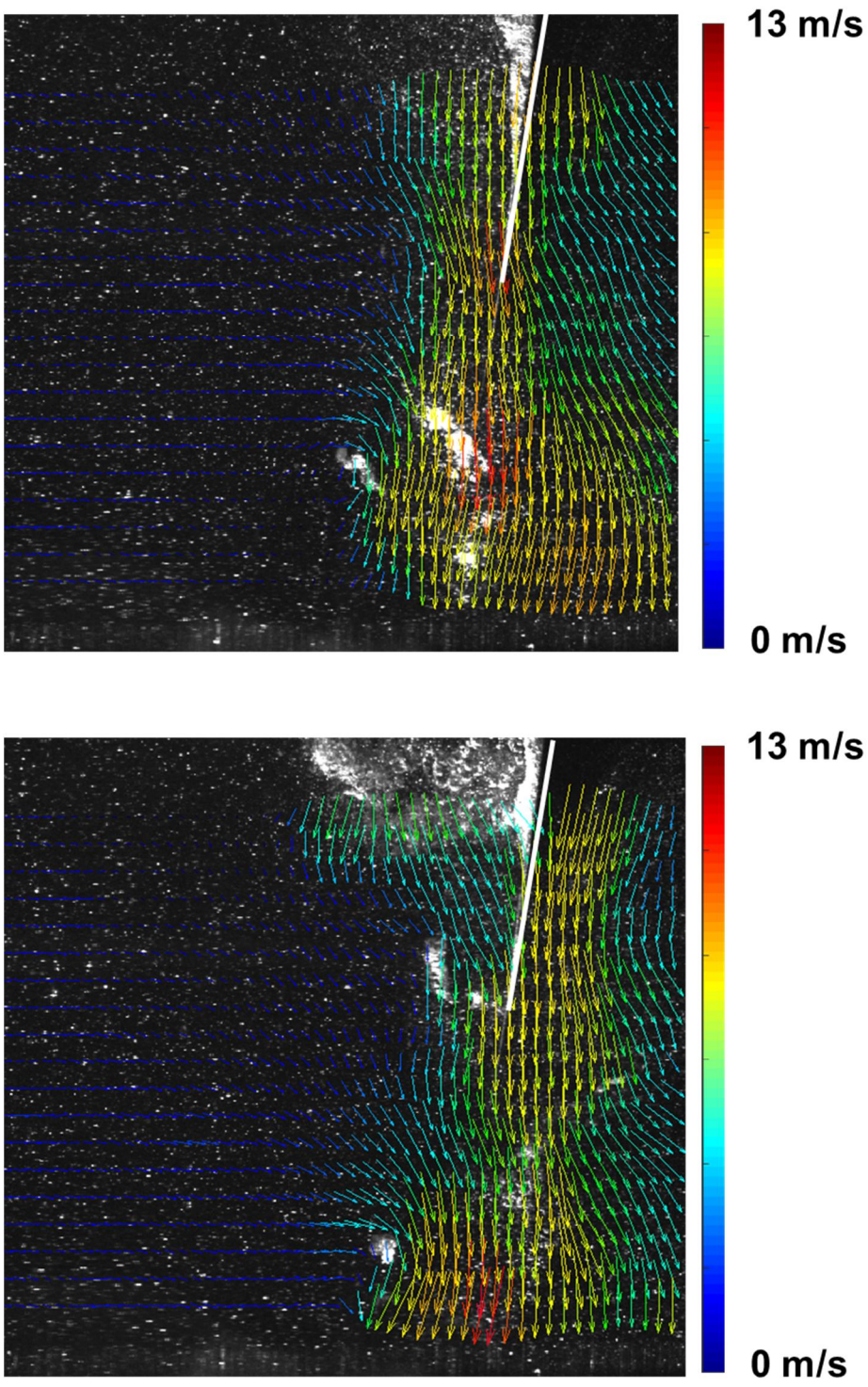

Figure D.1 Raw velocity vectors for no rotating cavitation.

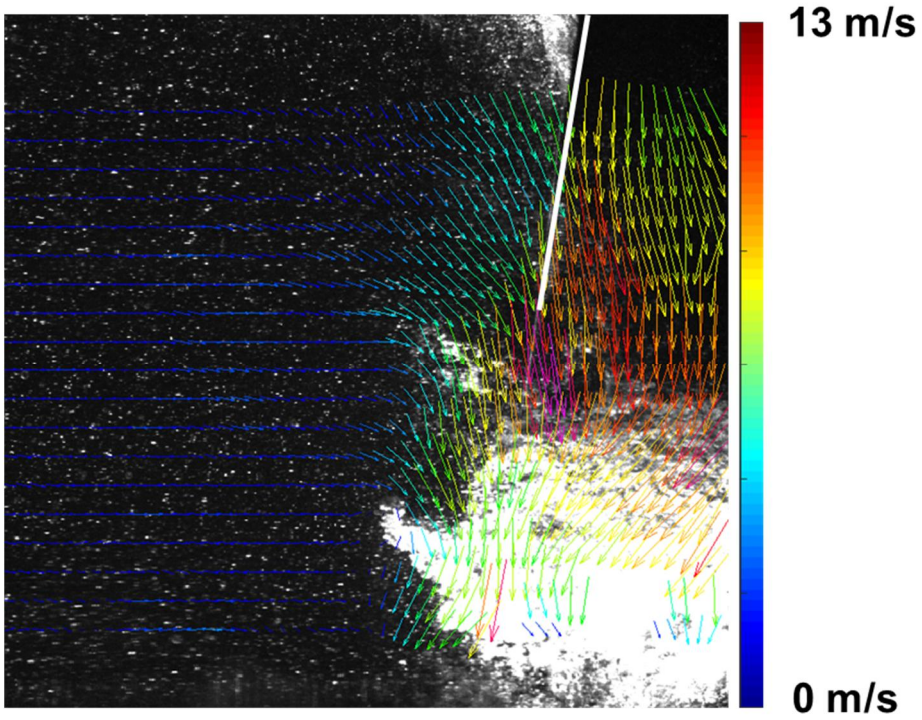
13 m/s
0 m/s

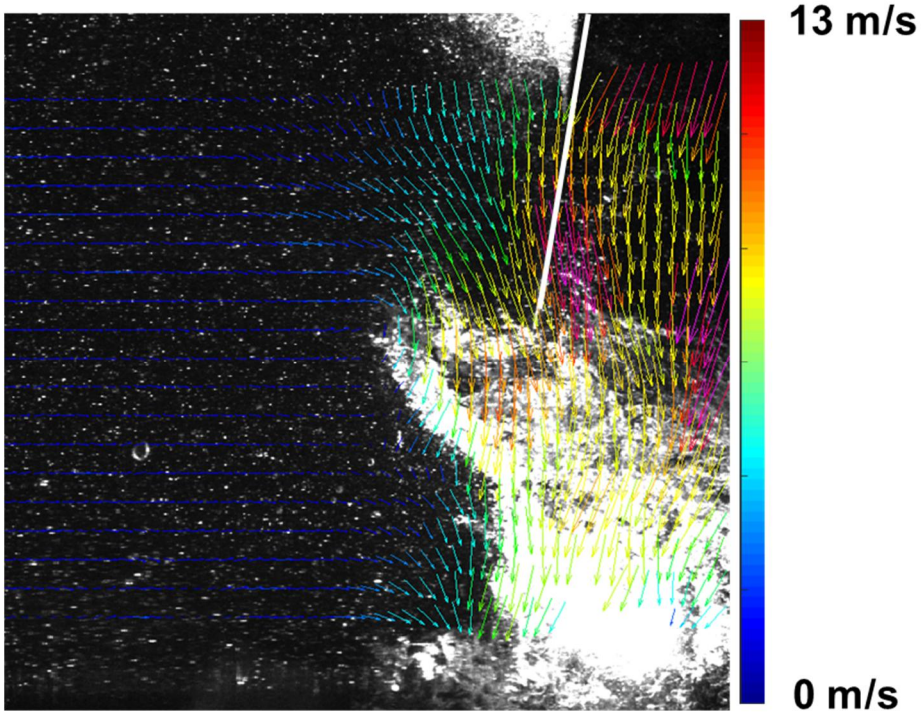
13 m/s
0 m/s

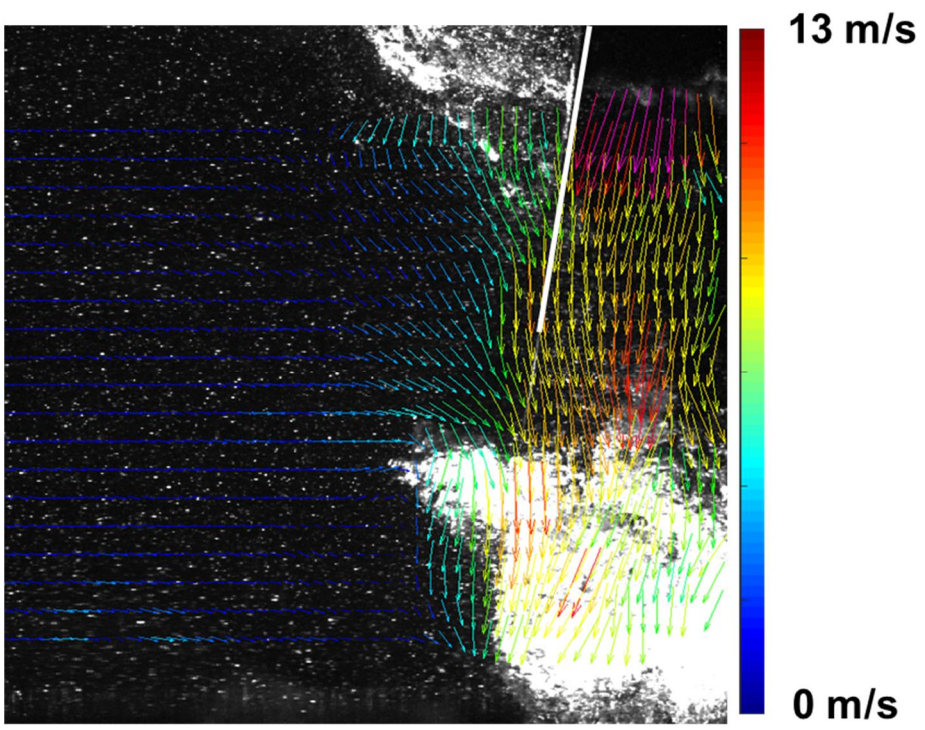

Figure D.2 Raw velocity vectors for large cavitation region under rotating cavitation.

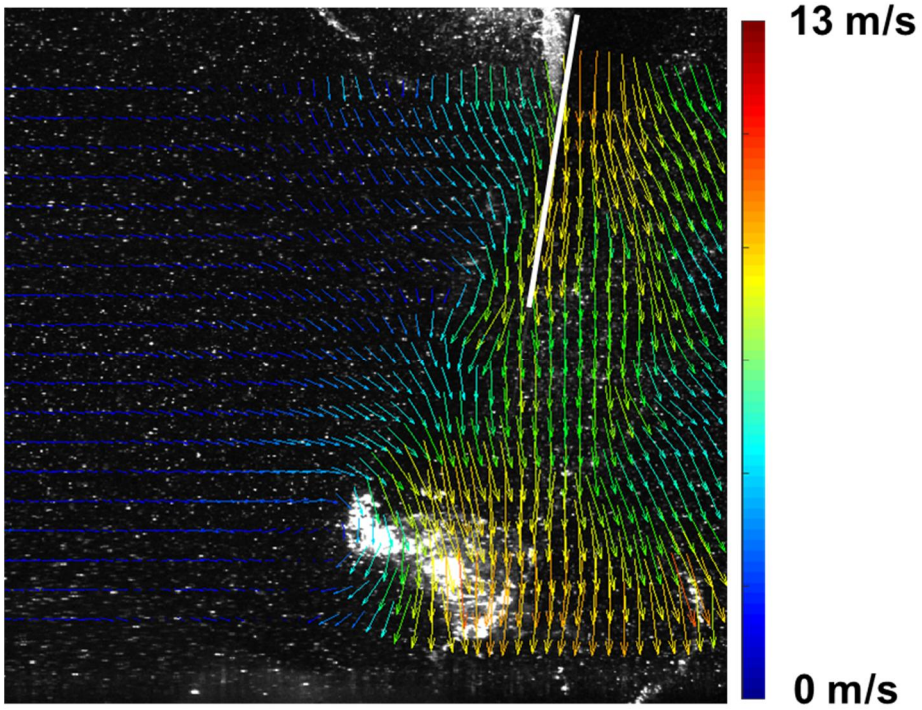
13 m/s
0 m/s

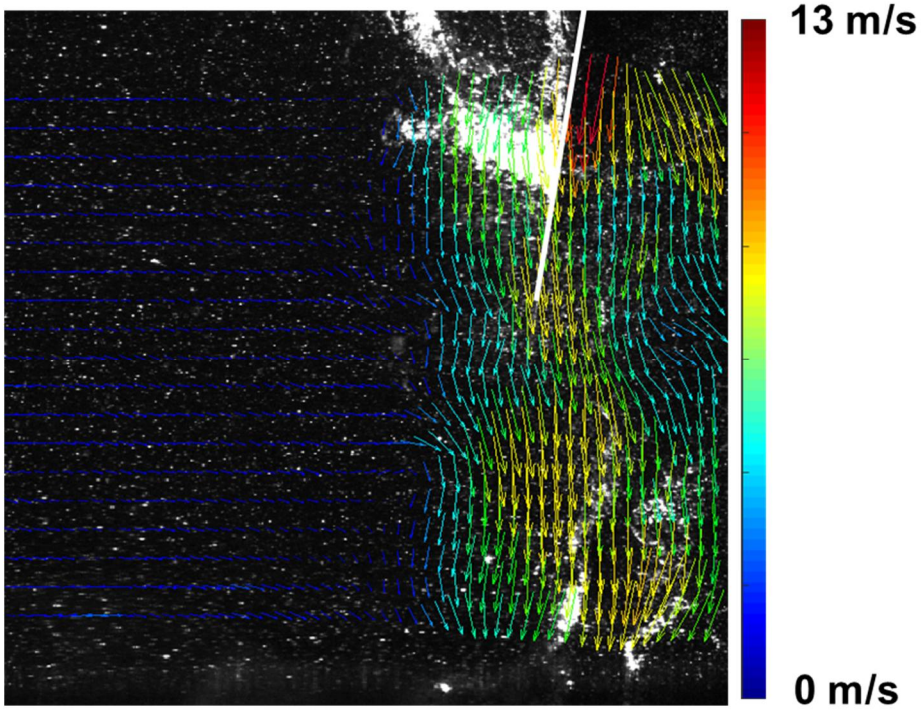
13 m/s
0 m/s

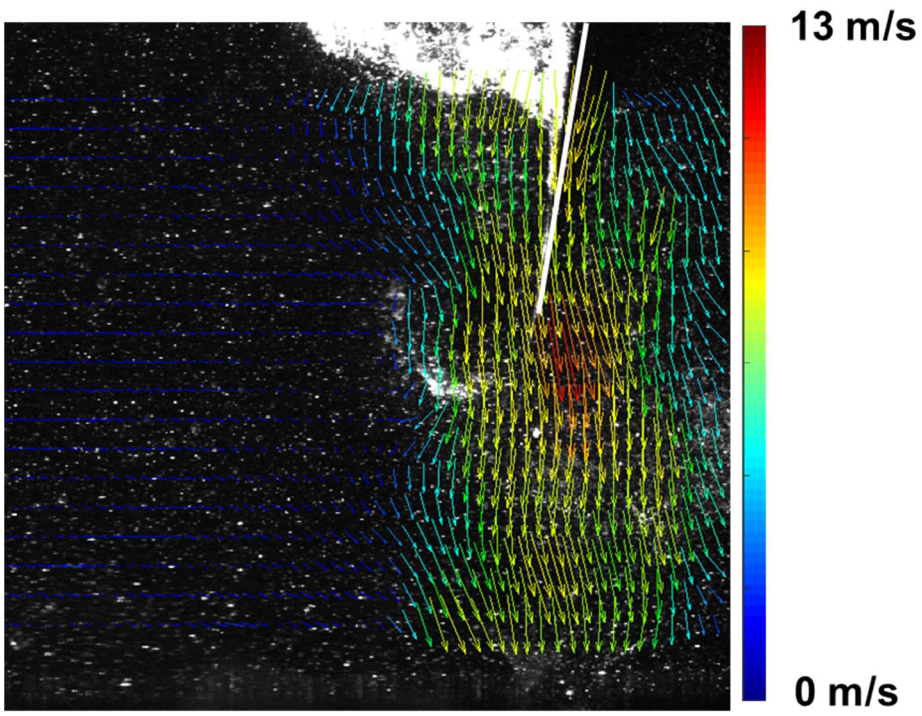

Figure D.3 Raw velocity vectors for small cavitation region under rotating cavitation.

Appendix E

Equipment Used in Experiments

Detailed equipment pictures used in cavitating experiments and PIV are shown in Appendix E. Detailed specifications of each equipment are summarized in Chapter 2.

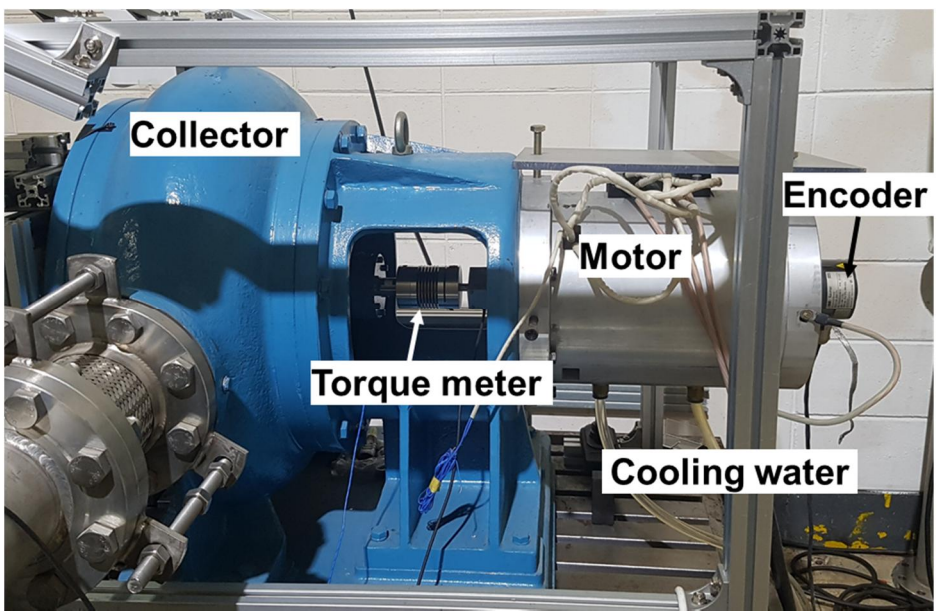

Figure E.1 Rotating parts.

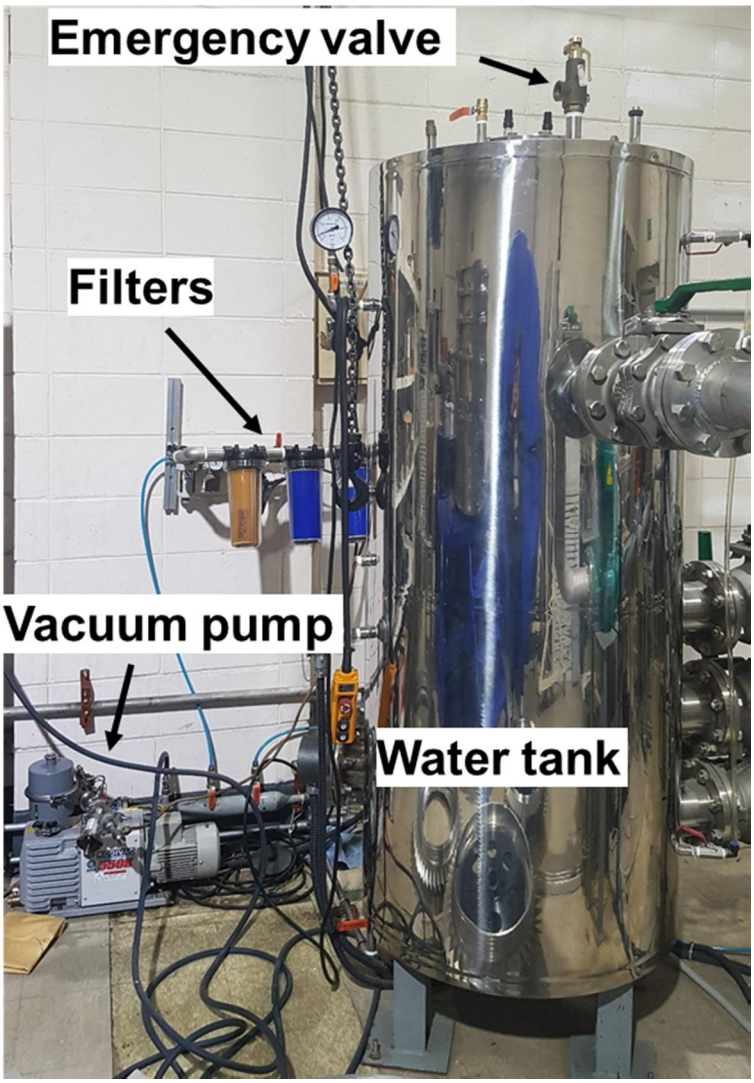

Figure E.2 Water tank and equipment attached to the water tank.

Figure E.3 Static pressure transducers (Druck).

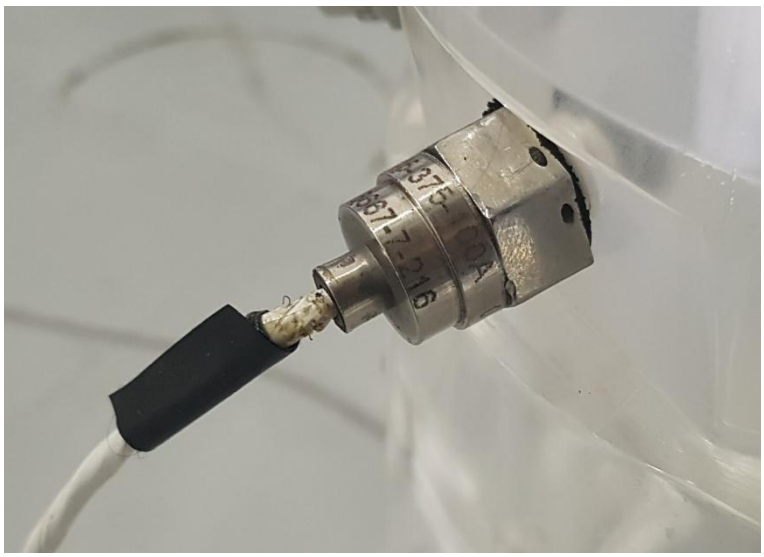

Figure E.5 Unsteady pressure transducers (Kulite).

Figure E.6 Amplifier (TEAC).

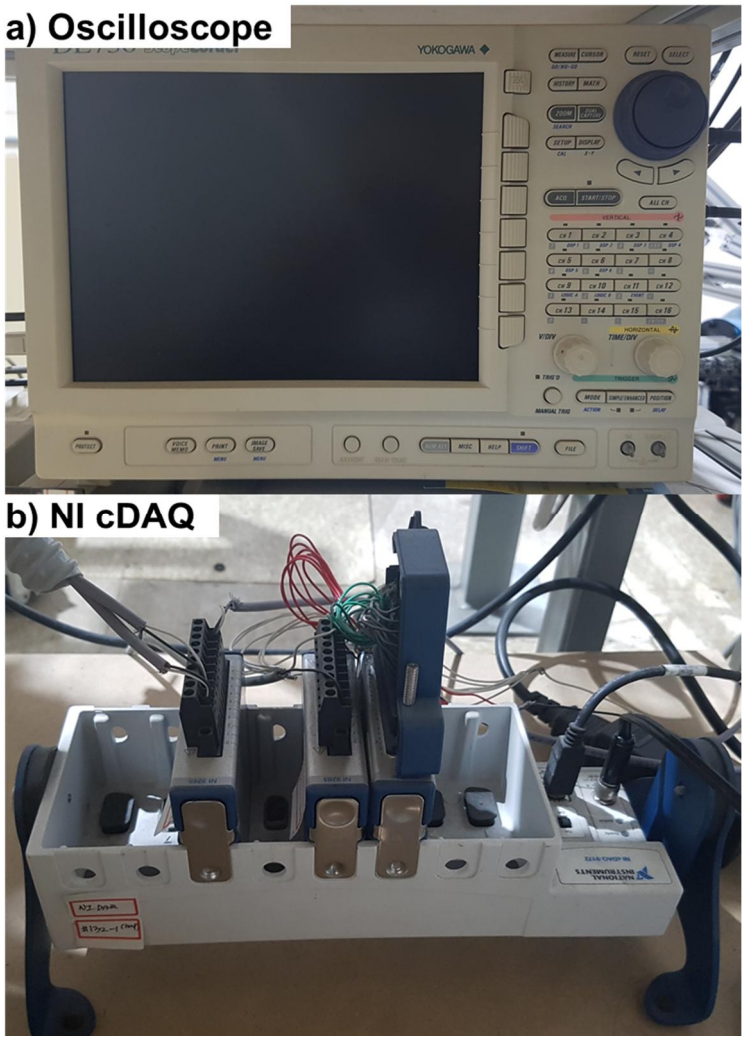

Figure E.7 Data acquisition system ((a) oscilloscope (Yokogawa), (b) NI cDAQ (National Instrument)).

a) Laser

b) Optics and alignment

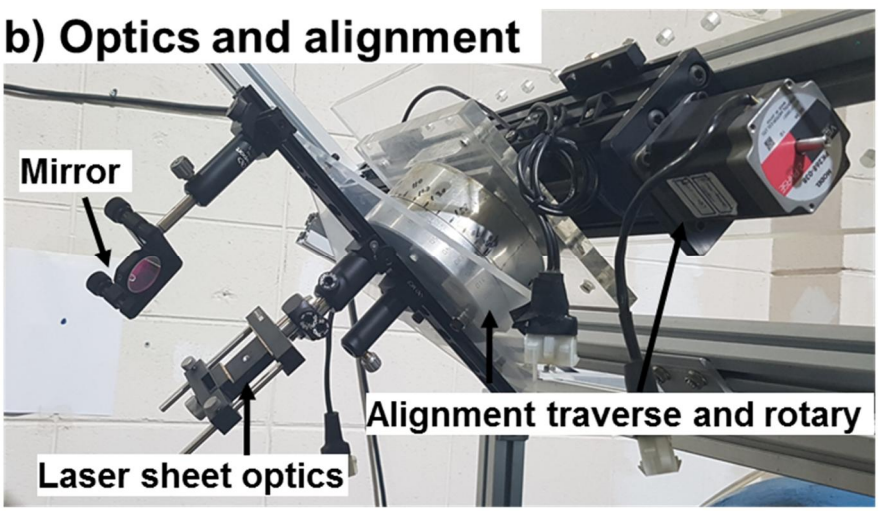

Figure E.8 PIV equipment ((a) Laser, (b) laser sheet optics and alignment traverse and rotary, (c) synchronizer (Quantum composer), and (d) CCD camera (PCO sensicam).

Appendix F

Inlet Flow Distortion Effects

In real turbopump system, oxidizer and fuel are supplied from the tanks to turbopumps through complex bent ducts. Figure F.1 shows the assembly of KSLV-2 liquid rocket engine [80] which is now being developed in Korea. The red circle indicates the turbopump, and upper one is oxidizer pump and the bottom is fuel pump. And inducers are installed upstream of each pump. In rocket engine, the complex piping system is required due to the restricted volume of rocket. Thus, the curved ducts are installed upstream of inducers and the inducer upstream flow must be distorted by the curved inlet. Therefore, inlet flow distortion effects on performance change and cavitation instability onset in turbopump inducers are important issues.

Few researches have been performed to investigate inlet flow distortion effects on critical cavitation number or the onset of rotating cavitation. Del Valle et al. [81] installed uniform and non-uniform honeycomb upstream of the inducer and measured the critical cavitation number (Fig. F.2 (a)). They reported that there is no difference in the critical cavitation number in case of uniform and non-uniform honeycomb case. Kang and Kang [82] installed radial obstacle to make flow come to the inducer in radial direction (Fig. F.2 (b)). They found that the critical cavitation number increases for the radial intake. Fujii et al. [83] installed non-uniform perforated screen upstream of the inducer (Fig. F.2 (c)). They

reported that the rotating cavitation onset cavitation number decreases in case of non-uniform perforated screen meaning more stable.

However, installation of honeycomb or screen upstream of the inducer results in cavitation bubbles at upstream of an inducer. And it cannot simulate secondary flow due to curved inlets. In previous research, inlet flow distortion effects on the critical cavitation number is unclear and the onset of rotating cavitation data is limited. Therefore, the objective of this study is to measure curved inlet effects using S-shaped duct on the critical cavitation number and the rotating cavitation onset cavitation number.

Experiments have been conducted at the same test facility. To simulate the inlet flow distortion, S-shaped inlet ducts of two different radius of curvature (1.0 and 1.5 diameter of the duct (D)) have been installed. To install the S-shaped inlets, the water tank has 3 different outlets as shown in Fig. F.3. Figure F.4 represents the detailed configurations of inlet shapes. The radius of curvature of each s-shaped inlet is determined at the centerline of the s duct. The red inlet represents when the radius of curvature is 1.0 diameter of the duct. It is the same radius of curvature with real KSLV-2 turbopump inlet duct. Blue line represents the 1.5 D radius of curvature case. The distance from the exit of the s-shaped inlet and the inducer leading edge (straight section length) is 2.0 D.

Using a 5-hole probe from Aeroprobe, the flow field upstream of the inducer has been measured at 0.9 D upstream from the inducer leading edge. Calibration of 5-hole probe has been performed prior to the measurements. Figure F.5 shows pictures of 5-hole probe calibration equipment. At the circular jet wind tunnel, 5-hole probe has been calibrated at -50° ~ 50°. Detailed

calibration process and coefficients are shown in [84]. Figure F.6 and F.7 show the calibration coefficient map and angle uncertainty results at Re=6,876 based on the probe diameter, respectively. Calibration tests have also been performed at Re=4,146 and 9,147 to check the Reynolds number dependency. The error is ± 3 % comparing, thus, the Reynolds number dependency is negligible. In the uncertainty map, blue are uncertainty is less than 0.5° . However, at 50° ~ 35° and −35° ~ −50° pitch angle, the uncertainty values are high. Thus, the 5−hole probe is possible to use in ranges from −35° to 35° following the calibration map and angle uncertainty.

The 2−D traverse system and rotary have been used to measure the flow velocity by 5−hole probe as shown in Fig. F.8. The measurement location is shown in Fig. F.9.

Firstly, the degree of the inlet flow distortion has been quantified using a circumferential inlet distortion factor which is from the SAE Aerospace Recommended Practice standard [].To calculate the circumferential distortion factor, a distortion intensity at each ring should be calculated. The definition of the intensity is as follow.

$$\text{Intensity}_i = \frac{V_{avg,i} - V_{low,i}}{V_{avg,i}} \quad \text{(F.1)}$$

$V_{avg,i}$ = average axial velocity of each ring

$V_{low,i}$ = average of axial velocities lower than $V_{avg,i}$

$V_{avg,i}$ represents the average axial velocity of each ring, and $V_{low,i}$ represents the average of axial velocities lower than the

average velocity of the ring. The intensity represents the degree of the circumferential distortion at each ring. The circumferential distortion factor (CDI_{avg}) is average of each ring's intensity.

$$CDI_{avg} = \sum_{i=1}^{n} \frac{Intensity_i}{n} \quad \text{(F.2)}$$

The inlet flow is measured at non-cavitating condition 1.8 bar. Figure F.10 represents axial velocity distribution normalized by the inducer tip speed and velocity vectors for the radius of curvature 1.0 D and 1.5 D (straight section length 2.0 D). The axial velocity is lower at bottom region, and increases to the upper region. From the velocity vectors, vortex structure is formed due to the S-shaped inlets. The vortex structure is asymmetric due to the upstream propagation of the inducer pre-rotation as found in Hosangdi et al. [39]. The circumferential distortion factor for the radius of curvature 1.0 D is 0.177 which is higher than the 1.5 D radius of curvature.

Cavitation performance for the s-shaped inlets and straight inlet have been compared at the design flow coefficient as shown in Fig. F.11. Blue line and red line is for the 1.0 D and 1.5 D radius of curvature case, respectively. At the design flow coefficient, the critical cavitation number of the s-shaped inlet (σ_{crit}=0.082) is 16 % higher than the straight inlet. Figure F.12 shows the critical cavitation number versus flow coefficients. The critical cavitation numbers of the S-shaped inlet are higher for all measured flow coefficient than the straight inlet. However, the radius of curvature effects does not significantly affect the critical cavitation number.

Cavitation instabilities have been also identified for the s-shaped inlet. Figure F.13 shows the power spectral density of

unsteady pressure fluctuations at the design flow coefficients of the S-shaped inlet for the radius of curvature 1.0 D and straight length 2.0 D case. Rotating cavitation and asymmetric attached cavitation occurs like the straight inlet with the same frequency. Types and frequencies of cavitation instabilities do not change by the S-shaped inlet. However, the onset cavitation number of rotating cavitation is different as shown in Fig. F.14. Figure F.14 represents the rotating cavitation onset cavitation number according to the flow coefficients. For flow coefficient lower than the design flow coefficient, rotating cavitation does not occur in straight and S-shaped inlets. At the design flow coefficient, the rotating cavitation onset cavitation number does not depend on the radius of curvature. Also, the critical cavitation number corresponds to the rotating cavitation onset cavitation number in case of S-shaped inlets, which shows the same correspondence as shown in Chapter 3 and 4. For flow coefficient larger than the design flow coefficient, the rotating cavitation onset cavitation number of the S-shaped inlet is higher than the straight inlet.

The effects of straight section length also have been measured. Velocity has been obtained at different straight section lengths from 1.0 D to 4.0 D as shown in Fig. F.15. For 1.0 D straight section length cases, the axial velocity at bottom region is much higher than the upper parts. As the straight section length becomes longer, the upper region velocity becomes higher. The circumferential distortion factors have also been calculated. The flow is more distorted in 1.0 D radius of curvature than 1.5 D radius of curvature. The distortion factor also increase as the straight section length decreases.

Figure F.16 represents the onset cavitation numbers of rotating

cavitation and asymmetric attached cavitation for different CDI_{avg} values at the design flow coefficient. Rotating cavitation occurs at higher cavitation number when the S-shaped inlets are installed. However, the rotating cavitation onset cavitation number remains constant as CDI_{avg} increases. The rotating cavitation onset cavitation numbers according to CDI_{avg} at different flow coefficients are shown in Fig. F.17. As CDI_{avg} increases, the rotating cavitation onset cavitation number increases. Rotating cavitation easily occurs as incidence angle decreases as reported in Tani et al. [41]. Thus, it is suspected that the distorted flow may decrease the local incidence angle and promote rotating cavitation onset. On the other hand, the onset cavitation number of asymmetric attached cavitation does not depend on the inlet flow distortion as shown in Fig. F.16.

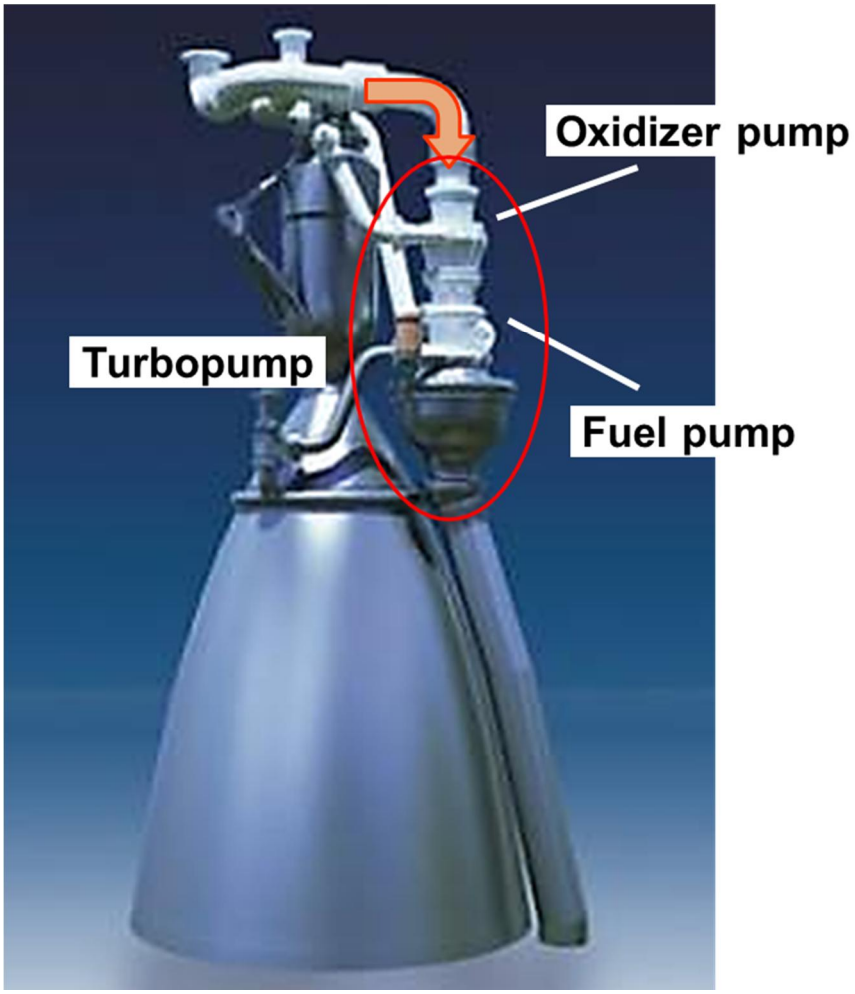

Figure F.1 Assembly of KSLV-2 liquid rocket engine [80].

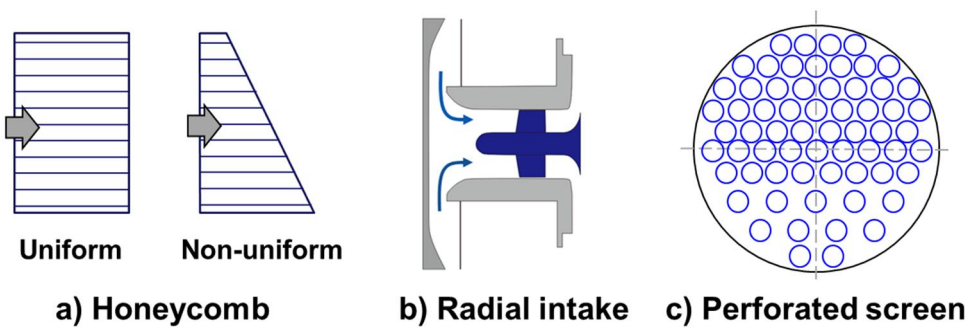

Figure F.2 Inlet flow distortion method from previous research (non-uniform honeycomb (a), radial intake (b), non-uniform

perforated screen (c)).

Figure F.3 Piping for S-shaped inlets

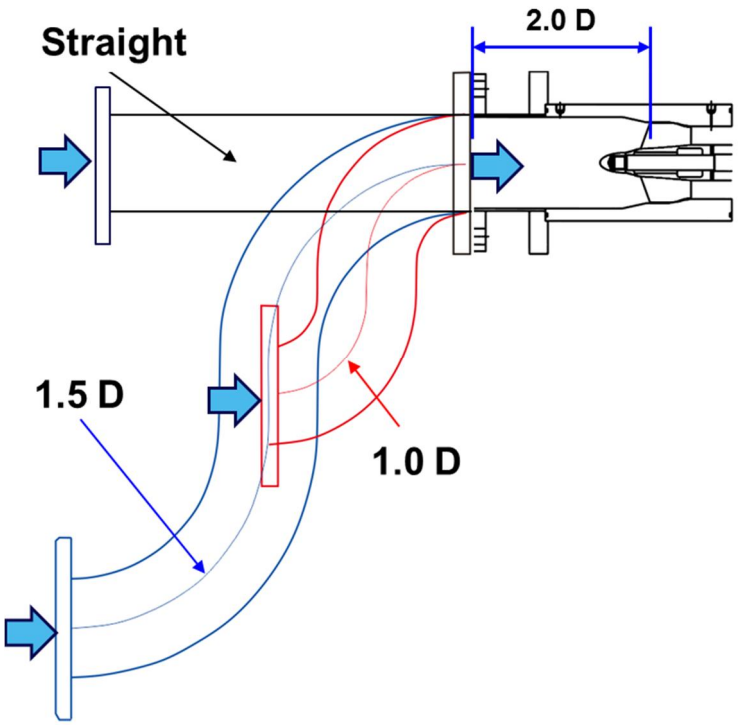

Figure F.4 Configuration of inlet shapes.

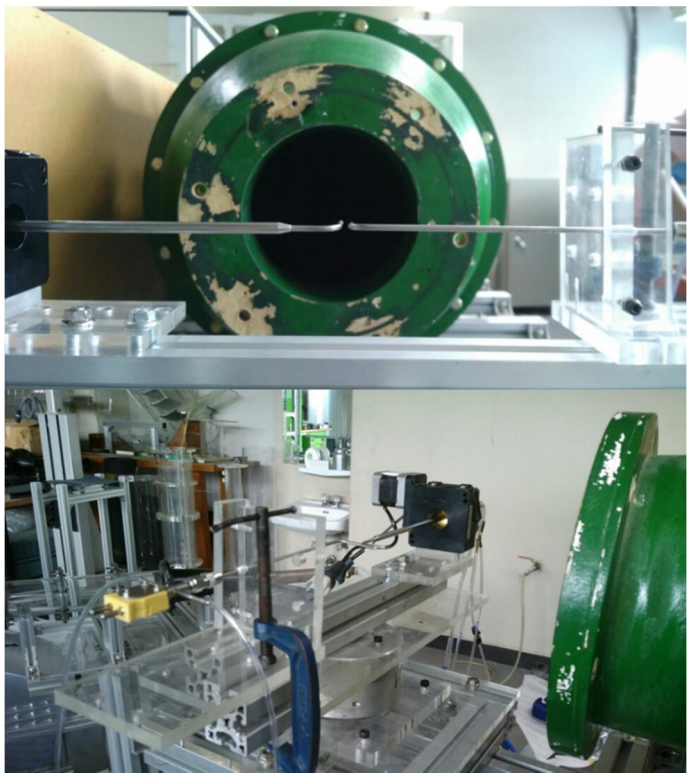

Figure F.5 5-hole probe calibration equipments.

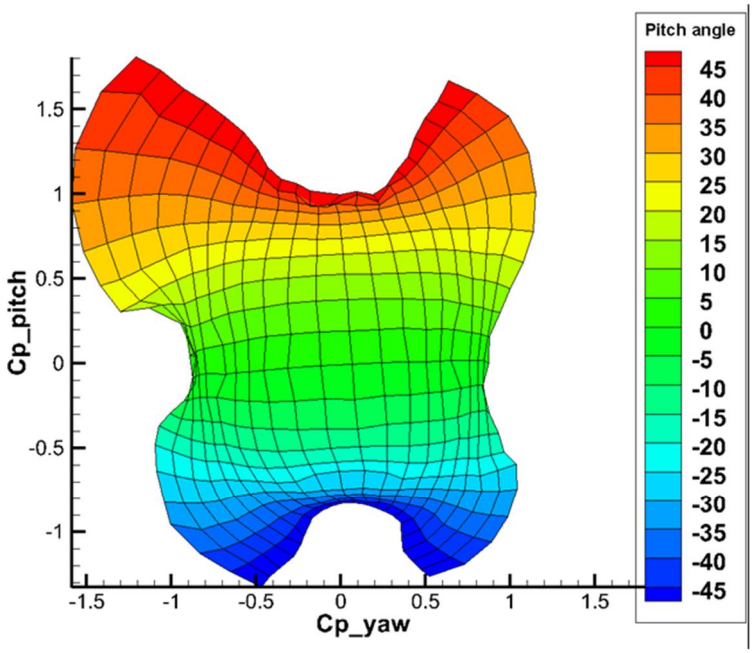

a) Pitch angle map

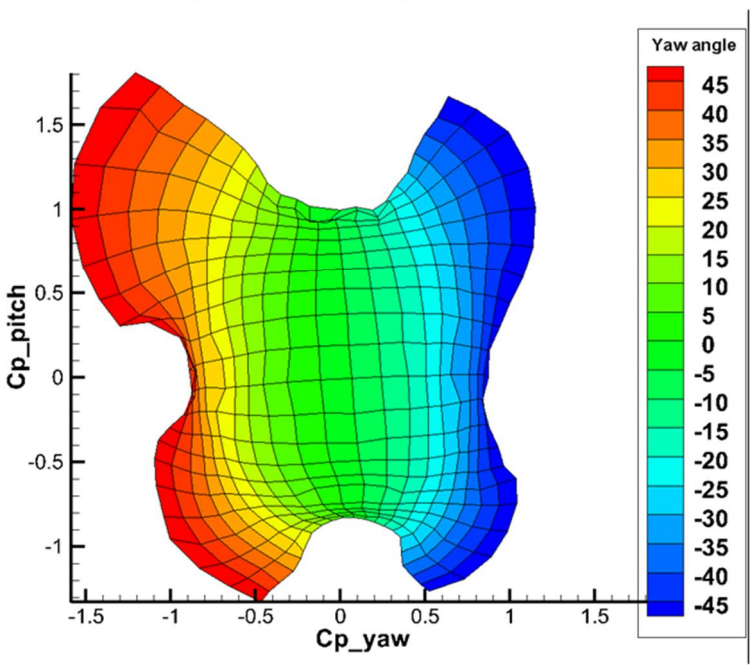

b) Yaw angle map

Figure F.6 Calibration coefficient map (Pitch (a) and Yaw (b) angle).

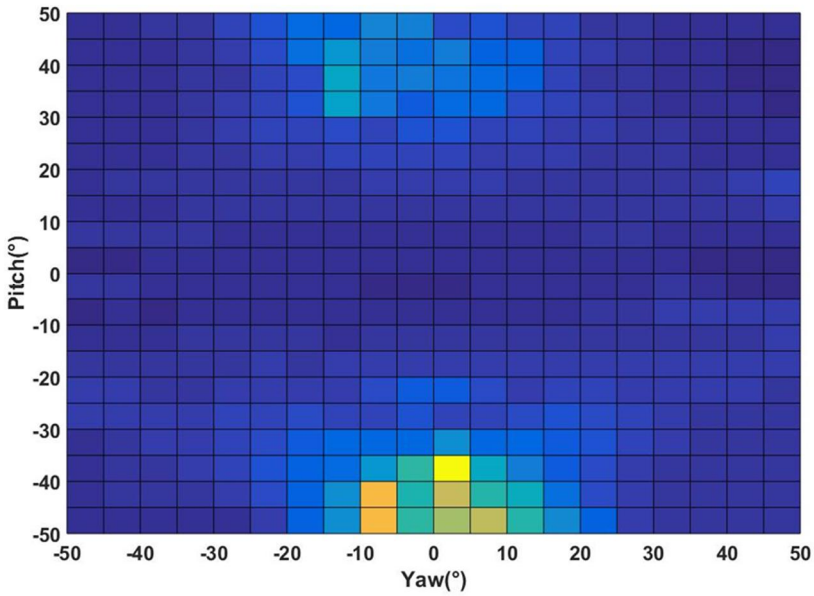

Figure F.7 Calibration uncertainty map
(blue region is less than 0.5 %, sky blue region is about 1 % and other region is higher than 1 %).

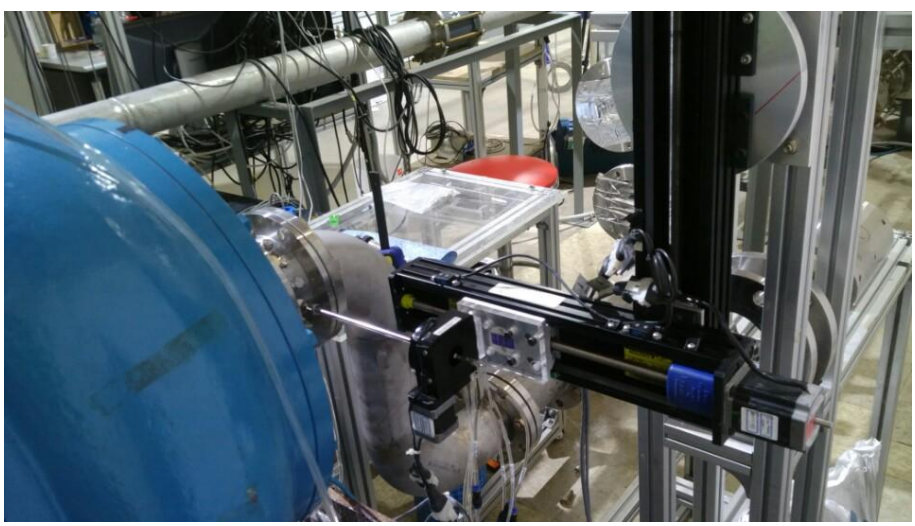

Figure F.8 The measurement method of velocity using 5-hole probe.

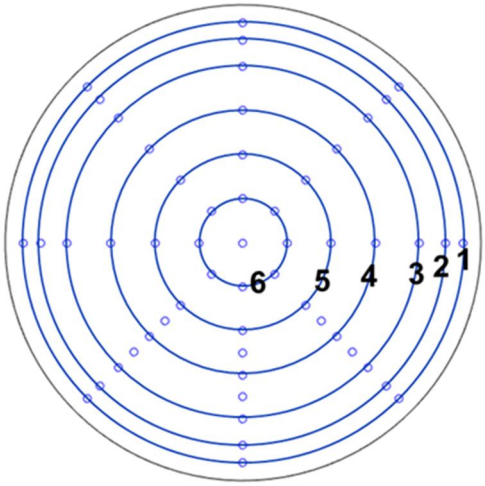

Figure F.9 5-hole probe measurement location.

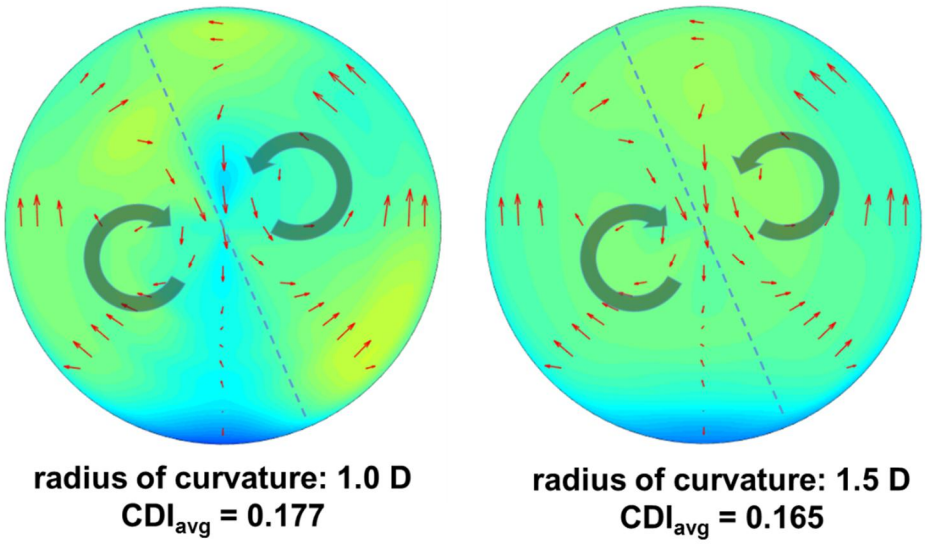

Figure F.10 Axial velocity distribution and velocity vectors for the radius of curvature 1.0 D (left) and 1.5 D (right) (straight section length is 2.0 D).

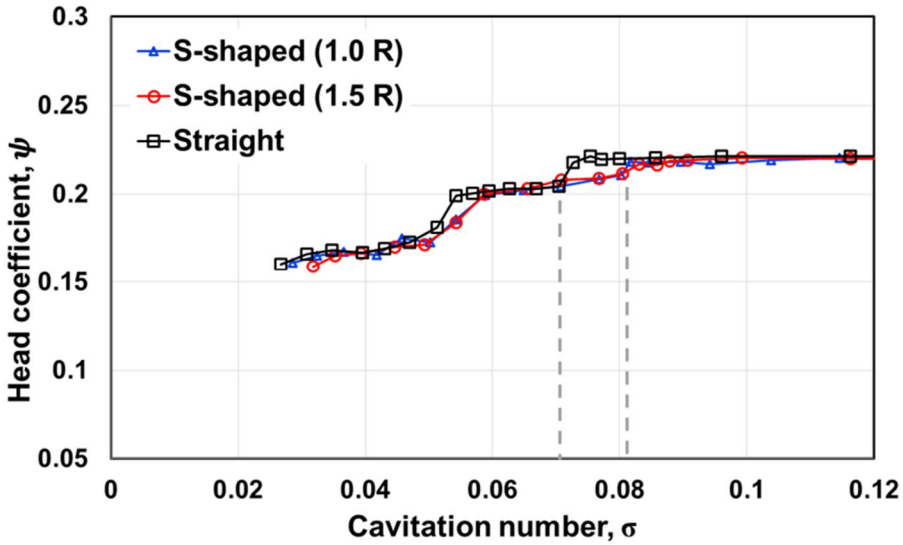

Figure F.11 Cavitation performance of s-shaped inlets at ϕ/ϕ_d=1.0.

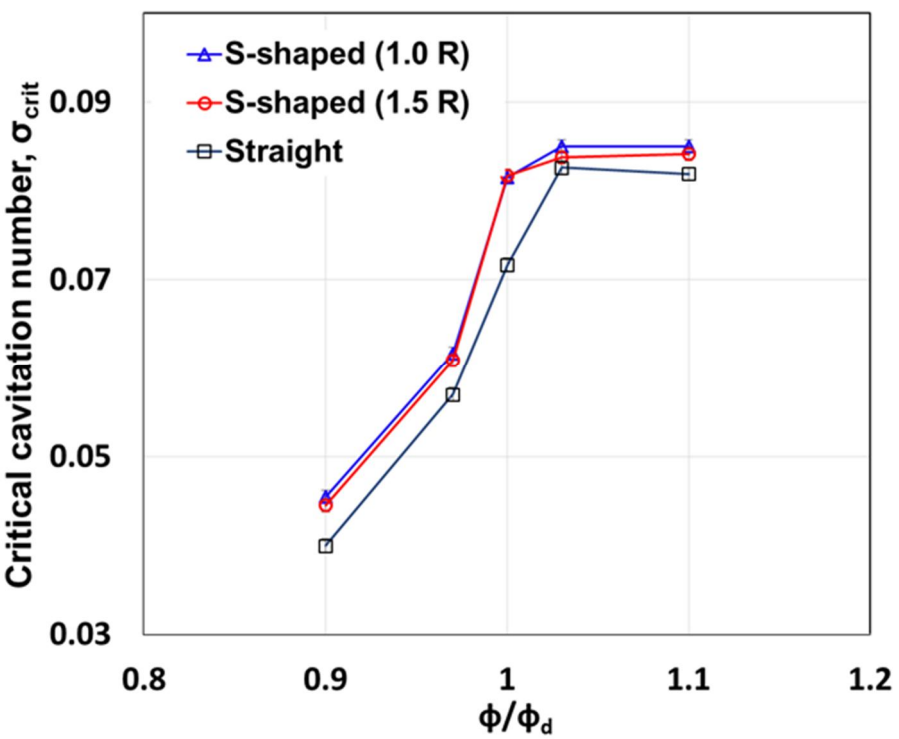

Figure F.12 The critical cavitation number versus the flow coefficients.

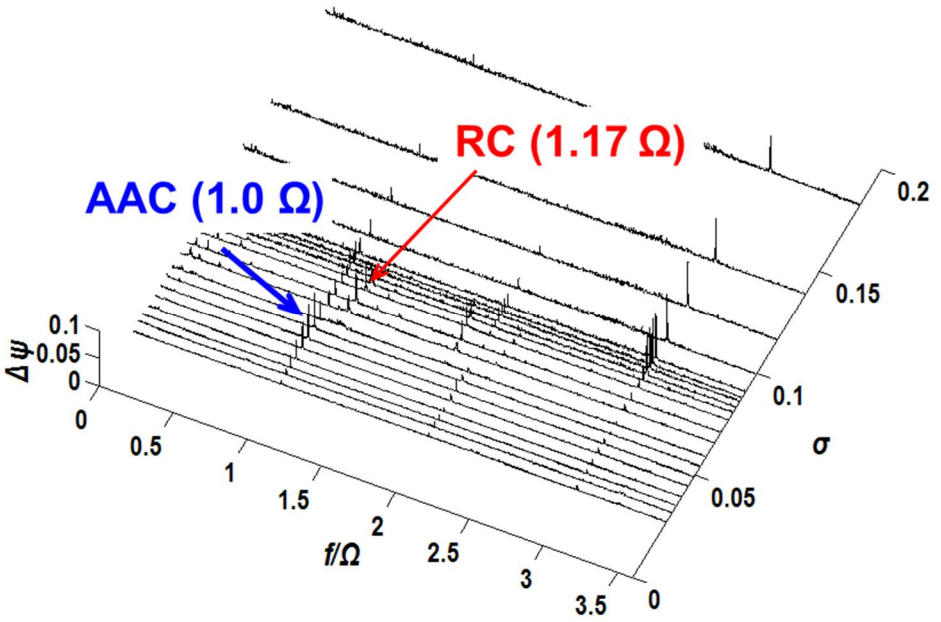

Figure F.13 The power spectral density plots of unsteady pressure fluctuations at ϕ/ϕ_d=1.0 of the s-shaped inlet (1.0 R/2.0D).

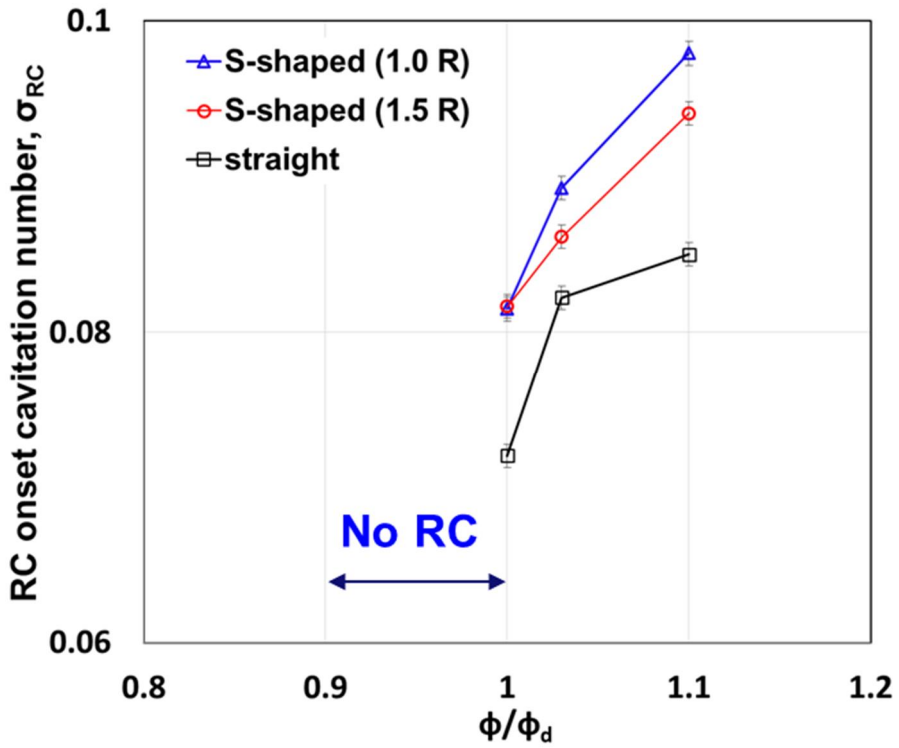

Figure F.14 The onset cavitation number of rotating cavitation for different flow coefficients.

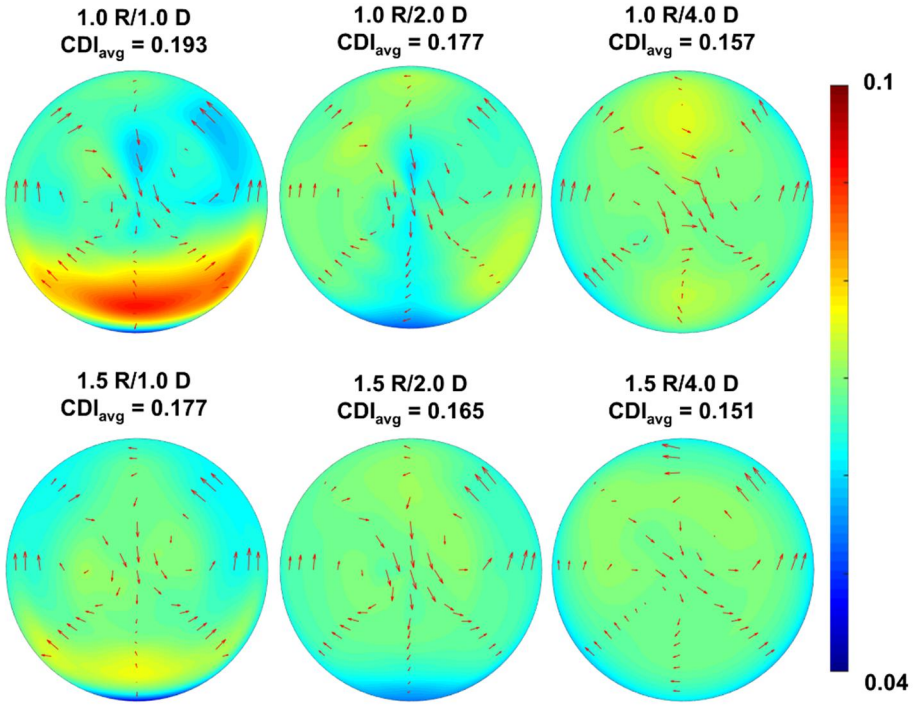

Figure F.15 Axial velocity distribution and velocity vectors for various radius of curvatures and straight section lengths (radius of curvature/straight section length).

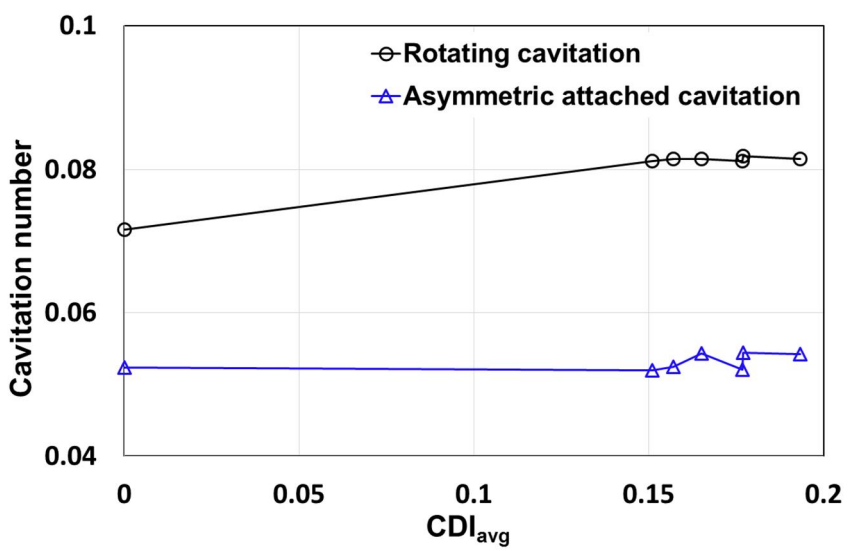

Figure F.16 The onset cavitation numbers of rotating cavitation and asymmetric attached cavitation for different CDI$_{avg}$ values at ϕ/ϕ_d=1.0.

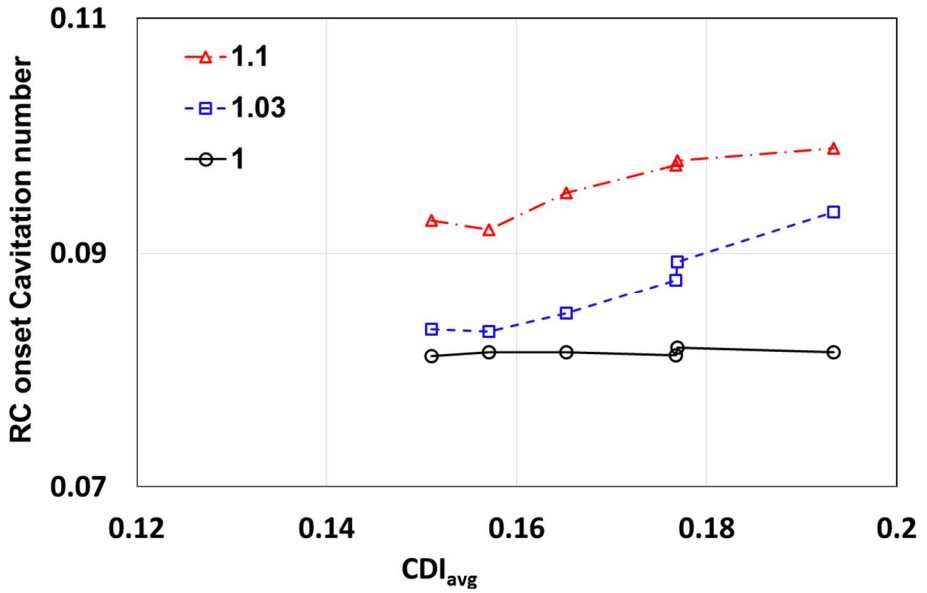

Figure F.17 The onset cavitation number of rotating cavitation for different CDI_{avg} values at various flow coefficients.

요약(국문초록)

터보펌프 인듀서에서의 캐비테이션 불안정성 메커니즘 및 열적 효과 연구

김 준 호

기계항공공학부

서울대학교 대학원

터보펌프에서 발생하는 선회 캐비테이션의 원인과 전파 메커니즘, 그리고 선회 캐비테이션 발생에 열적 효과가 미치는 영향에 대한 실험적인 연구를 수행하였다. 이러한 목적을 달성하기 위해 서울대학교에 실험 장비를 설계하고 구축하였다.

선행 연구를 바탕으로 인듀서 입사각의 변화가 선회 캐비테이션을 유도한다는 가정을 세웠다. 이를 입증하기 위해 입자 영상 유속계 방법을 통해 인듀서 팁 부근에서의 입사각을 측정하였다. 선회 캐비테이션 상황에서는 큰 팁 누설 캐비테이션 영역과 작은 팁 누설 캐비테이션 영역이 각각 형성된다. 큰 팁 누설 캐비테이션은 다음 날개의 입사각을 음의 값까지 감소시키면서 캐비테이션 영역을 억제한다. 반면, 작은 팁 누설 캐비테이션은 다음 날개의 입사각을 다시 양의 값으로 회복시키며, 다음 날개의 캐비테이션 영역이 성장한다. 캐비테이션 영역이 성장하면서 다음 날개의 입사각을 음의 값으로

줄이면서 선회 캐비테이션은 발생한다. 또한, 캐비테이션 영역의 성장과 억제가 순차적으로 발생하며 각 날개의 캐비테이션 영역이 측정한 주파수와 같이 섭동한다.

인듀서 입구에서 측정한 비정상 압력 측정을 바탕으로 레이놀즈 수와 무차원 열적 변수에 따른 선회 캐비테이션의 발생 캐비테이션 수 변화를 측정하였다. 무차원 열적 변수가 증가는 선회 캐비테이션을 억제하며 선회 캐비테이션 발생 캐비테이션 수가 지속적으로 감소한다. 낮은 무차원 열적 변수(e.g., 0.0125)에서는 선회 캐비테이션 발생 캐비테이션 수는 레이놀즈 수 변화와 무관하다. 하지만 그보다 높은 무차원 열적 변수(e.g. higher than 0.0537)에서는 선회 캐비테이션 발생 캐비테이션 수는 레이놀즈 수가 증가하면서 증가한다. 따라서, 레이놀즈 수는 선회 캐비테이션 발생을 촉진한다.

이 연구는 선회 캐비테이션의 원인과 메커니즘에 대한 첫 번째 실험적 결과를 제공한다. 또한 선회 캐비테이션 발생에 대해 무차원 열적 변수와 레이놀즈 수의 각각의 효과를 첫 번째로 평가하였다.

핵심어 : 터보펌프 인듀서, 캐비테이션 불안정성, 캐비테이션 성능, 열적 효과, 선회 캐비테이션, 입자 영상 유속계

학번 : 2011-23329